

NVH Analysis Techniques for Design and Optimization of Hybrid and Electric Vehicles

Chapter 3

Experimental Approaches for the NVH study of Electric and Hybrid Electric vehicles

Ramon Peral-Orts¹, Stephanos Theodossiades², Stephen Walsh³

¹Mechanical Engineering and Energy Department, Miguel Hernández University of Elche, Av de la Universidad, S/N - 03202, Elche, Spain, ramon.peral@umh.es,

²School of Mechanical and Manufacturing Engineering, Loughborough University, Loughborough LE11 3TU, UK, S.Theodossiades@lboro.ac.uk,

³Department of Aeronautical & Automotive Engineering, Loughborough University, Loughborough LE11 3TU, UK, S.J.Walsh@lboro.ac.uk,

Abstract. The use of experimental techniques to analyse NVH on vehicles with Internal Combustion Engines (ICE) has led to a significant improvement on the mechanical characteristics of those vehicles, as well as to successful results regarding their internal comfort. With the increasing commercialization of Electric and Hybrid Electric Vehicles, the vibro-mechanical conditions of the vehicles have changed dramatically, giving as a result new NVH challenges affected by a variety of sources. As a consequence, key experimental approaches to determine the effectiveness of Electric Vehicles, as well as new materials, NVH configurations and the environmental consequences of the EVs use are presented in this chapter.

The aim of is to compile main contributions regarding the adaptation and application of experimental methodologies to study the NVH of hybrid electric vehicles and electric vehicles.

1 Introduction

The automotive companies are facing increasing pressure, both from legislation and customers, to provide “noiseless” vehicles, with two main objectives: (i) reduce noise emissions and (ii) increase driving comfort. As a result, the development of vehicles utilising electric drive systems in combination with, or instead of, traditional combustion engines, are becoming increasingly attractive [1], but their “better vibro-acoustics conditions” should be tested and studied in depth.

Traditionally, the empirical study of NVH in vehicles has developed a significant improvement on the driver/passenger comfort, driving security or reduction on traffic noise pollution. The increase in sales of Hybrid Electric Vehicles, HEVs, and Electric Vehicles, EVs, is bringing out new challenges to companies and research groups that only can be afforded by adapting or developing experimental procedures for the study of the interior-exterior behaviour of their systems. The presence of new NVH sources in the vehicle, as well as the absence of the typical mechanical ones, makes the

electric vehicle a sensitive platform that should be studied carefully [2]. The well-established Source-Transfer-Receiver approach proves to be very valuable to assess the various consequences related to hybrid/electric drivetrains and associated vehicle system design challenges [3]. The development of new materials and structural configurations can help to achieve the driving conditions expected by EV's potential users (see more on chapter 1).

Some important aspects should be considered to guarantee the optimal NVH conditions of the incoming new generation of vehicles.

On one hand, regarding the vehicle interior behaviour, a relevant current trend is how the absence of mechanical sounds can affect the use of the vehicle in urban environments and how electric components, especially at high frequencies, can be perceived by the driver and the passengers. Regarding that, the NVH refinement is especially important on the powertrain development and vehicle integration process [4], as well as on the conflict that may occur between vehicle chassis and powertrain teams regarding NVH issues when developing future electric and hybrid technologies [5]. Previously, the internal combustion engine could mask much of the drive train noise; however, in hybrid and electric vehicles this is no longer the case. Similarly, the study and use of new light materials can help to adapt the cabin surrounding and prevent the vibro-acoustical noise transmission [6].

On the other hand, the very low level of exterior noise radiated by a low-speed approaching electric or hybrid vehicle [7] is a recognised danger for other vehicles, pedestrians and cyclists. Particularly children, elderly and blind people are especially affected by the lack of sound, even though this absence of sound is welcoming for the environmental regulations. In order to achieve a compromise, several manufacturers and research teams have developed external noise generators for such vehicles but two outstanding issues remain. First, how a significant warning level can be generated in front of the vehicle, without generating significant environmental noise pollution by radiating high noise levels from the sides and rear of the vehicle. The second issue is concerned with the best character of the warning noise to use. This should be perceived to be coming from a vehicle but not as alarming that it will cause a startle reaction and thus increase the danger. In the same way, and before the study of the influence of warning sounds, the global noise impact of such new vehicles in national road configurations has been evaluated [8] on different driving conditions.

This chapter compiles some important contributions that can help to increase/improve the NVH knowledge of EVs and HEVs. Some of these contributions are focused on the adaptation of NVH technologies from ICE to EV and HEV. Compared to traditional internal combustion engines, electric engines translate and enlarge the noise spectrum to a much higher range, changing a priori the testing conditions.

2 Methodologies and experimental contributions to the study of EVs

According to the objective of this chapter, several issues related to NVH experimental methods have been studied and analysed in detail. Fig. 1 shows the main topics of this chapter.

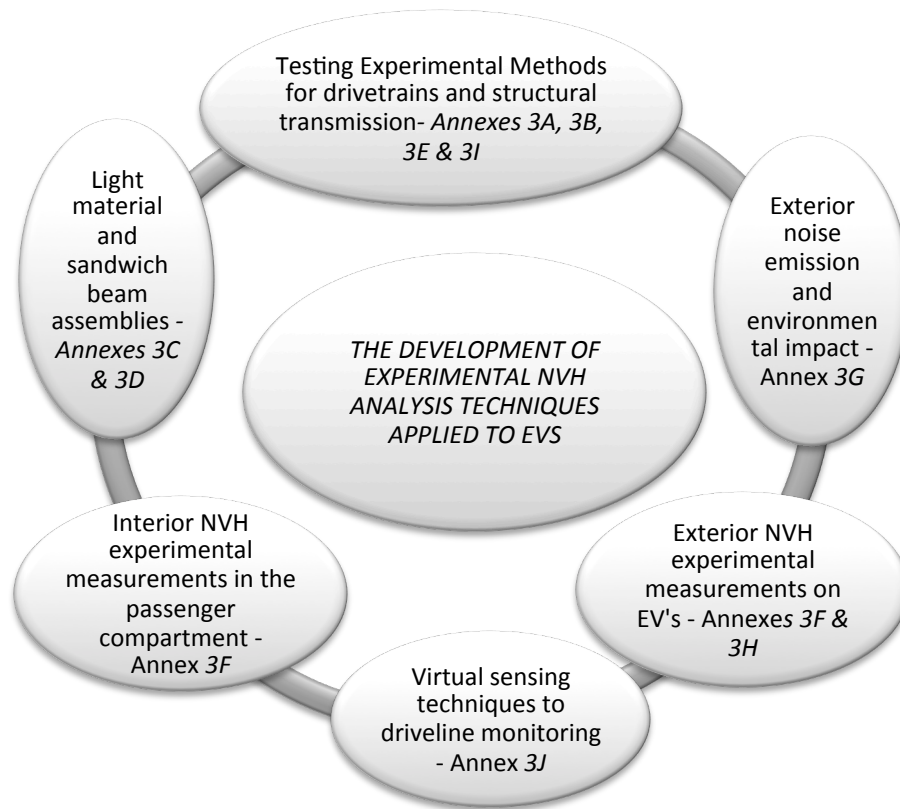


Fig.1. Main aspects of the experimental NVH study of Electric and Hybrid Electric Vehicles

Each input is presented as an individual annex, according to the following structure:

- 3A. NVH analysis techniques for design and optimization of hybrid and electric vehicles (TPA and OPA)
- 3B. Virtual sensing on mechatronic drivetrains using multi-physical models
- 3C. Numerical/experimental vibro-acoustic characterisation of lightweight materials using a novel test setup

- 3D. An inverse methodology for low-frequency transmission loss characterization of a lightweight panel in a small reverberant transmission suite
- 3E. NVH measurements on electric motors
- 3F. NVH investigations of hybrid urban buses (Sustainable noise reduction and enhanced passenger comfort using hybrid diesel-electric urban buses)
- 3G. Influence of electric vehicles in noise maps
- 3H. An innovative noise measurement method using OBSIe
- 3I. Multi-axial dynamic testing for design/functional/durability testing
- 3J. Experimental approaches for monitoring rotational dynamics systems

3 Conclusions

Some important achievements have been presented in this chapter, as well as suggestions for future work. Concerning the contributions compiled and related to experimental approaches for the NVH analysis of EVs and HEVs, the main conclusions are:

- Experimental methodologies have been applied for the structural path analysis of EVs. More specifically, the OPA and TPA methodologies can be satisfactorily applied to EV and HEV as demonstrated. More suitable testing conditions have been identified for each methodology and were compared to real testing measurements on an Electric vehicle, see *Annex 3A*.
- Combined input/state estimation on a mechatronic drivetrain has been presented, using experimental approaches and numerical models, see *Annex 3B*. The research points out how moving from a lumped-parameter drivetrain model towards a 1D-3D model would improve the accuracy and enlarge the scope of the applied estimation techniques. Future work will encompass validation on a test setup representing a general EV driveline subject to wheel loading. As such, the technique can be used to identify and quantify NVH problems related to drivetrain oscillations as a result of the interaction between operational wheel forces and possibly nonlinear drivetrain dynamics.
- In *Annex 3C*, the vibro-acoustic characterisation of lightweight materials, especially using a novel test setup for fast and easy characterisation of acoustic damping materials and lightweight panels, has been proposed. The employed setup allows for both acoustic absorptive materials and lightweight panels of different sizes. It shows a high versatility, where airborne (by means of a full-range speaker) or structural (by means of an electro-dynamic shaker or an impact

hammer) excitation can be applied and the response can be measured either acoustically (by means of microphones or intensity probes) or structurally (by means of lightweight accelerometers).

- As the main conclusion of *Annex 3D*, the proposed procedure has shown the capability to accurately estimate the mobility matrix of a homogeneous aluminium plate by mean of an indirect approach. As part of the future work, it is expected to validate the proposed approach by a set of experiments made on an aluminium homogeneous plate coupled to a small rectangular cabin located at ViF's (Virtual Vehicles) laboratory in Graz.
- Annex 3E discusses the measurement challenges related to the electric motor power source. NVH characteristics are determined not only by the type of motor but also by the power electronics and motor control strategy. The result are unique signatures in totally different frequency zones and characteristic modulation patterns unlike these encountered with ICE powered vehicles. As result, the nature of the NVH problems as well as of suitable noise control measures is very different, requiring to include the (H)EV nature of the drivetrain from the start in the vehicle design to come to an optimal design.
- In *Annex 3F*, after some experimental procedures, it is concluded that buses with an electric powertrain offer promising results on noise and pollutant emissions in the area of public transportation. Regarding the exterior noise, the analysis of the experimental data has shown that electric buses reduce noise emissions in the low speed area up to 15 km/h. At higher vehicle speeds, the reduction is not significant due to the tire-/road and wind noise. Also in the resulting interior noise and vibrations, the sound pressure level is in average reduced by 14 dB, considering the maximum difference by 20 dB. This objective measured improvement is reflected in a survey, that essentially results that a high percentage of passengers (80 %) have rated the HEV bus ride as more comfortable compared to a conventional diesel bus.
- The potential effect of Electric Vehicles in noise maps (with and without warning sounds) has been justified and modelled, having studied different traffic conditions with an adaptation of the French Noise Prediction Model NMPB ROUTES, see *Annex 2G*. The main conclusions point to a maximum reduction of noise pressure levels of 2 dB(A) in roads with 30km/h speed (without heavy traffic) and an expected improvement of 10% of population exposure to sound pressure levels lower than the limit of Spanish legislation.
- On *Annex 2H*, the OBSIe method has been used to evaluate some external aspects concerned with NVH on EV, HEV or FCEVs, like tyre/road noise and warning sound signals outside the vehicle. In the future, there are extensive plans on performing analysis of not only noise generated outside the vehicle, but also to analyse the noise inside the car, as regards different pavement types, different tyres or different measuring conditions.
- Due to the specific characteristics of EVs (the new powertrain components and a different mass and inertia distribution), *Annex 2I* proposes a multi-axial dynamic testing procedure using the CUBE 6 DOF hydraulic shaker to characterize the NVH behaviour of a vehicle.

- Finally, the contribution of *Annex 3J* shows that embedded power buffers in EV drivelines can enhance the efficiency of the EV itself. A potential palliative is integrating flywheels in EV drivelines. This research deals with the application of virtual sensing techniques to driveline monitoring. The achievements can contribute to the accurate and on time fault detection in EV drivelines.

4 References

- [1] IHS Online, Global Production of Electric Vehicles to Surge by 67 Percent This Year, Southfield, Michigan, 2014.
- [2] Lindberg, E., Hörlin, N., Göransson, P. An experimental study of interior vehicle roughness noise from disc brake systems, *Applied Acoustics* 74-3(2013) 396-406.
- [3] H. Van der Auweraer, K. Janssens, A Source-Transfer-Receiver Approach to NVH Engineering of Hybrid/Electric Vehicles. SAE paper 2012-36-0646, Proc. SAE NVH Brazil, Florianopolis, Brazil, 2012
- [4] Govindswamy K., T. Wellmann T., G. Eisele G. Aspects of NVH integration in hybrid vehicles. SAE Paper 2009-01-2085, 2009.
- [5] Bryant, M. Solving nvh issues in hybrid and EV powertrains, Transmission Engineer, Drive System Design Ltd, United Kingdom.
- [6] Pluymers, B., Desmet, W. Design and dynamic characterization of lightweight materials that meet automotive NVH targets, 8th International Styrian Noise, Vibration & Harshness Congress, Graz, Austria, 2014.
- [7] Pallas, M.A., Chatagnon, R., Lelong, J. Noise emission assessment of a hybrid electric mid-size truck, *Applied Acoustics* 76(2014) 280-290.
- [8] Pallas, M., Chatagnon, R., Lelong, J. Acoustic assessment of a passing-by hybrid distribution truck, INTERNOISE 2012, New York.

Annex 3A

Transfer Path Analysis for vehicle NVH refinement: Application on EV / HEV vehicles

Alfonso Fernández del Rincón¹, Alberto Diez-Ibarbia¹, Mattia Battarra², Juani Palenzuela³, Gines Cervantes³, Stephen Walsh⁴, Stephanos Theodossiades⁵

¹Structural and Mechanical Engineering Department, University of Cantabria, Av Los Castros s/n - 39007, Santander, Spain. alfonso.fernandez@unican.es,

²Engineering Department, University of Ferrara, Via Saragat, 1 - 44122, Ferrara, Italy, mattia.battarra@student.unife.it,

³Mechanical Engineering and Energy Department, Miguel Hernández University of Elche, Av de la Universidad, S/N - 03202, Elche, Spain, ginescm@gmail.com,

⁴Department of Aeronautical & Automotive Engineering, Loughborough University, Loughborough LE11 3TU, UK, S.J.Walsh@lboro.ac.uk,

⁵School of Mechanical and Manufacturing Engineering, Loughborough University, Loughborough LE11 3TU, UK, S.Theodossiades@lboro.ac.uk,

Abstract. In the current framework, hybrid and electric vehicles have the advantage of polluting the environment less than other conventional technology-based vehicles, nevertheless one issue of concern has been the noise impact that they generate. The main objective of this proposal is to improve the acoustic perception of the driver in the cabin. This is the reason why Transfer Path Analysis and Operational Path Analysis methods were performed in an electric vehicle. A comparison between both methods taking into account the structure-borne paths from the motor and the suspension points to the cabin has been performed. One of the aims of this study is to check the versatility of these methods, commonly used in petrol engine cars. This assessment includes the analysis of the noise contribution of each path depending on the frequency and vehicle speed range and moreover, the path noise impact for harmonic excitation due to the physical components of the electric vehicle.

3A.1 Introduction

NVH issues in vehicle design have been receiving increasing interest from the manufacturers during last decades. An interesting testimony of this fast development can be found in [1] where the author describes how a small NVH department composed by about 12 engineers with limited testing facilities was increased in only 5 years up to a team about 90 persons working in a new center with more than 15 additional facilities.

One of the reasons for this success can be found in the market and in the necessity of providing quiet and refined NVH vehicles to satisfy customer demands. The development of more advanced, powerful and cheaper technologies for NVH measurements jointly with the necessity of reducing the time expended in trial and error

test has been a fruitful context where several NVH analyses techniques were developed.

One of these techniques was the so called Transfer Path Analysis (TPA) which main aim was the identification of the individual contributions via different transmissions paths from “sources” as powertrain or wheels to the “receivers” which will be the passengers. This identification provides the basis for further troubleshooting and product improvement from the point of view of NVH. Moreover in spite of automotive industry has been the field where TPA has proven their utility; its use has been extended to other sectors as printers, refrigerators, ships, wind turbines, helicopters and aircrafts [2].

In this chapter the main questions concerning TPA will be described and the current available approaches to carry out this kind of analysis in practice will be presented. Afterwards, the main concerns regarding their application in EV / HEV will be reviewed. Then a case study corresponding to the experimental test carried out at Loughborough University on the EV provided by PSA group will be discussed. Finally some preliminary conclusions from the results obtained will be presented.

3A.2 Techniques for TPA

There are several terms to describe the same kind of technique. Source Path Contribution (SPC) [3-4] or Noise Path Analysis (NPA), are also common acronyms used to designate the same technique. The former techniques used for this kind of analysis were developed in the late 70’s and it was initially based on analysis of coherence between signals coming from several channels [5]. But it was during 80’s that the so called classic TPA was described in [6].

According to the classical approach the system can be divided in an active part and a passive part (or a source part and a receiver part) which are connected together by some kind of interface [7]. The objective is to be able to discern what contribution is due to each transmission path considering both structural and acoustic paths and how excitation is transmitted towards the reception point.

Classical TPA approach considers that the response ($R(\omega)$) at a certain location (and at a certain frequency) can be obtained as an addition of contributions due to different paths, structural or acoustical according to the expression, Eq. 1-A.

$$R(\omega) = \sum_{i=1}^n FRF_i(\omega)F_i(\omega) + \sum_{j=1}^r NTF_j(\omega)Q_j(\omega) \quad \text{Eq. 1-A}$$

1-A

Where FRF_i denotes the Frequency Response Function between the receiver and an input force at location i (F_i) while NTF_j represents the Noise Transfer Function between the receiver and the acoustic load (Q_j).

Thus if operating excitations (F_i and Q_i) and transfer functions (FRF and NTF) are known it is possible to determine what is the contribution of each path as well as the frequency range where this contribution is more important. If there is not missing

paths in the analysis, the synthesized response and the measured one should be nearly the same and therefore this provides a simple mean for validating the analysis.

Nevertheless there are some important problems involved in the application of classical TPA. Two steps are necessary to build the expression (Eq. 1-A): i) measuring excitations in operational conditions and ii) determining transfer functions.

Measuring operational excitations

Measuring operational excitations is a complex task in real systems as it is the case of automobiles. Due to space restrictions and practical issues usually it is not possible to measure operational excitations directly by a simple transducer like a load cell. In fact that is one of the main practical problems concerning real TPA applications. To circumvent these difficulties two main techniques have been proposed: the mount stiffness method and the so called inverse force identification method.

The mount stiffness method

The mount stiffness method is useful when active and passive parts are connected by simple flexible joints. In these cases, operational forces are obtained from the movement (usually acceleration) of the input and output sides of flexible mounts, applying Eq. 2-A, under the assumption that its dynamic stiffness $K_i(\omega)$ it is known.

$$F_i(\omega) = K_i(\omega) \frac{a_{ai}(\omega) - a_{pi}(\omega)}{-\omega^2} \quad \text{Eq.}$$

2-A

Determination of dynamic stiffness of flexible mounts requires specific test procedures as their behaviour is strongly non linear by nature and it is necessary to consider different load levels reproducing the real operating conditions. Moreover dynamic stiffness involving cross coupling effects should be defined in modern set ups making much more difficult their test and assessment. As a consequence dynamic stiffness method usually does not solve the problem and instead it includes more uncertainty in the TPA analysis.

Inverse force identification

In order to avoid the direct measurement of forces, theoretically it is possible to obtain it from the measured response from a certain number of locations in the structure.

$$H_{jk}(\omega) = \frac{a_{qk}(\omega)}{F_k(\omega)} \quad \text{Eq.}$$

3-A

When the number of measured response locations is equal to the number of unknown forces, the resulting frequency response matrix is square and it is possible to obtain the corresponding force by its inversion according to

$$\{F(\omega)\} = [H(\omega)]^{-1} \{a_q\} \quad \text{Eq.}$$

4-A

Nevertheless, while it is possible to calculate a unique response from known excitations, the inverse problem is not straightforward as the same response could be produced with a different forcing history. Moreover, practical application of this theoretical concept does not provide acceptable results likely due to the ill-condition of the frequency response matrix at frequencies near the resonances [8]. As a consequence significant errors are committed when matrix is inverted and therefore the results become not useful. To avoid this problem several numerical techniques have been proposed involving a redundant number of measurement points (some authors [9] claims the overdetermination factor should be at least 2). Thus, if response is measured in q locations while loads are applied in p sites, the relationship between responses and excitations will be given by

$$\left\{ \begin{matrix} a_q \\ (q \times 1) \end{matrix} \right\} = \left[\begin{matrix} H(\omega) \\ (q \times p) \end{matrix} \right] \left\{ \begin{matrix} F(\omega) \\ (p \times 1) \end{matrix} \right\} \quad \text{Eq.}$$

5-A

Arriving to a formulation where a rectangular matrix (H(w)) should be inverted. Pseudoinverse and Singular Value Decomposition (SVD) are techniques, which have been applied by researchers to accomplish this task [10-11]. Thus, the force can be obtained from the accelerations by

$$\{F(\omega)\} = [H(\omega)]^+ \{a_q\} \quad \text{Eq.}$$

6-A

Where H(ω)⁺ represents the pseudoinverse. The application of this procedure can be compromised by different kind of errors as inaccuracies and noise in the experimental measurements as well as insufficient, inadequate or inaccurate sensor data.

Determining transfer functions

On the other side, determining transfer functions usually requires dismounting the active part assuming that the behaviour of the passive part remains the same. This task is time consuming and the last assumption is not always acceptable. Several excitation techniques can be used in this task (shakers, loudspeakers or impact hammers) and commonly the reciprocity principle is applied due to space restrictions in the connection points between active and passive parts. It can be noted that if the

load identification method uses the stiffness or matrix approach, the FRF can be performed at the same stage, measuring the acoustic pressure as well as the accelerations.

Once the transfer functions have been determined, the response at the receiver might be predicted by Eq.1-A. Then, it is possible to identify the contribution of each path to the response in the so-called partial path contribution (PPC) plot. This plot provides by rows the contribution of every single path as a function of frequency (or engine RPM). Care should be taken on the consideration of phase for each path and frequency as the interaction between paths could result in a lower value of the response.

In order to validate the procedure the predicted response is compared with the record actually obtained in the location of interest. Differences between recorded and predicted might be attributed to lack of paths considered in the analysis, inaccurate acquisition procedures and numerical problems involved in the approach used for force identification.

3A.3 Techniques for OPA

In spite of classical TPA is powerful and can be applied in a wide range of problems, some practical issues constrain its usefulness. The main drawback of this kind of technique is related with the amount of time necessary to complete the analysis. Mounting and dismounting tasks associated with the calculation of FRF as well as the inherent limitations on the measurement of forces have led researchers to the development of new techniques entirely based upon *in-situ* measurements. The main concern of these techniques is avoiding the identification of loads by measuring instead the response (commonly accelerations) at certain locations distributed near the loads and (or) along the transmission paths. In essence, this approach can be derived from the combination of equations 1 and 6 that focusing in structural paths and removing noise-related terms, for the sake of simplicity, becomes

$$R(\omega) = \sum_{i=1}^n FRF_i(\omega) [H(\omega)]^+ \{a_q\} \quad \text{Eq. 7-A}$$

As the main advantage of this kind of techniques is linked with the fact that only measurements of machinery in operation are required for characterization of system transmission paths, this group of techniques are commonly designed as Operational Path Analysis (OPA). Thus, in the case of multiple receivers $R_i(\omega)$, Eq. 7-A can be expressed in matrix form as

$$\{R(\omega)\} = [T(\omega)] \{a_q\} \quad \text{Eq. 8-A}$$

Where matrix $T(\omega)$ represents system transmissibility's between the reference points located in the structure and the target receivers. Despite the fact this method has shown some limitations due to the requirement of considering all the paths and using

low-coherence signals, companies are deeply interested in improving them because of the possibility of obtaining TPA-like results quickly.

In the following some possible approaches for OPA are briefly described,

Direct application of transmissibility concepts

Three main stages can be considered for the application of the most direct approach of OPA [12], i) Operational measurements, ii) Transmissibility function and iii) Results and assessment. Operational measurements are taken in the same way as was described for the TPA. With the acceleration and the acoustic pressure measurements, the transmissibility functions are calculated using Eq. 9-A.

$$R(\omega) = \sum_{i=1}^n T_i(\omega) \cdot a_i(\omega) \quad \text{Eq. 9-A}$$

9-A

Finally, the obtained results are assessed, determining which transfer path is the most critical one for a specific frequency.

Indirect application of transmissibility concepts

This method is a variation of the general OPA method previously explained and can be divided into three main stages, i) Operational measurements, ii) Frequency response function calculation and iii) Results and assessment. The main difference between these methods is that while in the previous one the transmissibility functions are calculated, in this method, the FRFs are calculated instead. This method is more theoretical than practical, because the applicability of these concepts in a vehicle has still to be proven. The fundamentals of this method are based on the application of the transmissibility concepts. According to [13], the key point to obtain the FRF without disassembling the system (in TPA this is a requirement) is to apply a known force in the subsystems of interest. In Fig. 1-A, the simplified model of the engine and body can be appreciated as an example of application. If the FRFs of the subsystems of interest need to be determined, the F1, F2 and F3 forces have to be known. This is a difficult task, because the devices used to introduce the excitation forces (hammers or shakers) on each subsystem are not designed to co-exist with the forces generated by the engine.

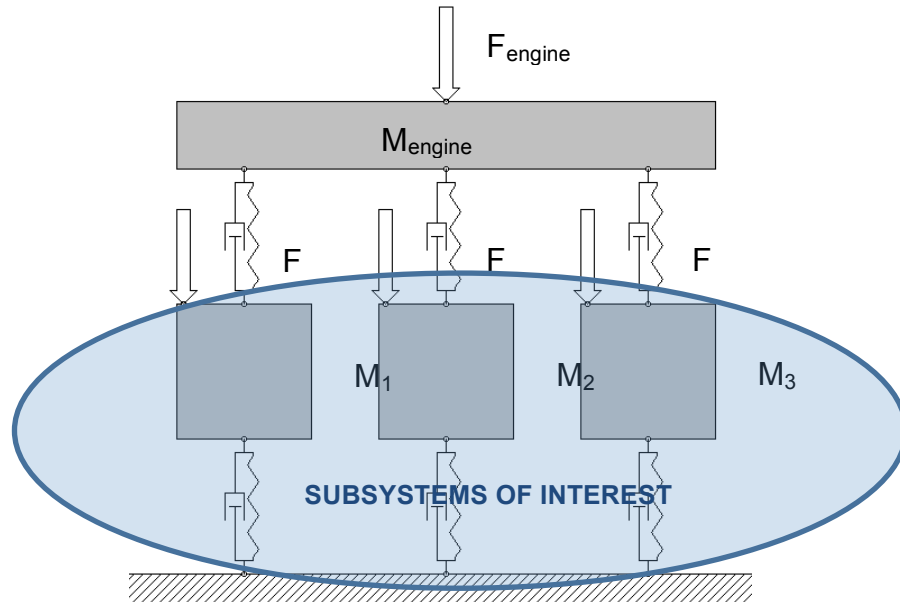


Fig. 1-A. Lumped model of a vehicle

OPA with exogenous inputs (OPAX)

This method is another variation of the general OPA method explained previously and can be divided in five main stages [14], i) Operational measurements, ii) Frequency response function iii) Parametric load model iv) Calculation of operational loads and v) Results and assessment.

The first stage is the same as in the OPA method obtaining the accelerations and acoustic pressure in operational conditions at the points of interest. Then (second stage), once the motor is removed, FRF procedure takes place in the same way as in the second stage of the TPA procedure.

In third stage, using the accelerations and forces obtained in the FRF stage, an exogenous force parametric model can be determined. To achieve this, the accelerations and forces are introduced in the chosen formulation (Eq. 10), calculating the parameters or constants of the equation.

$$F_i(\omega) = f(\text{parameters}, a_{ai}(\omega), a_{bi}(\omega)) \quad \text{Eq. 10-A}$$

Once the equation is solved and calibrated, the accelerations in operational conditions are introduced in the formula, allowing the simulated forces of the engine at the interest points to be found.

Lastly, the simulated acoustic pressure is determined by means of the transfer function (second stage) and the operational forces calculated in the previous stage.

Assessing whether the model is valid by the comparison between the calculated acoustic pressure and the measured one (first stage).

3A.4 Comparison between methods / approaches

In order to determine which method is the most suitable for this case study, the strengths and weaknesses of each method have been assessed:

TPA

STRENGTHS: The most important aspect of this approach is that the results are usually close to the real scenario. Moreover the validity of the results is easy to determine because a comparison between the real acoustic pressure value and the simulated one can be made. Another interesting aspect is that the cross-coupling effects, introduced when the engine is mounted, are always considered and an error is avoided.

WEAKNESSES: One of the main problems with this method is the execution time because a lot of tests hammer have to be used in order to determine every transfer functions. Also, in this case study, this method presents the further problem that the engine must be removed in order to perform most of the tests.

OPA (Direct)

STRENGTHS: This method has two main advantages. The first is that it is not necessary to calculate the loads that the engine is introducing in the system because the transmissibility functions do not require it. Following from the first advantage, a large numbers of tests are not required making this method the quickest and at the same time the easiest.

WEAKNESSES: Although this method is the easiest and quickest, it might produce more problems because of the difficulties that are presented in its validation. The first weakness is the estimation of the transmissibility matrix because the inverse acceleration matrix is needed. To solve this problem an estimator is usually used (H1 estimator) and the input forces are limited to low-coherence. Unlike the TPA method, cross-coupling affects the transmissibility function hugely, for this reason low cross-coupling is required to obtain reliable results. Also this method is sensitive and all the active paths must be considered in order to obtain valid results. This is because the contribution of the missing path is added to the rest paths.

OPA (Indirect)

The strengths and weaknesses of this method are similar to the previous one but there is a main difference. To perform this method, the forces of the isolated subsystems of interest must be known.

OPAX

STRENGTHS: Measurements are simpler compared to the traditional matrix inversion TPA method because mount stiffness data is not required. On one hand the estimated parametric model of forces used allows the determination of additional information such as dynamic stiffness and forces in other operational conditions by introducing other accelerations. On the other hand, it is more accurate than dynamic stiffness method way of load calculation.

WEAKNESSES: One of the main problems with this method is the execution time, although it spends less time than the classical TPA, it is more time consuming than general OPA. Also, in this case study, this method presents another problem which is that the engine must be dismounted in order to perform most of the tests.

Conclusions

With regard to all the information gathered from the literature review, a ranking of the different methods studied has been done. In this ranking, different general aspects have been taken into account and shown in the Table 1-A.

Table 1-A. Ranking among passive transfer path methods

GENERAL ASPECTS	TPA	OPA	OPAX
SPEED	3	1	2
ACCURACY	2	3	1
LESS COMPLEXITY	2	1	3
EASY TO VALIDATE	1	3	1

3A.5 Particular issues of application TPA in HEV / EV:

Electric vehicles (EV) are typically quieter than comparable Internal Combustion Engine (ICE) vehicles. However, they do produce a significant amount of higher frequency tonal noise than traditional ICE vehicles. For example, whining tonal noise from electric motors and generators is typically in the frequency range 400-2000 Hz [15]. Once elements of the EV powertrain are included then the whining tonal noise can be produced up to 3000 Hz [16-17] note that the engine orders excited by an

electric drive are higher than for those of an ICE engine, thus, leading to higher frequency interior noise in an EV.

Since the noise from an electric powertrains is no longer restricted to the low frequency region of a traditional ICE, it can be expected that the transfer paths from the powertrain to the vehicle interior now include a relatively stronger contribution from the airborne paths rather than being dominated by the structure borne paths as in a traditional ICE powertrain architecture [18].

Florentin et al. [19] report a comparison of the noise from a small conventionally powered vehicle and a similar sized electric vehicle. As expected, the EV is quieter than the ICE vehicle at low and medium speeds. However, at high speeds the high frequency ringing from the EV can exceed the ICE noise in certain frequency bands. Also, at high speeds the tonal EV noise was perceived as more annoying even in the frequency bands where the measured sound was less than for the ICE vehicle.

A further problem is that without the masking noise of the ICE the sound from the auxiliary components (pumps, inverters etc.) of an electric vehicle are noticeable even at low speeds [9].

Hybrid electric vehicles also present novel challenges. For example, the transition between the electric and the combustion engines stages of operation of a hybrid EV can produce unfamiliar sounds for the driver and passengers [20].

3A.6 Case of Study

TPA techniques have been applied in a vehicle demonstrator in order to validate its usefulness in EV and provide output for the other WG involved in the project. The vehicle under test is based in the Mitsubishi i-MiEV car which variants are also sold in Europe by PSA Peugeot Citroën (PSA) as the Peugeot iOn and Citroën C-Zero. It is a five-door hatchback electric car, driven by a single permanent magnet synchronous motor in the rear axle powered by a 16 kWh lithium-ion battery pack. The vehicle uses a single-speed reduction gear transmission driving the rear wheels and the motor and batteries are water cooled by a conventional radiator with an electrical fan disposed in the front of the car.

Objectives

The main objective of the work carried out on the car under test is demonstrating capability of experimental available methods and techniques to be applied in a real electric vehicle development context (interior noise).

In this context and taking into account the means available for these task two particular objectives were defined as the following:

1. Identify noise sources: Develop and apply techniques to separated annoying tonal or multi-tonal sources (electric motor, control system, gear ratio, differential) from broad-band noise (road noise and aerodynamic noise).

2. Apply TPA techniques in order to define and assess the structure-borne paths for identified sources in targeted operative conditions on a roller bench.

Test description

In order to implement both the TPA and OPA methods, some test were performed. In the case of study, two kinds of test were executed, tests in operating conditions on a roller bench and impact tests on a bay lift.

Measurement points location

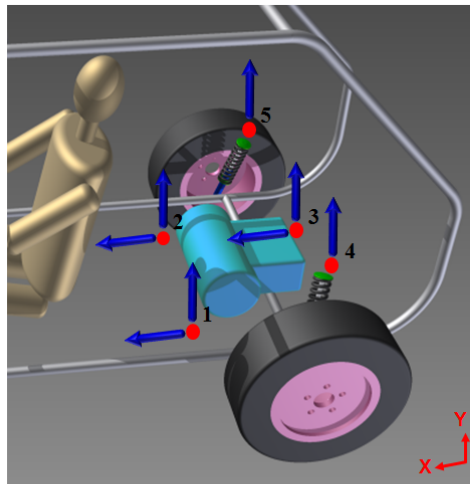


Fig. 2-A. Measurement point locations

The first stage to carry out these tests is to locate the transducer depending on the requirements of the measurements. In this case, since the noise perceived by the driver in the cabin wants to be assessed, a microphone in the driver’s seat was located. The speed of the wheel shaft was necessary for the analysis stage, therefore a laser tachometer were installed in the rear wheel shaft. Furthermore, it was envisaged that the motor and the road (through the suspensions) generated most of the noise in the cabin. This is the reason why, 8 accelerometers were strategically located in the motor mounts (6 accelerometers) and suspensions (2 accelerometers) in the directions presented in Fig 2-A.

In order to clarify the nomenclature and the location of each accelerometer, the Table 2-A is presented, where the information of each accelerometer is shown.

Table 2-A. Location of the accelerometers installed and their directions on the vehicle.

LOCATION	POINT	DIRECTION	ASSOCIATED
----------	-------	-----------	------------

			PATH
Engine mount 1	1	Vertical direction(Y)	1 st
Engine mount 2	2	Vertical direction(Y)	2 nd
Engine mount 3	3	Vertical direction(Y)	3 rd
Suspension 1	4	Vertical direction(Y)	4 th
Suspension 2	5	Vertical direction(Y)	5 th
Engine mount 1	1	Axial direction (X)	6 th
Engine mount 2	2	Axial direction (X)	7 th
Engine mount 3	3	Axial direction (X)	8 th

Test 1: Roller bench with motor switched off

This test was performed on the roller bench with the electric motor switched off. This means that the roller bench provided the energy to the car. Three different specifications were used in this kind of test which are shown in Table 3-A.

Table 3-A. Test specifications.

N° accelerometers	Minimum speed (km/h)	Maximum speed (km/h)	Acceleration (km/h/s)	Noise outside (dB)
3	5	60	3	45
5	5	60	3	45
8	5	100	5	45

It can be noticed that all of them are not in stationary condition. In fact, in order to carry out an OPA, which analyses a wide range of speed, it is necessary to measure vibrations and noise while the vehicle is doing a run-up. This kind of test was performed mainly because some issues with the data acquisition system occurred during the roller bench test 2 which is going to be presented.

Test 2: Roller bench propelled by the EV

In this test, the car motor provided the energy to the system. The specifications of the test performed are gathered in Table 4-A.

Table 4-A. Test specifications.

N° accelerometers	Minimum speed (km/h)	Maximum speed (km/h)	Acceleration (km/h/s)	Noise outside (dB)
8	5	100	5	45

It can be noticed that all of them are not in stationary condition. In fact, in order to carry out an OPA, which analyses a wide range of speed, it is necessary to measure vibrations and noise while the vehicle is doing a run-up. This kind of test was performed mainly because some issues with the data acquisition system occurred during the roller bench test 2 which is going to be presented.

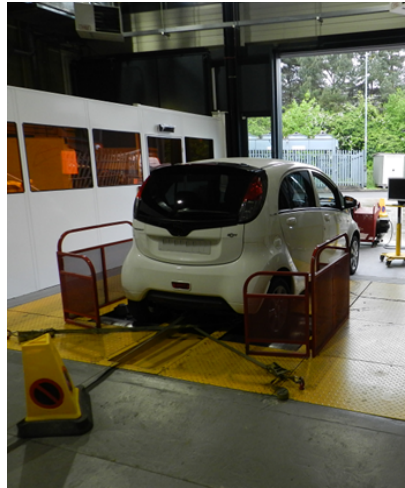


Fig. 3-A. Vehicle under test mounted on the chassis dynamometer (roller bench)

This kind of test was utilised to identify the noise sources and to calculate the transfer paths in the OPA and TPA methods.

Test 3: Impact test

This test was performed with the car on a bay lift, therefore in static conditions. The performance of this test was exciting the different points of interest with a test hammer as the same time as the data acquisition system is collecting all the required data. In this case, the force introduced by the hammer was measured by the force transducer as well as the accelerometers and the microphone were measuring in the considered points.

Data acquisition

As commented, to collect all the data measured by the transducer, an acquisition system was needed. In this case, the acquisition equipment was: Brüel & Kjaer, accelerometers type 4517-002 DeltaTron and Brüel & Kjaer microphone Type 4942-A-021 were used with a Brüel & Kjaer Type 2693-0s4 signal conditioner. All this equipment was checked by laboratory calibrators.

All signals were sampled and acquired by National Instruments acquisition card cDAQ-9178 + 2x National Instruments 9215 drive by a home-made virtual instrument developed in LabVIEW code (see Fig. 4-A).

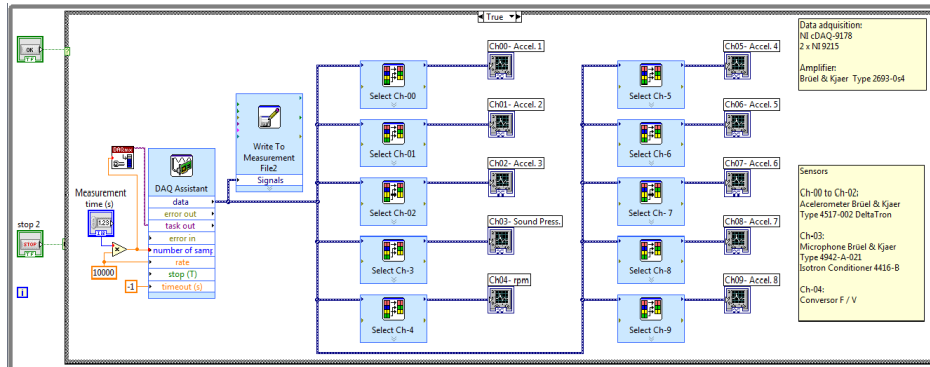


Fig. 4-A. Application to record data in LabVIEW software

Additional tools were developed in MATLAB environment in order to process the recorded signals. A specific script was made in order to plot the different acquired signals on a graph, in time domain; in this way it was possible to focus the attention only on the region of interest (the run-up). After that, a Short Time Fourier Transform was applied to each signal in order to accomplish a time-frequency analysis. This technique enables to find the natural frequencies of the system and, at the same time, determine the most excited orders. The script was created with the possibility to modify the width of the time's window and the overlap in each analysis.

Identification of noise sources

In order to complete this objective the following guidelines were defined:

- Identify source signals from a colour-map or similar plot by simply extract the relevant order from the experimental data in the frequency domain.
- Pay special attention to tonal and multi-tonal sounds coming from gears and electric devices, which are subjectively the most annoying noise in EV.

This task was carried out using the colour-maps obtained from the run-up records of Test 1 (electric drive switch off). In Fig. 5-A, the results corresponding to the measurement lay out with 5 accelerometers are shown. Acoustic pressure recorded inside the vehicle -at the driver location- is presented at the bottom on the right.

According to previous results and the dynamic behaviour of motor-gearbox system, three main natural frequencies are expected, one in the region between 200 and 250Hz, one between 600 and 650Hz and one more between 700 and 800Hz. These frequency regions can be recognized in acoustic pressure measurements and more clearly, as expected, in the acceleration records (see Fig. 5-A).

A more detailed view for the low frequency region is presented in 6-A. In the upper side, the attention is focused on the orders between the 8 and the 48. As expected, the

orders 10.71 and 25 are clearly recognizable because related to the gearbox, while the orders 8 and 48 are not excited because related to the poles of the engine that was switched off.

Attention should be paid to orders 0.16, 0.49 relative to the first order, which is the spin velocity of the engine shaft. Order 0.16, that appears to be the most excited, is related to the spin velocity of the tires and the order 0.49 is his third harmonic. With this analysis of the results coming from the measured data it was possible to consider them validated and ready for the second part of the post-processing, made by another research group.

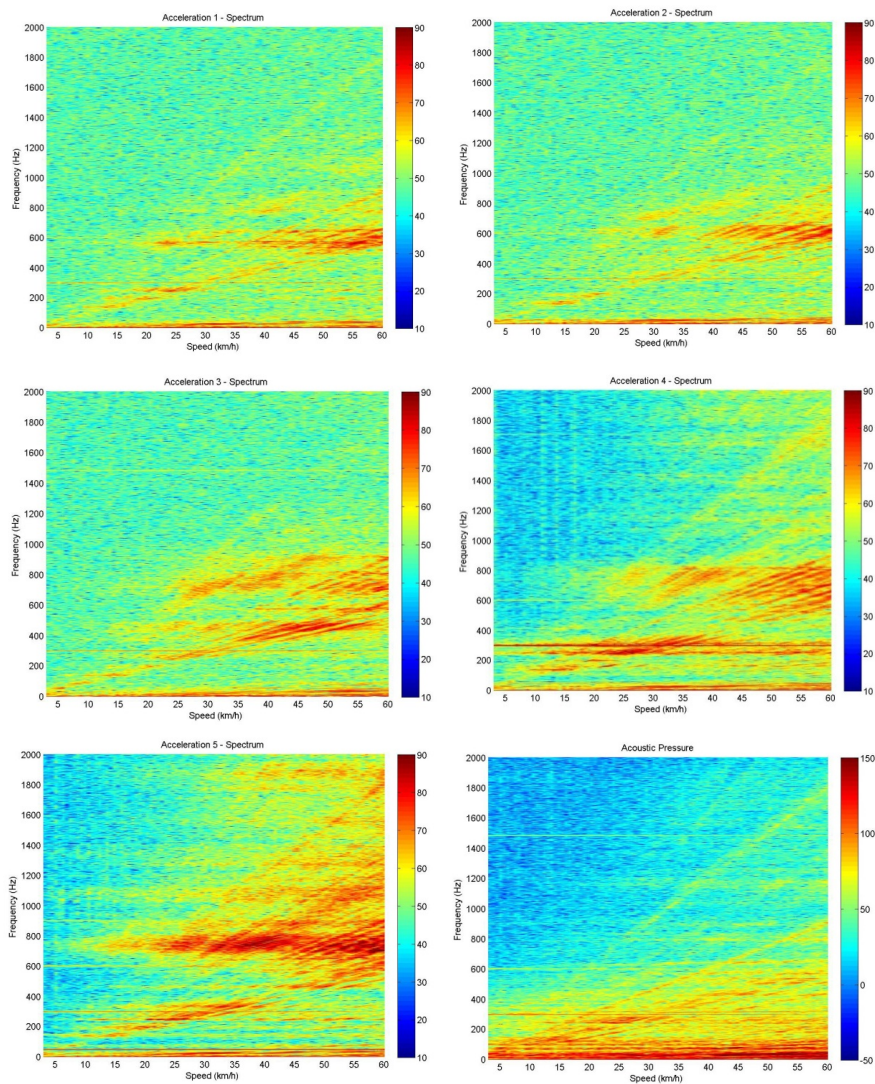


Fig. 5-A. Run-up results in Test 1 (5 accelerometer). Acoustic pressure (lower-Right)

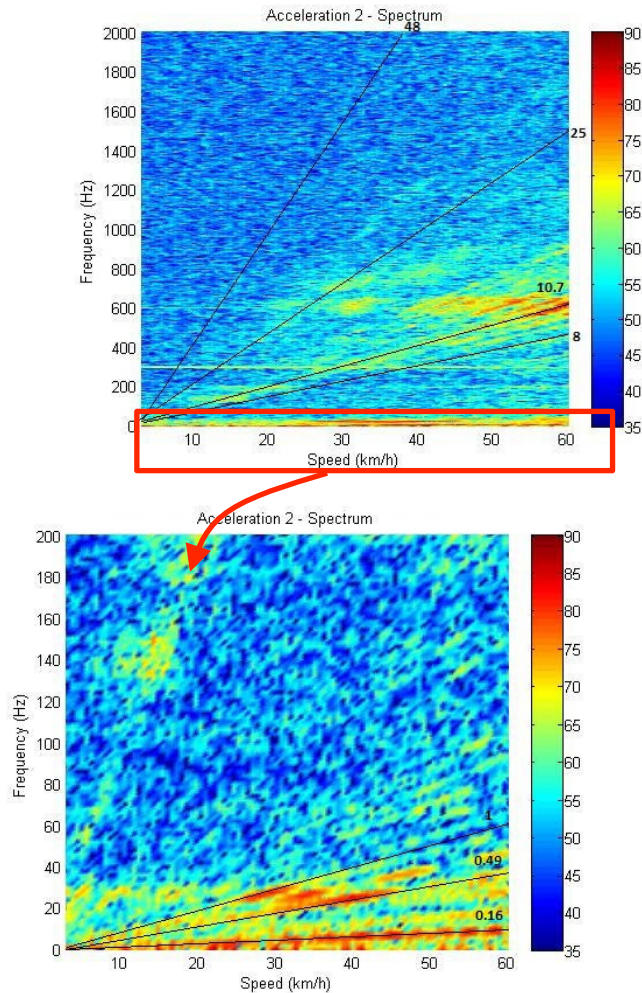


Fig. 6-A. Detail in the low frequency region (engine mounting 2 accelerometer)

OPA results

In this section, the procedure to obtain the OPA results is to be explained firstly, assessing the results lastly. To perform the OPA method, two operational tests are necessary. With the first one, the transmissibility functions are calculated and with the second one the validity of them is checked. The procedure to calculate the transmissibility functions requires the accelerations and acoustic pressure gathered in the acquisition data stage and transforms them to the frequency domain. Once this transformation is done, the transmissibility functions are calculated by a mathematical

method based on H_1 estimator. Once they are calculated, the acoustic pressure of the other operational test is calculated by the new accelerations and the transmissibility functions. Finally, this computed acoustic pressure is compared with that measured in the second test, checking the validity of the procedure.

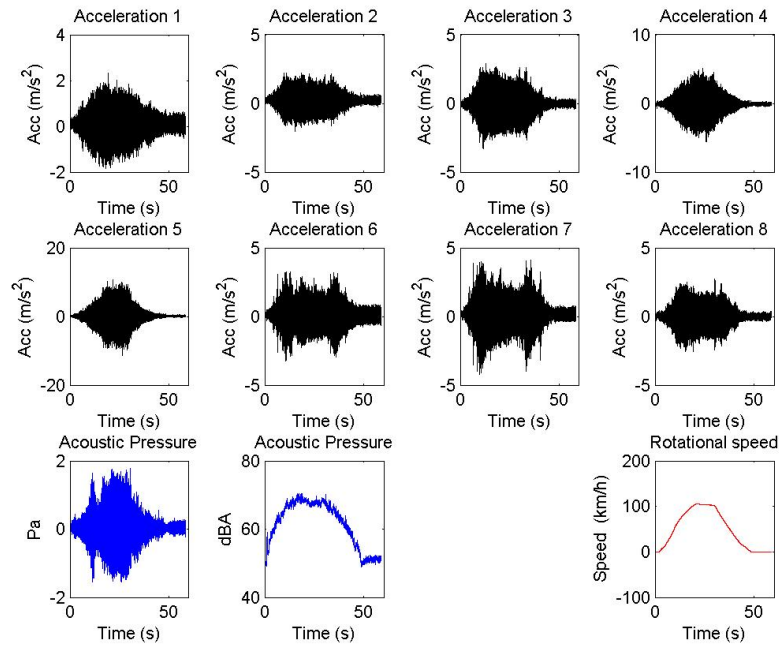


Fig. 7-A. Time-domain accelerations (6 on the motor mounts and 2 on the suspensions), acoustic pressure inside (in Pascal and dBA) and wheel rotational speed

In Fig. 7-A, it can be shown the typical set of results obtained from the measurements in Matlab environment. To calculate the OPA, the first step is to obtain each transmissibility functions by means of the H_1 estimator procedure. This procedure requires the auto-spectrum and the cross-spectrum of the accelerations and acoustic pressure measured to calculate these transmissibility functions. In Fig. 8-A, the transmissibility functions in the frequency domain can be seen.

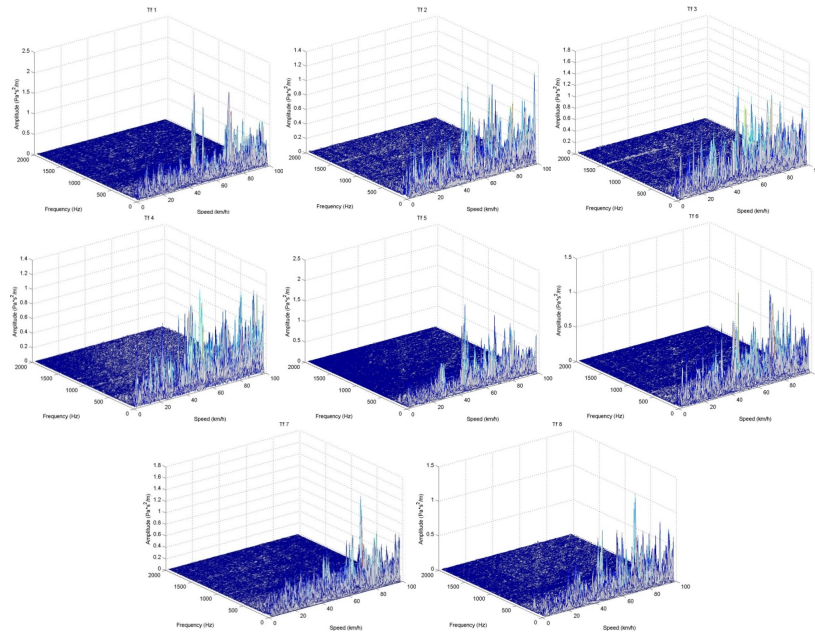


Fig.8-A. Transmissibility functions

In order to check that the mathematical procedure was precise, the calculation of the acoustic pressure and the real measurement has been compared and shown in Fig. 9-A in the frequency domain.

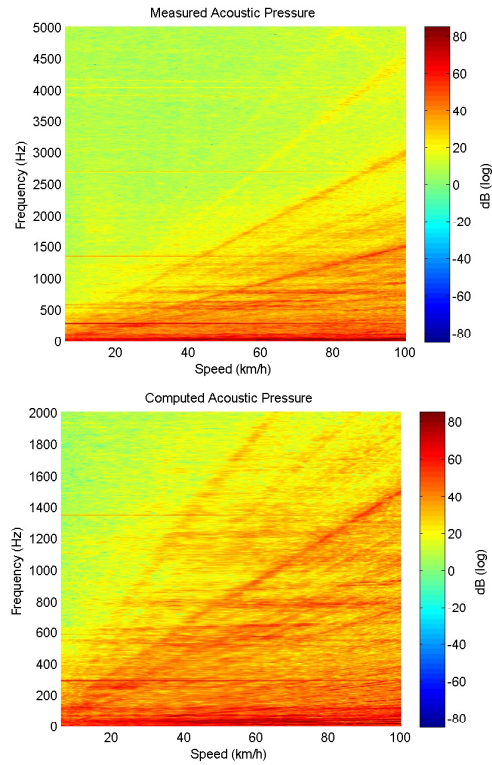


Fig.9-A. Measured and computed acoustic pressure

The next stage is to assess which path affects more inside the pilot's cabin. In Fig 10-A, the contribution of each path is presented depending on the speed and frequency case of study.

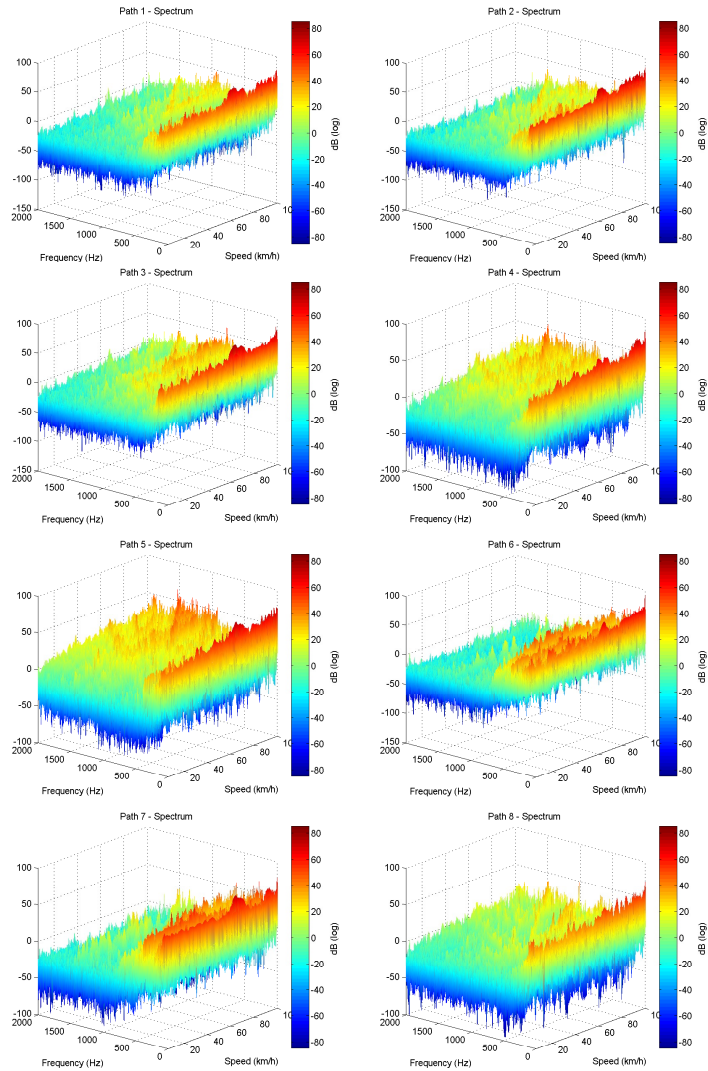


Fig.10-A. Acoustic pressure of each transfer path in the frequency spectrum

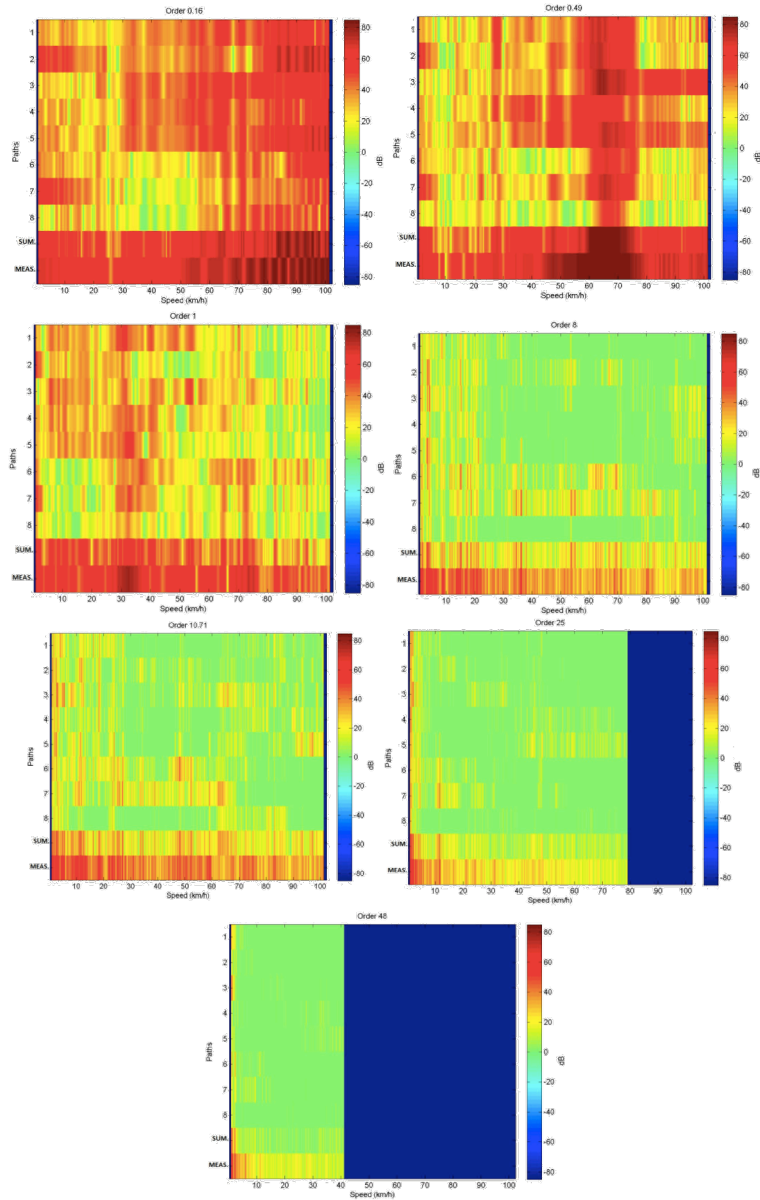


Fig.11-A. Path analysis for the orders of interest

The last stage was to extract the amplitude values of the different orders of interest, Fig. 11-A. Specifically, the orders case of study has been: 0.16 related to the wheel, 0.49 related to the third harmonic of the wheel, 1 due to the rotation of the motor, 8 due to the poles of the motor, 10.71 and 25 due to the gear transmission and 48 due to the coils of the stator.

TPA results

In this section, the TPA results are to be shown and assessed. The methodology consists in the post-processing and assessment of two different tests, impact and operational tests as is detailed next. The impact tests were performed with the electrical vehicle on a bay lift to calculate the frequency response functions (FRF) between accelerations and forces first and between forces and acoustic pressure next. Once the paths have been characterized, the operational measurements are used to validate this functions and if new paths need to be considered by the calculation of the acoustic pressure and comparison with the measured one. The acoustic pressure is calculated using the accelerations obtained in operational test and multiplying it by the acceleration-to-force FRF (the equivalent forces are calculated) and then multiplying the results by the force-to-acoustic pressure FRF.

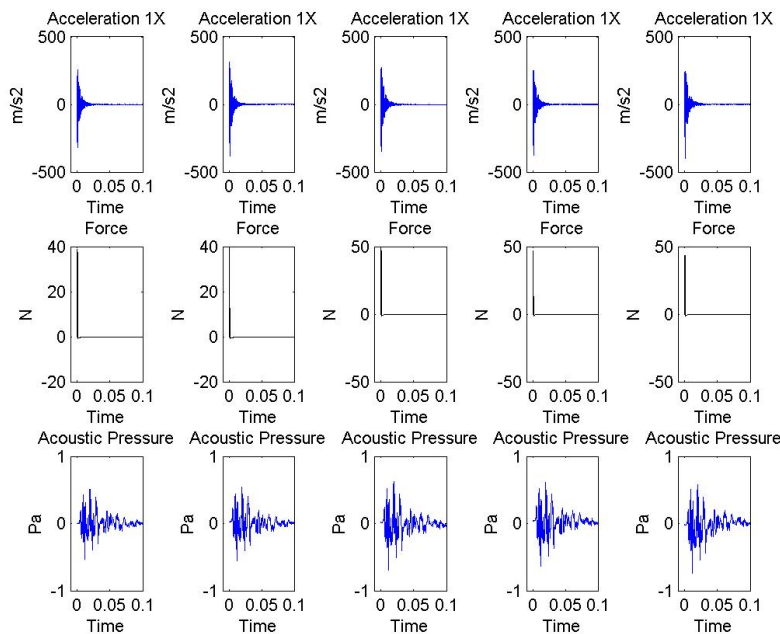


Fig.12-A. Impact test example

From the several impact tests in all the points of interest, five of these impacts have been gathered randomly. As an example, the five impacts in the point 6, the respective accelerations in the same location and the recorded acoustic pressure in the cabin are showed in Fig. 12-A.

With all the acceleration and force data transformed to the frequency domain and applying the inverse matrix method for each frequency, the acceleration-to-force matrix was calculated (Fig. 13-A). Furthermore, with a similar procedure than the previous one, the FRF matrix between forces and acoustic pressures has been obtained (shown in Fig. 14-A).

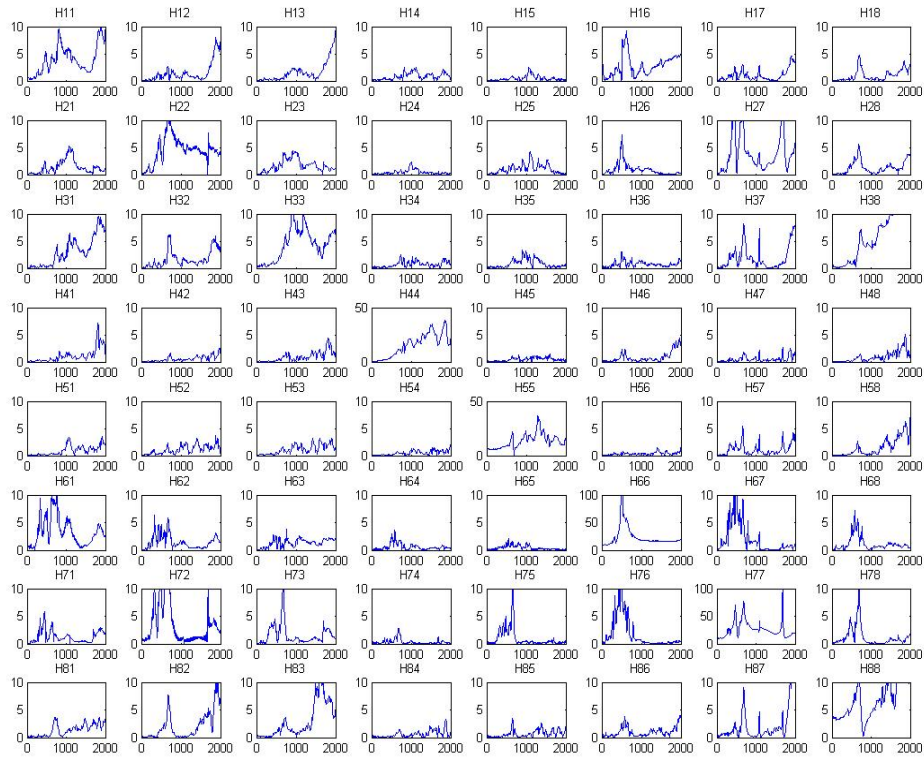


Fig.13-A. Acceleration-to-force frequency response functions

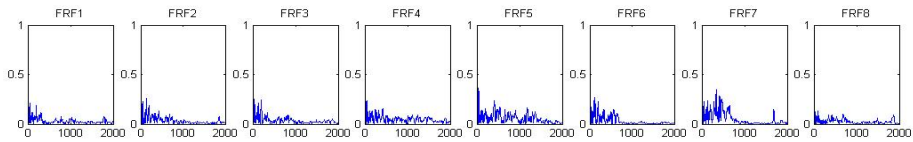


Fig.14-A. Force-to-acoustic frequency response functions

The main aim of the impact test is to calculate these two matrixes, which describe the system behaviour. The next step is to gather accelerations and acoustic pressure data of the operational test. With the accelerations in frequency domain and the acceleration-to-force matrix, the equivalent operational forces can be calculated (Fig. 15-A).

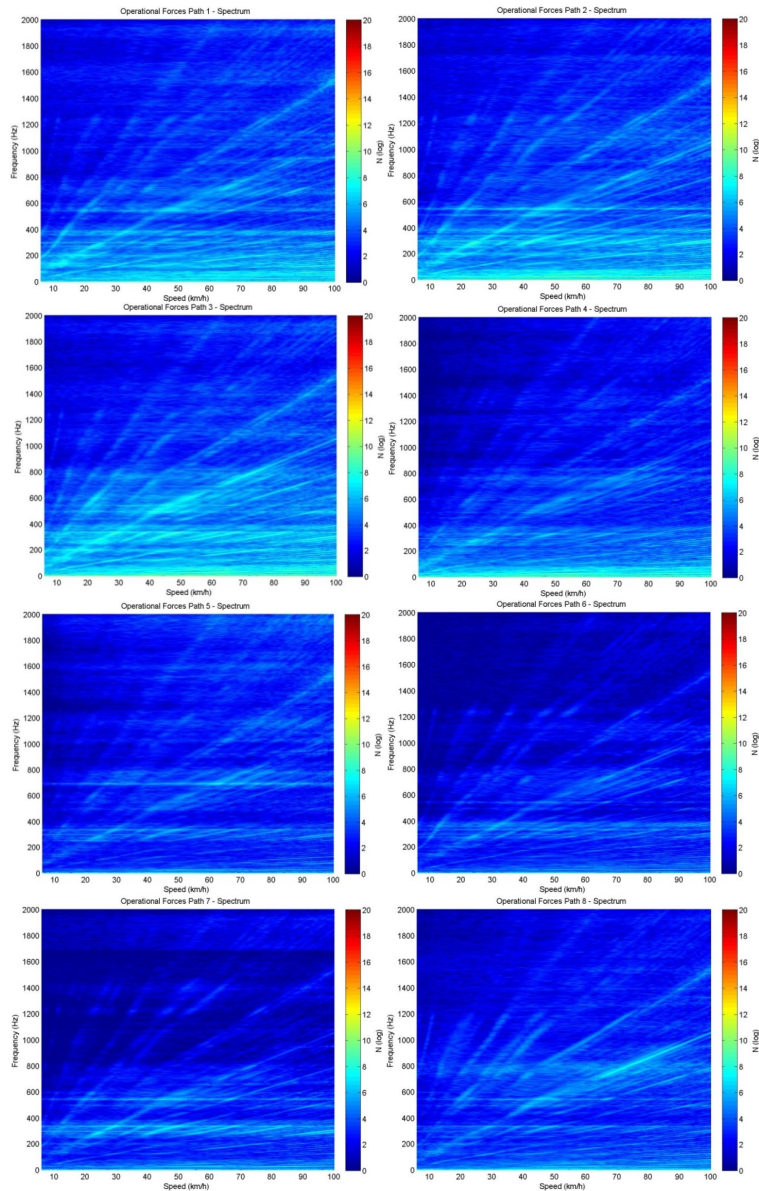


Fig. 15-A. Operational forces

Then, with the equivalent operational forces in each path and the FRF, the equivalent noise that is passing through each path can be calculated. These noise contributions are one of the set of results presented later. Adding all the individual noise contributions, the computed acoustic pressure in the cabin is obtained. To assess the

validity of this calculation, a comparison between with the measured one has been done and showed in Fig. 16-A.

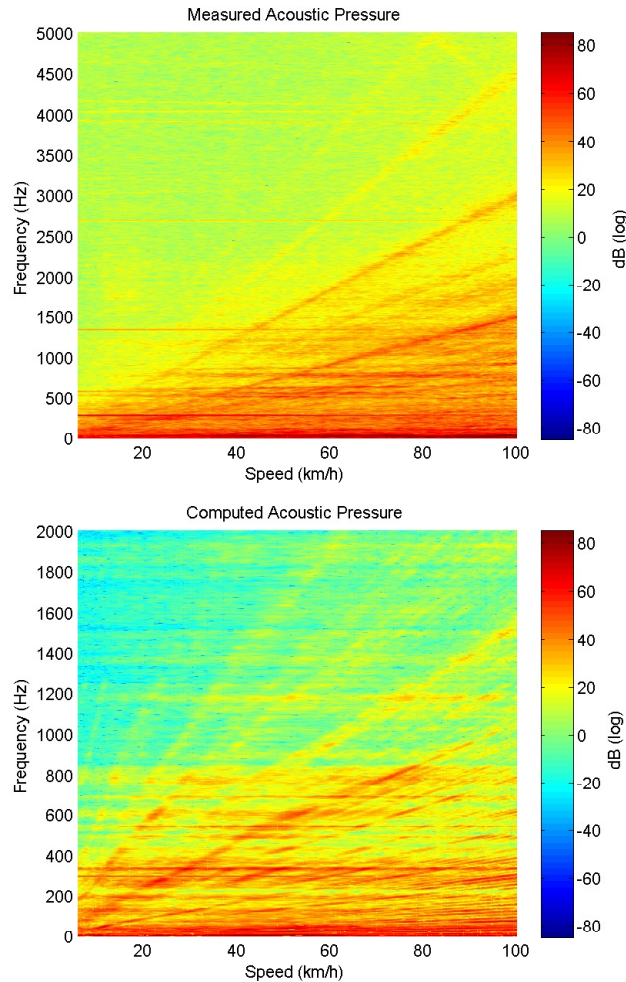


Fig. 16-A. Measured and computed acoustic pressure

The main conclusion that can be extracted from this fact is that the sources, which are producing the high frequency noise, are not taken into account. Thus, to obtain more reliable results, an increment in the number of paths has to be done.

Once the correlation between the measured and the computed acoustic pressure, two different set of results are presented. The first set of results is the equivalent acoustic pressure of each path in different speed and frequency conditions, see Fig. 17-A. Moreover, the second set of results, which present the acoustic pressure for each order of interest depending on the vehicle speed, see Fig. 18-A.

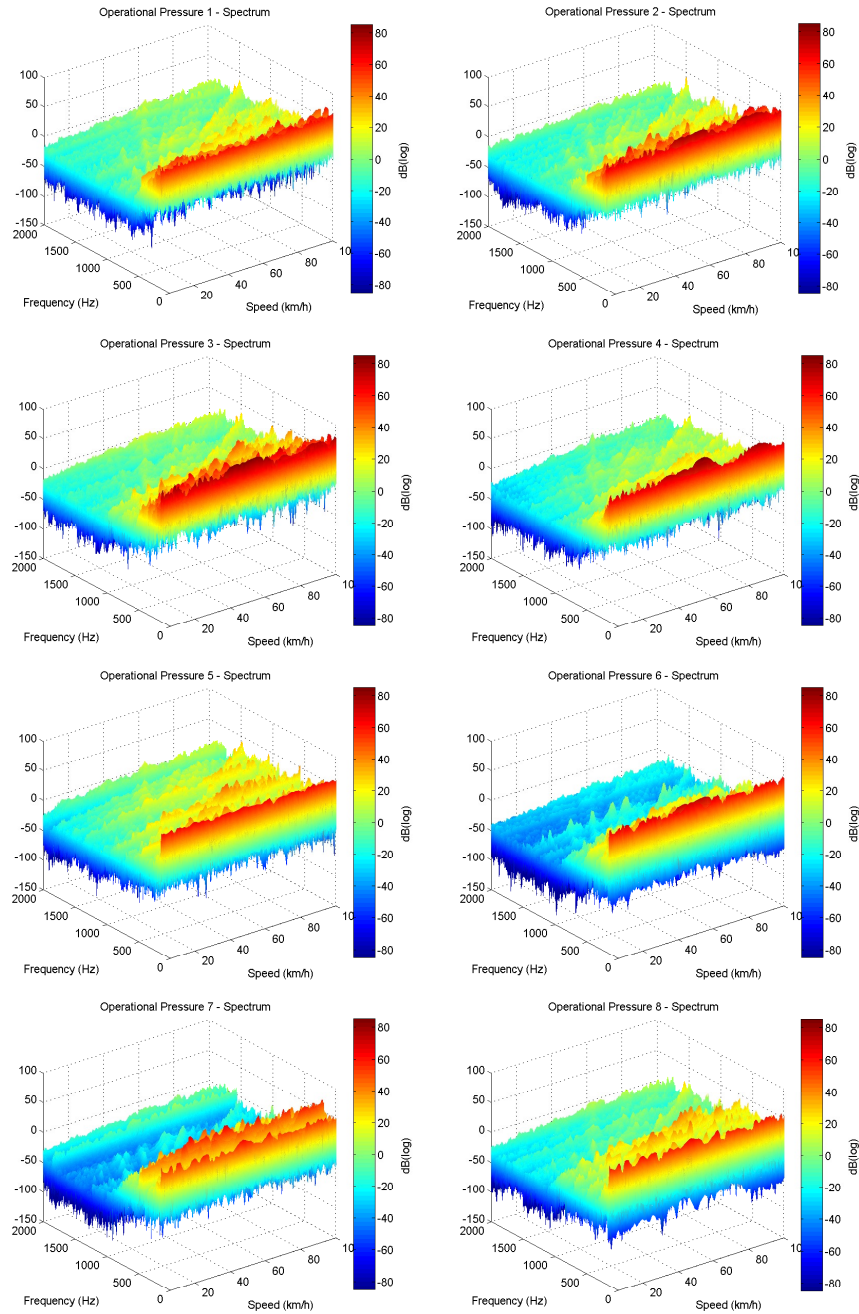


Fig. 17-A. Acoustic pressure of each transfer path in the frequency spectrum

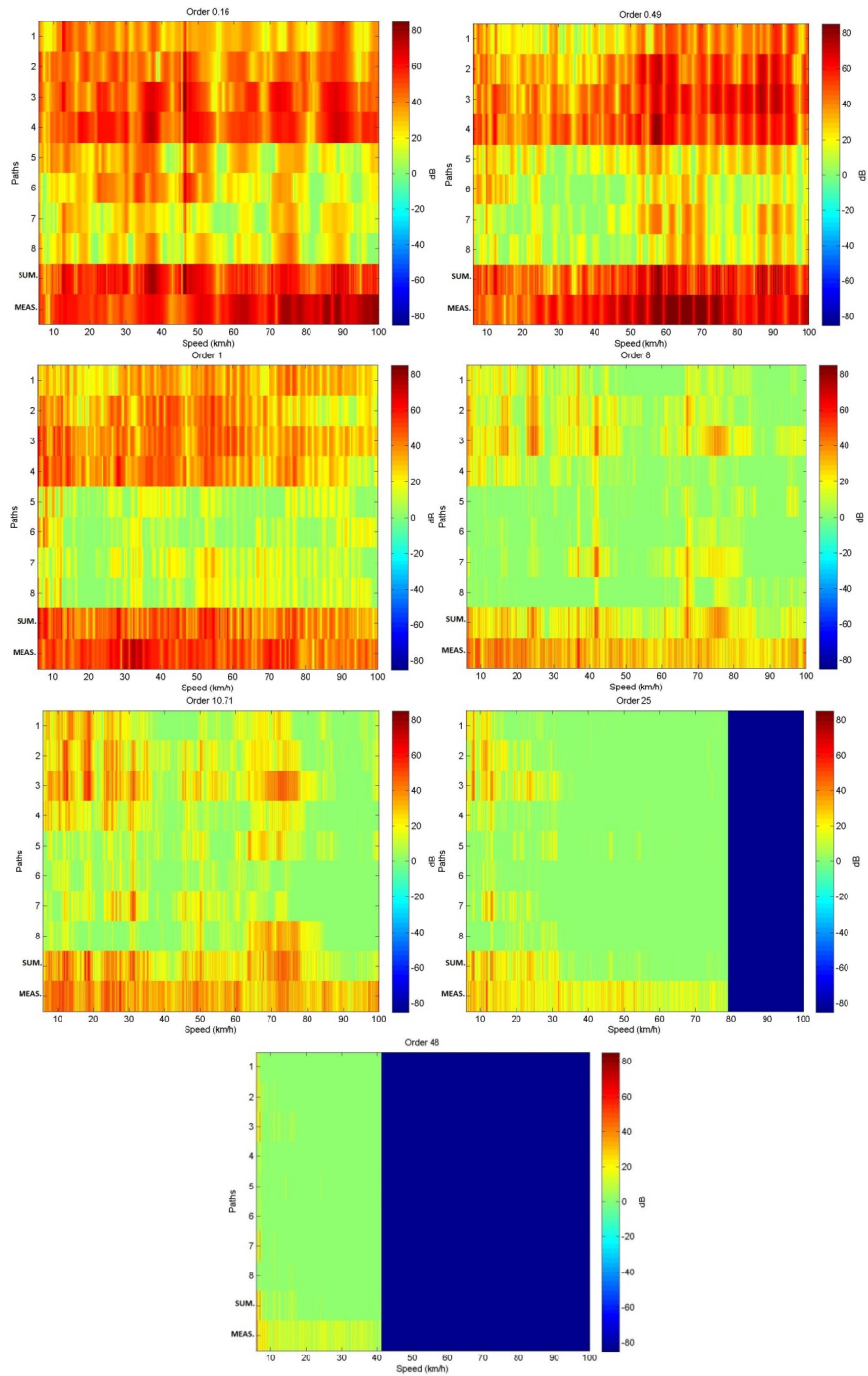


Fig. 18-A. Path analysis for the orders of interest

Comparison between methods

In this subsection, a comparison between the both methods explained is to be made. Firstly the main differences regarding the methodology and data needed to perform it are to be presented and lastly, the main differences among the results calculated by each method.

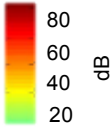
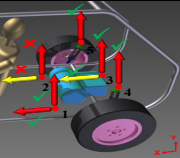
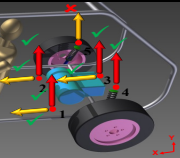
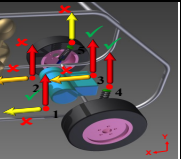
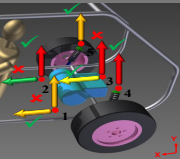
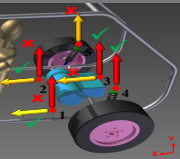
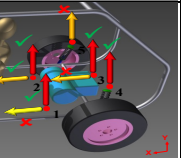
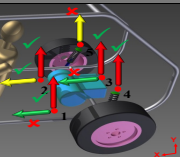
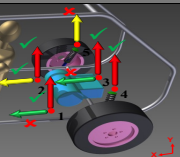
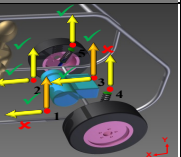
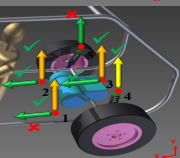
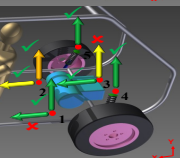
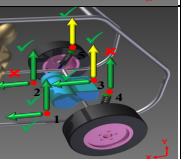
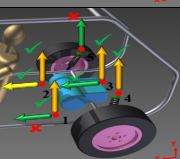
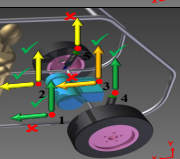
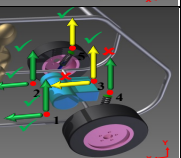
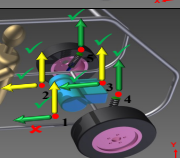
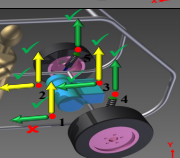
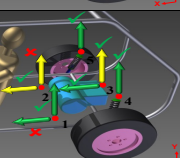
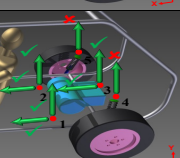
With regard to the methodology, several dissimilarities can be found. Whilst in the OPA only operational tests are necessary to execute the method, in the TPA both operational tests and static tests are compelled (in the case of study impact tests, although other kinds of test can be performed). With respect to this difference, as the transmissibility functions are obtained by the measured acoustic pressure, other operational tests are needed to check the validity of these functions in the OPA method. Nonetheless, in the TPA, as the system properties (FRFs) are calculated by static tests, only one operational test is required. Moreover, whilst the OPA mathematical method to obtain the transmissibility functions uses the measured acoustic pressure in operational conditions, the TPA does not use it to calculate properties of the system. In the TPA case, if all the paths are not considered, there will be a deviation between the measured and the computed acoustic pressure whilst in OPA method, an error in the transmissibility functions is introduced. The former error is noticeable and quantifiable, nevertheless, the latter is not easy to find and check. By comparing Fig. 9-A and Fig. 16-A, it can be seen the OPA acoustic pressure agrees better with the measured one than the TPA one. Nevertheless, this does not mean that OPA is better than TPA method.

From the assessment of the first set of results of both methods, a comparison between TPA and OPA acoustic pressure impact of each path has been made. In general terms, it can be appreciated that the spectrum shape and behaviour is the same in both methods, although the amplitude in the TPA results is higher than in the OPA ones

Regarding the second set of results, a comparison between TPA (right hand side) and OPA (left hand side) can be made by Table 5-A. Similarities between both methods can be found.

Although there are some dissimilarities quantitatively speaking, a good agreement can be deduced from Table 5-A.

Table 5-A. Comparison between methods

Noise Contributions  dB 80 60 40 20	LOW SPEED (< 30 km/h)	MEDIUM SPEED (30 – 80 km/h)	HIGH SPEED (> 80 km/h)
ORDER 0.16			
ORDER 0.49			
ORDER 1			
ORDER 8			
ORDER 10.71			
ORDER 25			X
ORDER 48			X

3A.7 Conclusions

The methodology can be applied to EV and HEV as demonstrated. One of the aims of this study is to check the versatility of these methods, commonly used in petrol engine cars, in electrical vehicles, which has been successfully fulfilled.

Technical goals

Two different sets of results have been presented; the noise contribution spectrum of each path and the path noise impact for some harmonics due to physical components of the electrical vehicle.

One of the conclusions extracted from this study is that TPA results are easier to realise when an error occurs than OPA ones. The error in the TPA is observed in the computed acoustic pressure that can be compared with the measured one having and instantaneous feedback. Nevertheless, the error of not considering paths in the OPA is computed to the transmissibility functions, and then transmitted to the computed acoustic pressure. Thus, although the last appearance of the acoustic pressure is really good, this does not mean that all the paths are considered.

The OPA results give a good approximation in a short period of time whilst to obtain the TPA results a longer and more arduous procedure has to be performed.

Another conclusion is inferred from the study, although the more number of accelerometers, the more accurate results, a good agreement with the real situation has been obtained with eight accelerometers.

3A.8 References

- [1] Ahlersmeyer, T. Transfer path analysis - a review of 18 years of practical application. Transfer Path Analysis - a Review of 18 Years of Practical Application, Rotterdam, 2009.
- [2] Siemens PLM Software. In Siemens PLM Software (Ed.), What is a transfer path analysis.
- [3] Schuhmacher, A., Tcherniak, D. Engine contribution analysis using a noise and vibration simulator. Sound and Vibration 43-1(2009) 16-21
- [4] Elliott, A. S., Moorhouse, A. T., Huntley, T., Tate, S. In-situ source path contribution analysis of structure borne road noise. Journal of Sound and Vibration 332-24(2013) 6276-6295
- [5] Bendat, J. S., Piersol, A. G. Engineering applications of correlation and spectral analysis J. Wiley, 1993
- [6] Verheij, J. Multipath sound transfer from resiliently mounted shipboard machinery. Technische Physische Dienst TNO-TH, Delft, 1986
- [7] Janssens, K., Gajdatsy, P., Van der Auweraer, H. Operational path analysis: A critical review. 23rd International Conference on Noise and Vibration Engineering 2008, ISMA 2008, 6, 3657-3671

- [8] Dobson, B. J., Rider, E. A review of the indirect calculation of excitation forces from measured structural response data. Proceedings of the Institution of Mechanical Engineers, Part C: Journal of Mechanical Engineering Science 204-2(1990) 69-75
- [9] Gajdatsy, P., Janssens, K., Desmet, W., Van Der Auweraer, H. Application of the transmissibility concept in transfer path analysis. Mechanical Systems and Signal Processing 24-7(2010) 1963-1976
- [10] Janssens, M. H. A., Verheij, J. W., Thompson, D. J. The use of an equivalent forces method for the experimental quantification of structural sound transmission in ships. Journal of Sound and Vibration 226-2(1999) 305-328
- [11] Thite, A. N., Thompson, D. J. The quantification of structure-borne transmission paths by inverse methods. part 1: Improved singular value rejection methods. Journal of Sound and Vibration 264-2(2003) 411-431
- [12] Fischer J., Behrendt M., Liesske D., Albers A. Measurement and analysis of the interior noise and the transfer path of acoustic phenomena into the driver cabin of a battery electric vehicle. Proceedings of InterNoise 2014, Melbourne, Australia, Paper 110, 2014.
- [13] De Sitter, G., Devriendt, C., Guillaume, P., Pruyt, E. Operational transfer path analysis. Mechanical Systems and Signal Processing 24-2(2010) 416-431
- [14] Janssens, K., Gajdatsy, P., Gielen, L., Mas, P., Britte, L., Desmet, W. OPAX: A new transfer path analysis method based on parametric load models. Mechanical Systems and Signal Processing, 25-4(2011) 1321-1338
- [15] Govindswamy K., T. Wellmann T., G. Eisele G. Aspects of NVH integration in hybrid vehicles. SAE Paper 2009-01-2085, 2009.
- [16] Meier C., Lieske D., Bikker S. NVH development of electric powertrains. SAE Paper 2014-01-2072, 2014.
- [17] Albers A., Fischer J., Landes D., Behrendt M. Method for measuring and analysing the transfer path of acoustic phenomena into the driver cabin of a battery electric vehicle. SAE Paper 2014-01-2071, 2014.
- [18] Genuit K. The future of NVH research – A challenge by new powertrains. SAE Paper 2010-36-0515, 2010.
- [19] Florentin J., Durieux F., Kuriyama Y., Yamaoto T. Electric motor noise in a lightweight steel vehicle. SAE Paper 2011-01-1724-1724, 2011.
- [20] Genuit K. Future acoustics of electric-vehicle. SAE Paper 2012-36-6012, 2012.

Annex 3B

Virtual sensing on mechatronic drivetrains using multiphysical models

Bart Forrier¹, Frank Naets¹ and Wim Desmet¹

¹Department of Mechanical Engineering, KU Leuven,
Celestijnenlaan 300B, 3001 Heverlee (Leuven), Belgium, bart.forrier@kuleuven.be,
frank.naets@kuleuven.be, wim.desmet@kuleuven.be,

Abstract. A numerical validation of coupled input/state estimation is performed on a mechatronic driveline consisting of an electric motor and a cardan transmission with flexible intermediate shaft. States and an a-priori unknown load torque are estimated using an unscented Kalman Filter. This approach enriches the nonlinear lumped-parameter electro-mechanic drivetrain model by measurement data. The measurement data – polluted with realistic noise levels - is generated by a reference model which consists of a 1D motor model in combination with a 3D flexible multibody model of the cardan transmission. By employing current measurements in combination with rotational acceleration data, stable load torque estimation is numerically validated for dynamic excitation. The technique can be applied to electric vehicles drivetrains in order to perform online assessment of wheel loading and driveline state.

3B.1 Introduction

In recent years, great advancements have been made with respect to mechanical system modelling. Research with respect to flexible multibody (FMB) system modelling has opened up the possibility to accurately calculate high-dynamic structural responses in terms of displacements and even strains and stresses for general mechanisms [1]. Thanks to recent advancements in the fields of model order reduction [2], such results can even be computed in real-time [3] for systems which can be described by a moderate number of relevant flexible deformation shapes. The integration of flexible multibody models in a multiphysical system model featuring coupling between electrical and mechanical dynamics also leads to insightful results. One example is insight in energy flows resulting from high-dynamic loading conditions in a weaving-machine [4]. Another example is insight in critical loading (i.e. torque reversals) of a wind-turbine's main shaft due to the coupling between mechanical and electrical dynamics [5].

Although such high-fidelity models perform a crucial role in the design of high-performance mechanical or multiphysical systems, their full potential is currently not exploited. The main limitation is that although mechanical and system-level behaviour are described in a lot of detail, still a high level of uncertainty exists on operational loading predictions. One important source of uncertainty is the fact that operational inputs are often not well-known, meaning that design engineers only have a vague idea about which inputs should be applied to the model. A second

contribution to uncertainty on computed results is formed by often quite big uncertainties on model parameter values. These are often not known a-priori or feature a complex (unmodeled) dependency on e.g. temperature or state of wear.

Recently, some attention has gone to combining high-fidelity models with state estimation techniques, which have a rich tradition in the field of navigation and control [6]. For these applications, low-cost estimation algorithms like the linear, extended and unscented Kalman Filter [16] (KF, EKF, UKF, see e.g. [7]) have been very successful [8]. Although most high-fidelity FMB models are not straightforward to implement in the recursive one-step predictor-corrector approach of the Kalman Filter, e.g. due to the presence of constraints [9], some recent examples of successful applications exist. Joint state/input estimation in civil engineering applications and based on a limited number of acceleration measurements is demonstrated in [10]. In [11], an EKF is employed to successfully apply combined state/input/parameter estimation on structural applications.

This work aims to make advancement towards combined input/state estimation on mechatronic drivetrains. Such drivetrains are found in e.g. wind turbines and electric vehicles (EV). These are subject to ever more stringent demands in terms of noise, vibration & harshness (NVH), energy-efficiency, and high-dynamic system behaviour. Although their performance has certainly increased over the last years (see e.g. [18]), a lot of problems still occur (see e.g. [12]) due to lack of detailed knowledge on operational system behaviour. This is due to a combination of aforementioned model uncertainties and the difficulty with which relevant dynamic quantities, like forces, torques or strain fields over a driveline can - or even cannot - be measured.

By combining feasible-to-obtain measurement data from different domains with a multiphysical drivetrain model, information on operational system behaviour is obtained. A lumped-parameter drivetrain model is used to simultaneously estimate the driveline state an external load torque (cfr. wheel loading), and indicates how a high-fidelity flexible multibody model will enlarge the scope and increase accuracy of estimation results.

When applying the presented approach to an EV, the resulting virtual torque measurement provides detailed insight in operational wheel forces transmitted to the drivetrain. As such, the principal cause of NVH problems related to drivetrain transmissions can be identified and quantified without the need for a torque sensor, even when nonlinear dynamics are involved.

This work is a reproduction of a paper [19], which was presented at the 2015 ECCOMAS Thematic Conference on Multibody Dynamics. The original paper puts somewhat more emphasis on the aspect of multibody modelling, whereas this book section is more oriented towards embedding 1D or 3D models in EV testing.

3B.2 Proposed Approach

This work uses two multiphysical models of varying complexity to numerically validate coupled state/input observer results on mechatronic drivetrains. Fig. 1-B illustrates this approach.

First, a reference model (a) of the mechatronic drivetrain is composed. The drivetrain consists of an asynchronous induction motor, connected to a load through a double cardan transmission in Z-configuration. The load consists of an inertia on which an external load torque acts. The reference model features both torsion and bending behaviour of the intermediate shaft in the double cardan transmission.

Next, a filter model (b) of the same drivetrain is derived. This model should be fit for use in the proposed state/ input observer, and allow for correct estimation of the a-priori unknown load torque. As discussed further on, the resulting filter model is highly nonlinear.

Finally, a Sigma Point Kalman Filter scheme [6] is implemented to allow fusing the nonlinear filter model with measurement data. The measurement data is generated from the reference model, after which realistic values for white noise are added. Comparison of the estimation results - specifically of the load torque - with the reference counterparts shows that the 1D model is suitable for observing torsional dynamics.

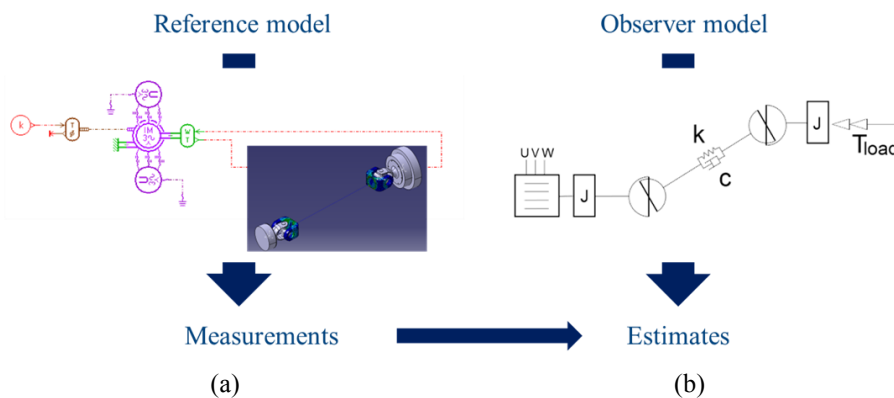


Fig. 1-B. Proposed approach to validate estimation results using a 1D-3D reference model

3B.3 Drivetrain model

Reference model

The reference model consists of a 1D induction motor model, combined with a 3D flexible multibody model of a double cardan configuration. LMS Imagine.Lab Amesim is used to solve both models in a co-simulation approach, employing LMS Virtual.Lab Motion to simulate the dynamic behaviour of the double cardan transmission. As the 3D flexible multibody model features system-level nonlinearity and distributed flexibility, it allows an informative assessment of the proposed estimation approach using a 1D observer model and enables to identify the added value of flexible multibody models in state estimation on mechatronic drivetrains.

The multibody model assumes the connections between yokes and cardan spiders to be ideal. The intermediate shaft is modelled as a flexible body, introducing both

torsional and bending oscillations in the driveline. Bending of the intermediate shaft changes the deflection angle of each cardan joint in a different way, so that the deflection angles are no longer identical. Torsion of the intermediate shaft means that both cardan joints no longer define one common plane, so that the in- and outgoing shaft no longer have the same speed, even in case of equal deflection angles.

Finally, the intermediate shaft has a periodical speed variation with respect to the in- or outgoing shaft at non-zero deflection angles. This also leads to torsional oscillations, as its inertia is greater than zero.

The induction motor model is a lumped-parameter description (see e.g. [13]). This model is readily available in Amesim's library of Electric Motors and Drives models. It represents exactly the same physical behaviour as the induction motor model used by the observer, presented later. As is common in literature, it also makes use of Park's transformation [14] to express both stator and rotor quantities in one common rotating reference frame. The frame consists of a direct (d) and quadrature (q) axis. The homopolar (0)-component is also computed, meaning applied stator voltages do not necessarily form a balanced set. Magnetic saturation and hysteresis effects are not modelled, hence both stator and rotor inductances are assumed constant in this qd0-frame.

To simulate the behaviour of the mechanical driveline in LMS Virtual.Lab Motion, a floating frame of reference component mode synthesis method (FFR-CMS) is used [1]. The intermediate shaft is modelled as a flexible body, and its corresponding set of component modes is computed using the Craig-Bampton method [15]. Its first five modes consist of the first and second lateral and vertical bending modes and the first torsion modes. These five modes dominate the high-dynamic response.

Fig. 2 shows the resulting flexible multibody model. Each end yoke of the intermediate shaft is connected to the corresponding joint's spider, modelled as a rigid body, by only allowing revolution along one axis of the spider. As the flange of each cardan joint is also modelled as a rigid body, it can easily be constrained to only rotate along the spider's other axis of rotation. Both the motor and load are assumed rigid as well. The motor is completely fixed to the adjacent flange, and is constrained to the ground so that it can only revolve around its own axis. The load rotates around its axis and is otherwise constrained to a rigid slider, which translates in one direction with respect to the ground. The translation distance, imposed through a kinematic driver, is constant throughout the simulation.

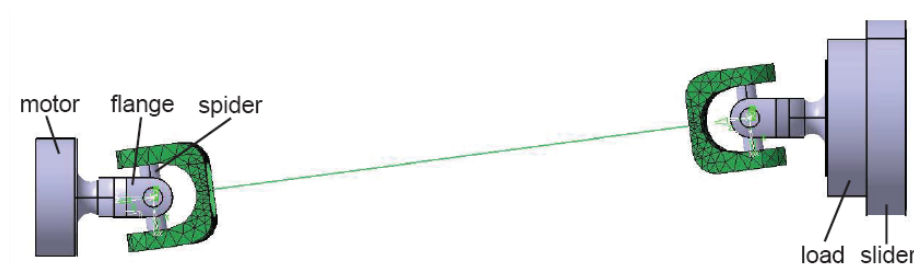


Fig. 2-B. Flexible multibody model of the mechanical part of the drivetrain

Observer model

The filter model is schematically shown in Fig. 1-Bb. Like the reference model, it includes electrical dynamics of the squirrel-cage induction machine as well as mechanical dynamics of the double-cardan transmission.

In the electrical part of this model, currents $i_{d,q}$ and voltages $u_{d,q}$ are decomposed along the direct and quadrature axis of a reference frame rotating in synchronism with the stator voltage phasor.

Additional subscripts $*_s$ and $*_r$ denote, respectively, stator and rotor quantities. The homopolar component is omitted, implying that the three phases of each electrical quantity, including externally applied stator voltages, form a balanced set. As in the reference model of the previous section, saturation and hysteresis effects are not included. Following these assumptions, Eq. 1-B describes the electromagnetic dynamics of the induction motor in continuous state space, with input matrix \mathbf{B}_{qdsr} and state update matrix \mathbf{A}_{qdsr} defined in Eq. 2-B. The electromagnetic motoring torque T_{em} is given in Eq. 3-B, where p denotes the pole pair number.

$$\frac{d}{dt} \begin{bmatrix} i_{qs} \\ i_{ds} \\ i_{qr} \\ i_{dr} \end{bmatrix} = \mathbf{A}_{qdsr} \begin{bmatrix} i_{qs} \\ i_{ds} \\ i_{qr} \\ i_{dr} \end{bmatrix} + \mathbf{B}_{qdsr} \begin{bmatrix} u_{qs} \\ u_{ds} \end{bmatrix} \quad \text{Eq. 1-B}$$

$$\mathbf{B}_{qdsr} \triangleq \sigma^{-1} \begin{bmatrix} L_r & 0 \\ 0 & L_r \\ -L_M & 0 \\ 0 & -L_M \end{bmatrix} \quad \text{Eq. 2-B}$$

$$\mathbf{A}_{qdsr} \triangleq \sigma^{-1} \begin{bmatrix} -r_s L_r & -\omega L_s L_r + L_M^2 (\omega - \omega_r) & r_r L_M & -\omega_r L_M L_r \\ \omega L_s L_r + L_M^2 (\omega - \omega_r) & -r_s L_r & \omega_r L_M L_r & r_r L_M \\ r_s L_M & -\omega_r L_M L_s & -r_r L_s & \omega L_M^2 - (\omega - \omega_r) L_r L_s \\ -\omega_r L_M L_s & r_s L_M & -\omega L_M^2 + (\omega - \omega_r) L_r L_s & -r_r L_s \end{bmatrix}$$

$$T_{em} = p L_M (i_{qs} i_{dr} - i_{ds} i_{qr}) \quad \text{Eq. 3-B}$$

In these equations, $\omega_r = p \omega_m$ (with ω_m the mechanical speed) is the electrical speed of the rotor and ω is the synchronous speed. Assuming the induction machine is coupled to an ideal grid, stator voltage amplitude and frequency are constant. This allows treating ω as a parameter. The leakage coefficient σ equals $L_s L_r - L_M^2$, with L_s and L_r respectively denoting the total stator and rotor inductance and L_M the mutual stator-rotor inductance. Stator and rotor resistance values are respectively denoted as r_s and r_r .

The mechanical part of the observer model features only torsional driveline dynamics induced by the cardan joint kinematics and by the torsional flexibility of the intermediate shaft. In contrast to the reference model, torsional oscillations do not arise as a result of speed variation of the – now massless - intermediate shaft in this model. Torsional oscillations occur as a result of flexibility of the intermediate shaft,

and its interaction with the cardan joint kinematics. Like in the reference model, the idealized cardan joints exhibit neither friction nor play.

The relation between the torque T_{is} in the intermediate shaft and the torque acting on the motor T_{cm} or load side T_{cl} by the cardan transmission is then given by Eq. 4-B. In this equation, $\omega_{is,m}$ ($\omega_{is,l}$) is the speed of the intermediate shaft at the motor (load) side, and ω_l is the speed of the load. The deflection angle of the cardan joint near the motor (load) is β_m (β_l). The torque transmitted by the intermediate shaft is given in Eq. 5-B, where $\vartheta_{is,m}$ and $\vartheta_{is,l}$ are the rotation angles at both ends of the Eq. 4 intermediate shaft. Eq. 6-B gives their relationship to the motor (load) angle ϑ_m (ϑ_l). As to Eq. 6-B indicate, the cardan joints induce nonlinear mechanical behaviour. This even holds at equal deflection angles β , as the intermediate shaft, although modeled as a linear spring-damper combination, behaves as if it featured a nonlinear spring characteristic.

$$\begin{aligned} T_{cm(cl)} &= T_{is} \left(\frac{\omega_{is,m(l)}}{\omega_{m(l)}} \right) \\ &= T_{is} \left(\cos \beta_{m(l)} (\cos \vartheta_{m(l)})^2 \right. \\ &\quad \left. + (\cos \beta_{m(l)})^{-1} (\sin \vartheta_{m(l)})^2 \right) \end{aligned} \quad \text{Eq. 4-B}$$

$$T_{is} = c(\omega_{is,m} - \omega_{is,l}) + k(\vartheta_{is,m} - \vartheta_{is,l}) \quad \text{Eq. 5-B}$$

$$\vartheta_{is,m(l)} = \tan^{-1}(\cos \beta_{m(l)} \tan \vartheta_{m(l)}) \quad \text{Eq. 6-B}$$

Using Eq. 3-B and Eq. 4-B, the dynamics of the mechanical part of the state vector are described by Eq. 7-B, where J_m and J_l respectively denote the inertia at the motor and load side, and T_{load} is the externally applied load torque.

$$\frac{d}{dt} \begin{bmatrix} \vartheta_m \\ \omega_m \\ \vartheta_l \\ \omega_l \end{bmatrix} = \begin{bmatrix} \omega_m \\ J_l^{-1}(T_{em} - T_{cm}) \\ \omega_l \\ J_l^{-1}T_{cl} \end{bmatrix} + \begin{bmatrix} 0 \\ 0 \\ 0 \\ -J_l^{-1} \end{bmatrix} T_{load} \quad \text{Eq. 7-B}$$

3B.4 Unscented Kalman Filter

Operational system behaviour and loading conditions can be obtained by combining measurement data with the model presented in the previous section. This combination is possible through the use of a state estimator. A great variety in such estimators exists, and a useful overview was provided by Radke and Gao [8]. In the context of virtual sensing using multiphysical models, the Kalman Filter [16] and its variants are appealing candidates, as their recursive two-step prediction-correction approach is relatively inexpensive in terms of computational cost.

The prediction essentially consists of integrating a discretized model with state vector \mathbf{x} from time t_{k-1} to time t_k . The correction is based on new measurement data \mathbf{y} at time t_k , and takes into account uncertainty on both the model \mathbf{f} and the measurements. This can be done by assuming zero-mean Gaussian white noise \mathbf{w}_k , with covariance matrix \mathbf{Q} , on the model equations 8 and similar noise \mathbf{n}_k with covariance matrix \mathbf{R} on the measurements Eq. 9-B.

$$\mathbf{x}_k = \mathbf{f}(\mathbf{x}_{k-1}, \mathbf{u}_{k-1}) + \mathbf{w}_k \quad \text{Eq. 8-B}$$

$$\mathbf{y}_k = \mathbf{h}(\mathbf{x}_k, \mathbf{u}_k) + \mathbf{n}_k \quad \text{Eq. 9-B}$$

In any Kalman filter approach, the prediction step provides a-priori estimates on the states and state covariances ($\hat{\mathbf{x}}_k^-$ and $\hat{\mathbf{P}}_{xx,k}^-$), as well as estimates of the expected measurements and their covariances ($\hat{\mathbf{y}}_k^-$ and $\hat{\mathbf{P}}_{yy,k}^-$). The correction step is based on the difference between expected and actually retrieved measurements, using the estimated covariances to perform an optimal weighting between model and measurement info.

In the Unscented Kalman Filter (UKF), a-priori ($*^-$) state and covariance estimates at time k are generated by passing states at time $k-1$ through the nonlinear state update function \mathbf{f} using an Unscented Transformation (UT) [17]. The UT consists of determining a set of $2n+1$ sigma points χ around the current estimate $\hat{\mathbf{x}}$ (n is the dimension of \mathbf{x}), and transforming each sigma point through the nonlinear function (Eq. 10-B and 11-B). Applying predetermined weights W_i to each transformed sigma point χ_i^* , $i = 1..2n+1$ results in an a-priori estimate of the state vector's mean value and covariance matrix (Eq.12-B and 13-B). The same UT approach yields measurement predictions (Eq. 14-B to 16-B), as well as the cross covariance $\hat{\mathbf{P}}_{xy,k}$ between states and measurements (Eq. 17-B). When model and measurement errors \mathbf{w} and \mathbf{n} are indeed Gaussian, correctly chosen weights W_i yield exact mean and covariance estimates even though only $2n+1$ samples are used to nonlinearly transform the uncertainty distributions. In the presented work all W_i are equal to $1/(2n)$, except $W_1 = 0$.

$$\chi = \left[\hat{\mathbf{x}}_{k-1} \quad \hat{\mathbf{x}}_{k-1} + \sqrt{\hat{\mathbf{P}}_{xx,k-1}^-} \quad \hat{\mathbf{x}}_{k-1} - \sqrt{\hat{\mathbf{P}}_{xx,k-1}^-} \right] \quad \text{Eq. 10-B}$$

$$\chi_i^* = \mathbf{f}(\chi_i, \mathbf{u}_{k-1}) \quad \text{Eq. 11-B}$$

$$\hat{\mathbf{x}}_k^- = \sum_{i=1}^{2n+1} W_i \chi_i^* \quad \text{Eq. 12-B}$$

$$\hat{\mathbf{P}}_{xx,k}^- = \mathbf{Q} + \sum_{i=1}^{2n+1} W_i (\chi_i^* - \hat{\mathbf{x}}_k^-) (\chi_i^* - \hat{\mathbf{x}}_k^-)^T \quad \text{Eq. 13-B}$$

$$Y_i^* = \mathbf{h}(\chi_i, \mathbf{u}_{k-1}) \quad \text{Eq. 14-B}$$

$$\hat{\mathbf{y}}_k^- = \sum_{i=1}^{2n+1} W_i Y_i^* \quad \text{Eq. 15-B}$$

$$\hat{\mathbf{P}}_{yy,k}^- = \mathbf{R} + \sum_{i=1}^{2n+1} W_i (Y_i^* - \hat{\mathbf{y}}_k^-)(Y_i^* - \hat{\mathbf{y}}_k^-)^T \quad \text{Eq. 16-B}$$

$$\hat{\mathbf{P}}_{xy,k}^- = \sum_{i=1}^{2n+1} W_i (\chi_i^* - \hat{\mathbf{x}}_k^-)(Y_i^* - \hat{\mathbf{y}}_k^-)^T \quad \text{Eq. 17-B}$$

The correction step yields the a-posteriori ($*^+$) estimates of state and covariances, through the Kalman gain matrix \mathbf{K} defined in Eq. 18-B and measurement update equations 19 and 20.

$$\mathbf{K} = \hat{\mathbf{P}}_{xy,k}^- (\hat{\mathbf{P}}_{yy,k}^-)^{-1} \quad \text{Eq. 18-B}$$

$$\hat{\mathbf{x}}_k^+ = \hat{\mathbf{x}}_k^- + \mathbf{K}(\mathbf{y}_k - \hat{\mathbf{y}}_k^-) \quad \text{Eq. 19-B}$$

$$\hat{\mathbf{P}}_{xx,k}^+ = \hat{\mathbf{P}}_{xx,k}^- - \mathbf{K} \hat{\mathbf{P}}_{yy,k}^- \mathbf{K}^T \quad \text{Eq. 20-B}$$

In this work, as in a lot of industrial cases, knowledge on the system's states implicitly assumes knowledge on the input, i.e. T_{load} (see fig. 1-Bb). The resulting problem of coupled state/input estimation can be solved by augmenting the state vector with unknown input u_u , leaving only known inputs in \mathbf{u} . By lack of other knowledge, the unknown input is typically assumed to follow a random-walk, i.e. to be nominally constant ($u_k^- = u_{k-1}^+$), yet variable due to associated process noise w_u .

The resulting Augmented Unscented Kalman Filter (A-UKF) predicts the augmented state vector (defined in eq. 21-B) based on a discretized version of Eq. 1-B, 7-B and 22-B. The discretization makes use of an explicit second-order Runge-Kutta scheme with a timestep of 500 μs .

$$\mathbf{x}^T \triangleq [i_{qs} \quad i_{ds} \quad i_{qr} \quad i_{dr} \quad \vartheta_m \quad \omega_m \quad \vartheta_l \quad \omega_l \quad T_{load}]^T \quad \text{Eq. 21-B}$$

$$\frac{dT_{load}}{dt} = 0 \quad \text{Eq. 22-B}$$

Electrical measurements consist of the stator currents in the dq-frame, after the transformation of the currents through inverter terminals a,b,c using Eq. 23-B. In this equation ϑ_d denotes the instantaneous electrical angle of the d-axis w.r.t. the axis defined by motor coil a. The same transformation is also useful for determining the known input $\mathbf{u}^T \triangleq [u_{qs} \quad u_{ds}]$.

$$\begin{bmatrix} i_{qs} \\ i_{ds} \end{bmatrix} = \sqrt{2/3} \begin{bmatrix} \cos(\vartheta_d) & \cos\left(\vartheta_d - \frac{2\pi}{3}\right) & \cos\left(\vartheta_d + \frac{2\pi}{3}\right) \\ \sin(\vartheta_d) & \sin\left(\vartheta_d - \frac{2\pi}{3}\right) & \sin\left(\vartheta_d + \frac{2\pi}{3}\right) \end{bmatrix} \begin{bmatrix} i_a \\ i_b \\ i_c \end{bmatrix} \quad \text{Eq. 23-B}$$

Mechanical measurements include shaft angle ϑ_m and speed ω_m obtained through a 1024-p encoder at the motor side, and shaft accelerations $\dot{\omega}_m$ and $\dot{\omega}_l$ at either side of the driveline. The latter can practically be obtained by a Ferraris-sensor. The

measurement functions of Eq. 24-B feature no direct feedthrough of known inputs \mathbf{u} . This holds for the mechatronic system of fig. 1-Bb, as well as for many other applications. Note that the accelerations in \mathbf{h} depend highly nonlinearly on the states \mathbf{x} .

$$\mathbf{h}(\mathbf{x}) = [i_{qs} \quad i_{ds} \quad \vartheta_m \quad \omega_l \quad J_m^{-1}(T_{em} - T_{cm}) \quad J_l^{-1}(T_{cl} - T_{load})]^T \quad \text{Eq. 24-B}$$

Covariance matrices \mathbf{Q} and \mathbf{R} are assumed diagonal. \mathbf{Q} is chosen such that a deviation of 10 % on the model parameters does not influence the estimation results significantly, whilst \mathbf{R} is based on datasheets of existing sensors. Specific attention is given to the element of \mathbf{Q} corresponding to T_{load} . This parameter is tuned so that fast variations on T_{load} are properly tracked, whilst not unnecessarily increasing overall noise on the estimation results.

3B.5 Discussion of results

To validate the estimation, first a simulation is performed on the reference model. This simulation has a duration of 10-seconds and consists roughly of two parts. From the start up to 2.5 seconds into the simulation, the load torque equals the motor's nominal value, and the terminal voltages form a balanced set at nominal amplitude and frequency. This corresponds to a direct online start of the motor. After about 2.5 seconds, nominal speed is reached. During the following part, a linear sine sweep from 10 Hz to 200 Hz is superposed onto the nominal load torque (fig. 3-Ba). The amplitude starts at 10 % of the nominal torque value, and drops linearly at a rate of 0.0395 % per Hz, reaching 2.5 % at the end of the simulation (fig. 3-Bb).

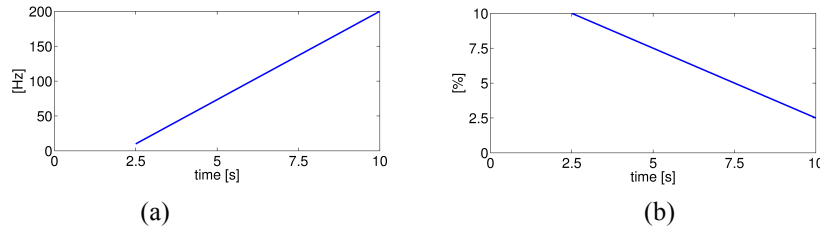


Fig. 3-B. Sinusoidal load torque's (a) frequency and (b) amplitude as a percentage of the constant (nominal) load torque

Using the filter model of before and noised measurements from the reference simulation, the A-UKF of section 4 is able to jointly estimate the states and a-priori unknown dynamic load torque. Accuracy of the estimates obviously depends on the noise level for the measurements, but also on how well the filter model matches the simulated behaviour of the reference model.

Fig. 4-Ba shows the estimate of the motor speed ω_m versus the measurement values. Fig. 4-Bb shows the same estimate versus the actual motor speed of the reference model. Comparison of both Fig.s reveals that the speed estimate ω_m is much more accurate than its measured counterpart. This requires a reasonably good observer

model, combined with accurate measurements of other quantities. In this case, the acceleration measurements are very accurate (fig. 4-Bc), with a signal-to-noise-ratio (SNR) of 84 dB. The dynamic load torque estimation (fig. 4-Bd) also benefits greatly from these accurate measurements. The electrical current measurements (which have a rather low SNR of 20 dB) are required for stability of this (joint state/input) estimator.

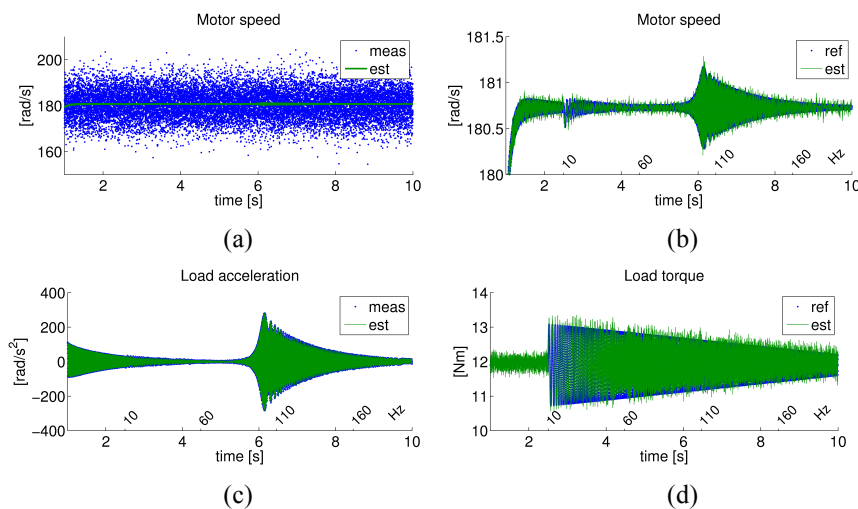


Fig. 4-B. Estimates (green lines) compared to measured or reference signal (blue dots) for (a,b) motor speed, (c) load acceleration and (d) load torque

Fig. 5-Ba-5-Bi zoom in on the results from Fig. 4-Bb-4-Bd, revealing good overall correspondence between measured and estimated values at excitation frequencies up to approximately 160 Hz. It can be noted that the model-based estimation allows to identify the load torque quite well below the first driveline resonance (Fig. 5-Ba-5-Bc), around this resonance (Fig. 5-Bd-5-Bf) and above this resonance (Fig. 5-Bg-5-Bi). The latter case is particularly challenging, as the load torque changes quite rapidly between successive time steps, while measurements are still dominated by the effect of passing by the first torsional resonance.

In order to gain further insight in the quality of estimation results, waterfall diagrams of load acceleration and load torque estimation results are shown in Fig. 6a and 6b, respectively. These reveal that on the whole, the rather complex and nonlinear relationship between applied inputs (i.e. load torque) and measurements (i.e. load acceleration) are well-captured by the filter model. Indeed, the load acceleration shows significant frequency content between 150 Hz to 160 Hz, which can be attributed to nonlinear behavior of the cardan transmission, and around the first torsional resonance just below 100 Hz. Both effects due to system behavior are, as expected, not visible in the load torque estimate. The load acceleration between 60 and 70 Hz, though, is reflected in the load torque estimate, which should ideally not be the case. The reason is that the filter model assumes the intermediate shaft to be massless, which is not the case in the reference model. Therefore the filter correlates

the resulting component on second shaft order in measured load acceleration to an erroneous component in the estimated load torque.

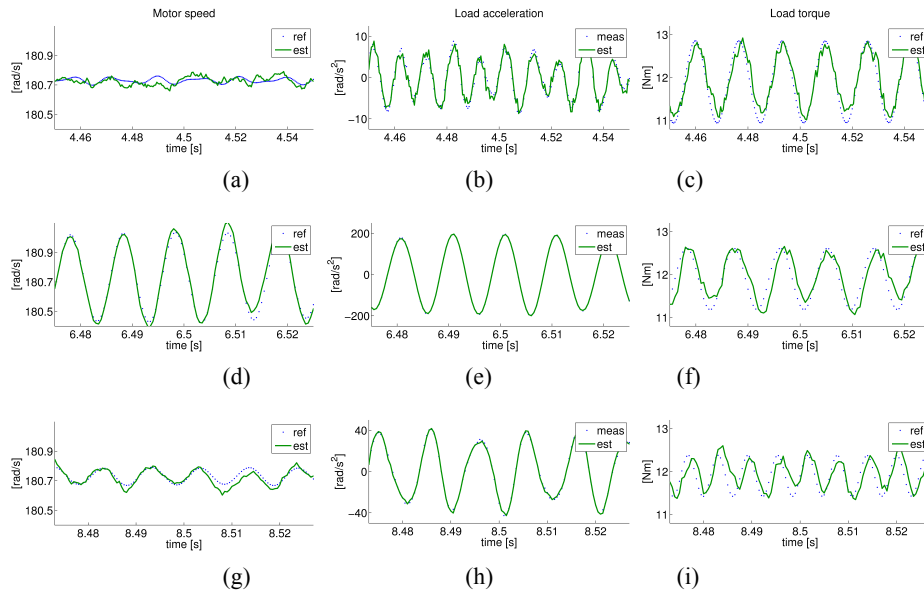


Fig. 5-B. Motor speed (left), load acceleration (middle) and load torque (right) estimate (green line) compared to reference or measurement signal (blue dots). The graphs zoom in on a region where the load torque passes a frequency of 60 Hz (a,b,c), 110 Hz (d,e,f) and 160 Hz (g,h,f)

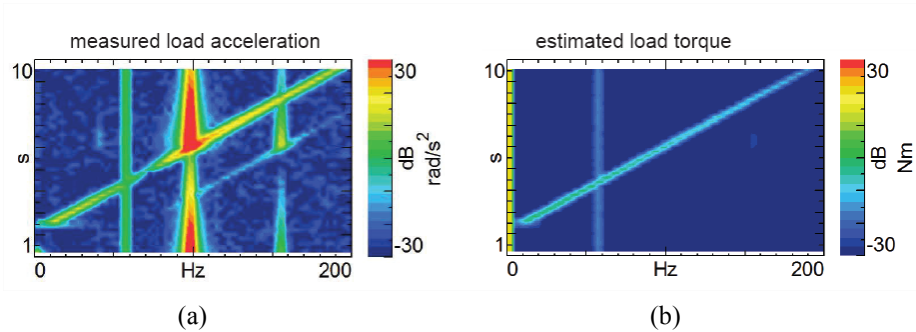


Fig. 6-B. Waterfall diagrams of (a) load acceleration measurement and (b) load torque estimate

This model mismatch could be remedied by adding a state-dependent equivalent inertia to both the motor and the load side, representing the effect of the intermediate shaft's rotational inertia. However, matching the driveline's rigid behavior around the second shaft order would result in both inertia values equalling half of the actual shaft's inertia, whereas matching the behaviour around the first torsional resonance would require much lower equivalent inertia values. A model mismatch like this one is consequently difficult to remedy using a lumped-parameter description, whereas making the step towards a flexible multibody description in the filter model would completely avoid the problem, and allow to describe combined torsional and bending

behaviour. Therefore, future research will focus on embedding a FMB model in state estimation, using the Global Modal Parametrization scheme [3] to reduce the number of states and eliminate constraint equations. The test setup of Fig. 7-B will then be used for validation. This setup is a general representation of an EV driveline. The induction machine on the right simulates the wheel load acting on the driveline and this input is transmitted to the motor on the left in a nonlinear fashion.

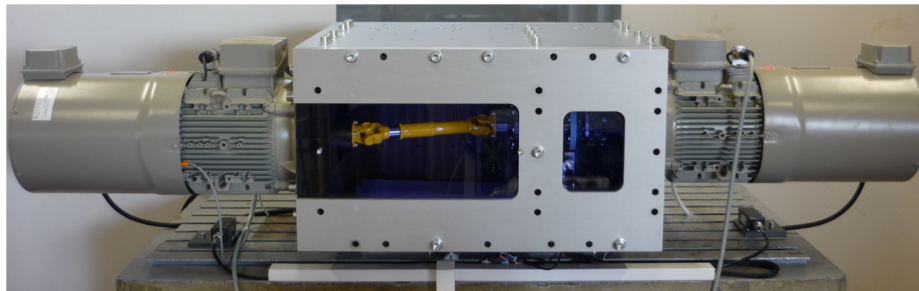


Fig. 7-B. Test setup for validation of estimation techniques in future research

3B.6 Conclusions

Combined input/state estimation on a mechatronic drivetrain has been presented. The state and load torque estimation approach makes use of unscented Kalman Filtering, combining a lumped-parameter non-linear electro-mechanical drivetrain model with measurements of electrical voltages and currents, encoder data and rotational acceleration. It is validated against a combined 1D-3D numerical model. In spite of significant deviations between reference and filter model, the obtained estimation accuracy allows virtual sensing of dynamic torque input covering a bandwidth of 0 to approximately 160 Hz, significantly higher than the driveline's first resonance frequency. Finally, this work points out how moving from a lumped-parameter drivetrain model towards a 1D-3D model would improve the accuracy and enlarge the scope of the applied estimation techniques. Future work will encompass validation on a test setup representing a general EV driveline subject to wheel loading. As such, the technique can be used to identify and quantify NVH problems related to drivetrain oscillations as a result of interaction between operational wheel forces and possibly nonlinear drivetrain dynamics.

3B.7 References

- [1] T. M. Wasfy, A. K. Noor. Computational strategies for flexible multibody systems. *Applied Mechanics Reviews* 56-6(2003) 553-613.
- [2] B. Besselink, U. Tabak, A. Lutowska, N. van de Wouw, H. Nijmeijer, D.J. Rixen, M.E. Hochstenback, W.H.H. Schilders. A comparison of model reduction techniques from structural dynamics, numerical mathematics and systems and control. *Journal of Sound and Vibration* 332-13(2013) 4403-4422.

- [3] F. Naets, T. Tamarozzi, G. H. K. Heirman, W. Desmet. Real-time flexible multibody simulation with Global Modal Parameterization. *Multibody System Dynamics* 27-3(2012) 267-284.
- [4] J. Croes, A. Reveillere, S. Iqbal. A combined 1D-3D simulation approach for the energy analysis of a high speed weaving machine. In *Proceedings International Conference on Noise and Vibration Engineering*, 2253-2268, Leuven, 2012.
- [5] B. Blockmans, J. Helsen, F. Vanhollebeke, W. Desmet. Dynamic response of a multimegawatt wind turbine drivetrain under voltage dips using a coupled flexible multibody approach. In *ASME 2013 Power Transmission and Gearing Conference*, art. nr. DETC2013-12458, Portland, Oregon, 2013.
- [6] R. van der Merwe, E. A. Wan, S. J. Julier. Sigma-point Kalman filters for nonlinear estimation and sensor-fusion - applications to integrated navigation. In *Proceedings AIAA Guidance, Navigation, and Control Conference*, pp. 16-19, Providence, Rhode Island, 2004.
- [7] D. Simon. *Optimal State Estimation*. JohnWiley & Sons, Inc. Hoboken, New Jersey, 2006.
- [8] A. Radke, Z. Gao. A survey of state and disturbance observers for practitioners. In *Proceedings of the 2006 American Control Conference*, 5183-5188, Minneapolis, Minnesota, 2006.
- [9] D. Simon. Kalman filtering with state constraints: a survey of linear and nonlinear algorithms. *IET Control Theory & Applications*, Vol. 4, No. 8, pp. 1303-1318, 2010.
- [10] E. Lourens, C. Papadimitriou, S. Gillijns, E. Reynders, G. De Roeck, G. Lombaert. Joint input-response estimation for structural systems based on reduced-order models and vibration data from a limited number of sensors. *Mechanical Systems and Signal Processing* 29(2012) 310-327.
- [11] F. Naets, J. Croes, W. Desmet. An online coupled state/input/parameter estimation approach for structural dynamics. *Computer Methods in Applied Mechanics and Engineering* 283(2015) 1167-1188.
- [12] J.M. Pinar Perez, F.P. Garcia Marquez, A. Tobias, M. Papaalias. Wind turbine reliability analysis. *Renewable and Sustainable Energy Reviews* 23(2013) 463-472.
- [13] P.C. Krause, O. Wasynczuk, S. D. Sudhoff. *Analysis of Electric Machinery and Drive Systems* (2nd ed.). John Wiley & Sons, Inc., New York, 2002.
- [14] R.H. Park. Two-reaction theory of synchronous machines. *Transactions of the American Institute of Electrical Engineers* 45-3(1929) 716-727.
- [15] M.C.C. Bampton and R.R. Craig, Jr.. Coupling of substructures for dynamic analyses. *AIAA Journal*, 6-7(1968) 1313-1319.
- [16] R.E. Kalman. A new approach to linear filtering and prediction problems. *Journal of Fluids Engineering* 82-1() 35-45.
- [17] S. J. Julier, J. K. Uhlmann. Unscented filtering and nonlinear estimation. *Proceedings of the IEEE*, 92-3(2004) 401-422.
- [18] N. Amann, J. Böcker, F. Prenner. Active damping of drive train oscillations for an electrically driven vehicle. *IEEE/ASME Transactions on Mechatronics* 9-4(2004) 697-700.
- [19] B. Forrier, F. Naets, W. Desmet. Virtual sensing on mechatronic drivetrains using multiphysical models. In *Proceedings of the ECCOMAS Thematic Conference on Multibody Dynamics*, 708-719, Barcelona, Catalonia, Spain, 2015.

Annex 3C

Numerical-experimental vibro-acoustic characterisation of lightweight materials using a novel test setup

Stijn Jonckheere¹, Elke Deckers¹, Daniele Brandolisio¹, Claus Claeys¹,
Bert Pluymers¹, Wim Desmet¹

KU Leuven, Department Mechanical Engineering, Celestijnenlaan 300 box 2420, B-3001, Heverlee, Belgium, stijn.jonckheere@kuleuven.be,

Abstract. This chapter reviews an experimental-numerical approach to study the NVH (Noise, Vibration and Harshness) behaviour of acoustic damping materials and lightweight structures using a novel test setup which allows for a fast and accurate characterisation of these materials, in synergy with a numerical simulation tools for vibro-acoustics. The combination of accurate simulations and the versatility of the aforementioned test setup show great potential for material characterisation, of acoustic damping materials (internal configuration) and lightweight structures (transmission configuration).

3C.1 Introduction

Driven by the increased commodity prices, the direct material cost and fuel consumption have become key design features of many products. In numerous industries, product manufacturers are driven towards lightweight materials. A prime example is the automotive sector, where lightweight materials can compensate for the additional weight of electrical vehicles, which require heavy batteries, but can also improve the handling of the vehicle and its energy efficiency. A lower weight with retained stiffness however has an adverse effect on the noise and vibration insulation properties. This opposes the present day trends in product design, where noise and vibration levels are not only imposed by the legislator, with increasingly strict regulations, but have also become a fundamental commercial differentiator.

To overcome these deteriorated NVH properties, damping material is often added ad hoc in the last design stage. However, such non-optimised measures strongly decrease the expected final weight gain and can even undo it. Therefore, the effect of lightweight materials on the product's NVH behaviour has to be estimated as early as possible in the product design cycle, in order to allow an optimised design. This means that the NVH properties of these structures have to be accounted for in the design and development phase, both experimentally and numerically. New material developments and the increasing complexity of final products often require new experimental practises and new numerical methods to study the dynamic properties of this new generation of lightweight components.

According to the standards, acoustic noise transmissibility of lightweight structures is evaluated in terms of Transmission Loss (TL) [3]. This technique provides a very good and generally valid characterisation of the test specimen, but it involves a

cumbersome and time consuming procedure. Moreover transmission facilities have a very large investment cost. For the assessment of acoustic absorption of materials, on the other hand, Kundt's tube measurements are often used. Although these experiments are easy and cheap to perform, they are based on normal incidence of the acoustic waves, thus giving a poor characterisation for oblique incidence. Faster, more accurate and more practical tools, models and theories are necessary to support faster material characterisation and a more intelligent development process. Therefore a new test setup [4, 5, 6] was proposed, consisting of a small (0.83 m³), mobile (3 ton, supported on a three wheel system) and inexpensive single acoustic cavity. Test specimens of different sizes, and thicknesses can be tested over a wide frequency range (50-20000 Hz).

The state of the use numerical schemes for vibro-acoustic simulations in the low- and mid-frequency region are mostly deterministic element based approaches, such as the Finite Element Method (FEM) [7] and the Boundary Element Method (BEM) [8]. These methods discretise the problem domain or its boundary into a large number of small elements in which polynomial shape functions interpolate the nodal values of the field variables but are limited in their applicable frequency as the number of elements needs to be refined more than linearly to properly capture the dynamic behaviour. This results in a practical upper frequency limit above which these techniques are no longer useable. The inclusion of lightweight materials and complex damping materials even further restricts this applicable frequency range. The so-called mid-frequency region, which is very relevant to the modelling of lightweight structures, stays out of reach of these simulation tools. To overcome this, an alternative method, the Wave Based Method (WBM) [9, 10] is being developed. Through its Trefftz-approach [11], which builds in *a priori* knowledge on the physics at hand, it exhibits a high computational efficiency, thus efficiently increasing the upper frequency limit for simulations.

The presented paper is divided in five sections. After the introduction section 2 gives a general description of the test setup that was designed and built at KU Leuven. Thereafter, the general modelling principles of the element-based approaches, the WBM and its hybrid extensions are discussed. The fourth section discusses the experimental and numerical approach to tackle both an internal configuration for the acoustic characterisation of damping layers as well as an external configuration for the vibro-acoustic characterisation of lightweight panels. The paper is concluded with a summary of results and future research perspectives.

3C.2 Test setup

Specifications

At KU Leuven a new test setup, depicted in Fig. 1-C, was developed. It consists of an acoustic cavity with a dismountable front wall to which a flexible component can be mounted.

The cavity is very compact (0.83 m³, 3 ton) and has a dominant modal behaviour in the frequency range up to 3 kHz. Five of the six cavity walls consist of reinforced

concrete (thickness 0.150 m to 0.200 m), while the front wall is a 0.035 m thick aluminium plate. Both can as such be considered acoustically and structurally rigid in the considered frequency range. The inner volume is designed so that it has a good modal distribution in the lower frequency zone, thus effectively avoiding coincident acoustic resonances [12], while still preserving a convex shape. This requirement led to inner walls where none is parallel to any of the other. Different configurations of the front wall exist with differently sized testing windows. Currently, a number of standardised front frames are available: a fully closed one and a set of front walls with DIN A-sized test openings to host samples.

Airborne excitation by means of a full-range speaker inside the cavity, as well as electro-dynamic shaker or an impact hammer as structure-borne excitation can be directly applied to the test sample. Correspondingly, both the acoustic and structural system response can be measured. For this, the cavity is equipped with a network of microphones and the structural dynamic response can be recorded using lightweight accelerometers or a laser vibrometer. The radiated acoustic power can be measured by scanning the radiating surface with an intensity probe or a pu-probe.

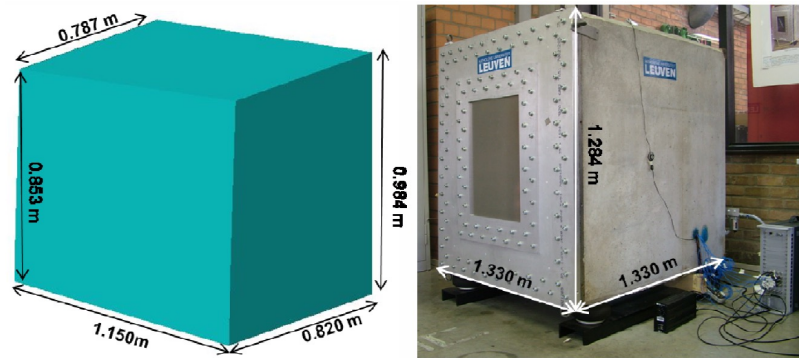


Fig. 1-C. Inner (left) and outer (right) dimensions

Comparison to Transmission suite

As mentioned earlier in the introduction section, the standard procedure for the assessment of the NVH properties of materials is the use of a transmission suite. This is carried out on dedicated facilities, which are very expensive and require considerable effort. The international standards [13, 14] give a detailed description of a transmission suite. It consists of two adjacent rooms, a reverberant source room and an anechoic receiver room. Sometimes, a second reverberant room is used instead of an anechoic one. In between these two rooms, a testing window with a hosted test sample is foreseen. In the source room, a diffuse sound field is generated, in order to provide a random field excitation and avoid favourite incidence directions of the impinging waves. Following the diffuse field hypothesis which predicts that every point in time and space has an equal energy-content and frequency spectrum, the acoustic power level spectrum can easily be found by measuring the acoustic pressure in the room. The diffuse field excites the test specimen to vibrate which radiates into

the receiving room. The transmitted power is usually evaluated from the acoustic power intensity obtained scanning the radiating surface from the receiving room side. With this information the TL can be straightforwardly calculated as:

$$TL = 10 \log \frac{P_{in,source}}{P_{out,receiver}} \quad \text{Eq. 1-C}$$

Transmission room facilities provide a generally valid characterisation, independent of the facility, as long as the facility itself conforms to the standards. Nevertheless, the measurements are very cumbersome and time consuming. The investment for the infrastructure is also very high, which makes transmission facilities not the ideal method for a ‘quick’ assessment.

The setup at KU Leuven is a faster and more practical tool. As mentioned earlier, it is small, inexpensive and versatile. Although the procedures for measurements are similar as compared to measurements on transmission rooms, there are a number of differences.

The nature of the cavity loading on the test specimen is different; for a transmission room it consists of a diffuse field excitation, while a strongly modally dominated acoustic field is present in the KU Leuven cavity, as it is also the case in many typical applications, e.g. a car cavity. This is mainly due to its reduced dimensions. Only starting from 3 kHz the acoustic field becomes diffuse. Therefore, typically not TL, but Insertion loss (IL) is measured in this frequency range. Two measurements of the radiated sound power (evaluated with the intensity probe method as described above), with and without the test sample, are necessary for the IL calculation, as Eq. 2-C indicates.

$$IL = 10 \log \frac{P_{open}}{P_{closed}} \quad \text{Eq. 2-C}$$

Table 1-C. Key differences between a transmission room facility and the sound box setup

	Transmission suite	KU Leuven setup
Volume	2 x 80 m ³ (at least)	1 x 0.83 m ³
Cost	High	Low
Moveable	No	Yes
Acoustic loading	Diffuse field loading	Modal loading (up to 3 kHz) Diffuse field loading (above 3 kHz)
Measured quantity	Transmission Loss (TL)	Insertion Loss (IL)
Measured quantity dependency	Test specimen	Test specimen and setup

When evaluating this IL, one should bear in mind that it accounts also for the cavity modal behaviour and for the mutual coupling with the test sample dynamics.

A conceptual comparison between the presented setup and a standardised transmission room facility is summarised in Table 1-C.

3C.3 Numerical modelling tools

Element-based methods (FEM/BEM)

The Finite Element Method (FEM) [7] and the Boundary Element Method (BEM) [8] are the state of the art numerical tools for simulation of steady-state vibro-acoustics. These methods discretise the problem domain or its boundary into a large number of small elements in which polynomial shape functions interpolate the nodal values of the field variables.

The modelling procedure of the FEM and BEM typically consists of the following steps:

1. The problem domain (FEM) or its boundary (BEM) is partitioned into a large number of small elements.

Inside the domain (FEM) or on the boundary (BEM), the relevant dynamic field variables, here noted as $a(\mathbf{r})$, are approximated using polynomial shape functions $N_i(\mathbf{r})$ and nodal values a_i :

$$a(\mathbf{r}) \cong \hat{a}(\mathbf{r}) = \sum_{i=1}^{n_{fe}} a_i N_i(\mathbf{r}) \quad \text{Eq. 3-C}$$

2. Construction of the system of equations by enforcing domain and boundary conditions in a weak integral form.
3. Solution of the resulting system of equations, yielding the distribution of the relevant nodal values for the variables a in the domain (or on its boundary). In a post-processing step, these can be used to calculate the other (secondary) dynamic variables (e.g. acoustic intensity). Note however that this post-processing typically goes with a loss of resolution due to spatial derivatives of the polynomial shape functions.

The Wave Based Method (WBM)

The Wave Based Method (WBM) [9, 10] is an alternative deterministic prediction technique for steady-state vibro-acoustic problems. It is based on an indirect Trefftz approach [11] in that it uses exact solutions to the governing differential equation(s) as approximation functions for the dynamical field variables. For an elaborated discussion on the WBM and its positioning against FEM and BEM, the reader is referred to a selection of publications on the general principle of the WBM [9], its application to 3D bounded acoustics [15], its application to 3D unbounded acoustics [16].

The modelling procedure of the WBM generally consists of four steps:

1. The problem domain is partitioned into a number of convex (sub)domains.

The steady-state dynamic pressure field $p(\mathbf{r})$, is approximated by a solution expansion $\hat{p}(\mathbf{r})$ in terms of wave functions $\phi_w(\mathbf{r})$:

$$p(\mathbf{r}) \cong \hat{p}(\mathbf{r}) = \sum_{w=1}^{n_w} p_w \phi_w(\mathbf{r}) + \hat{p}_q(\mathbf{r}) \quad \text{Eq. 4-C}$$

2. Construction of the WB system of equations by enforcing the boundary conditions in a weak integral form.
3. Solution of the resulting system of equations, yielding the wave function contribution factors p_w . In a post-processing step, these lead to the desired dynamic field variables (e.g. acoustic pressure) or secondary dynamic variables (e.g. acoustic intensity) without loss of spatial resolution.

Hybrid approaches

As the WBM's convergence is only guaranteed in the case of convex subdomains, the subdomain division procedure can lead to a large number of subdomains and a large number of interface surfaces for geometrically complex problems. This has a negative impact on the WBM's efficiency; the model building time and model size strongly increase. Therefore, for geometrically more complex cases, hybrid methodologies have been developed and are under continuous research. In this family of hybrid methods [17, 18, 19, 20] the strong points of the WBM are combined with those of another numerical modelling technique. Table 2-C discusses the synergy between the FEM and the WBM in a hybrid FE-WB approach.

Table 2-C. Properties comparison between the FEM and the WBM

	FEM	WBM
Model size	Large	Small
Convergence rate	Medium	High
Frequency range	Low	Low + Mid
Geometrical complexity	High	Moderate

In practise, this means that the computationally efficient WBM is used for geometrically simple (sub) volumes and that the FEM takes care of the geometrical details.

3C.4 Experimental-numerical synergy

The use of numerical tools in the testing process can substantially enhance the measurements. This section therefore discusses the two configurations in which the test setup can be used and how a numerical counterpart model can be constructed, enabling the efficient interpretation of measurement results and identification of important setup- and test specimen parameters.

Internal configuration (acoustic damping materials)

1 Experimental

The closed cavity, which is essentially a small reverberant room due to the rigid cavity walls, can be easily used to measure the characteristics of acoustic damping materials. Typically test samples are put on the cavity floor. Acoustic excitation by means of a full-range speaker is provided and the Sound Pressure Level (SPL) is measured using an array of microphones (see Fig. 2-C).

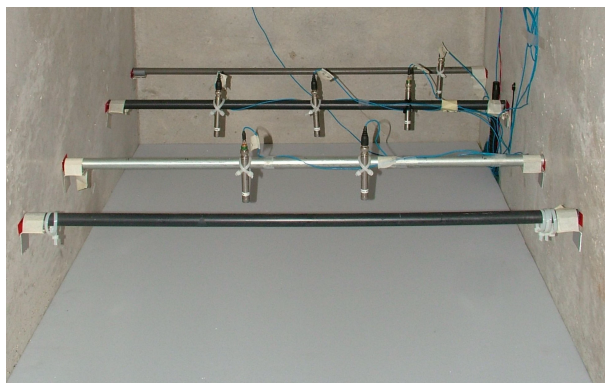


Fig. 2-C. Internal configuration with an acoustic damping material on the floor

2 Numerical

Following the conventional theories for porous damping materials, these values can be introduced in the acoustic cavity model in a number of ways [21].

A first approach describes the material's behaviour using a complex and frequency dependent impedance value, relating acoustic pressure and velocity on the boundary. For some classes of materials, especially those with a high flow resistivity (so-called locally reacting materials), this approach gives good results. A slightly more accurate modelling strategy is an equivalent fluid model. This strategy takes into account the full dynamic behaviour of the air inside the highly porous material and all viscous and thermal effects. Especially in the case of a rigid backing (like this configuration), these are a good choice.

If also the dynamic behaviour of the damping material's frame and the coupling to the air inside the material is important, the poroelastic Biot theory [22] should be considered. Given the backed configuration, this is however not considered in this paper.

Two numerical models will be compared, both based on the discretisation shown in Fig. 3-C. The first is a direct BE model with frequency dependent acoustic impedance representing the dynamic damping behaviour of the material. The second model is an FE model, including a homogenised equivalent fluid model for the material.

All cavity walls except the floor are considered acoustically rigid and the loudspeaker is modelled as an acoustic volume velocity source.

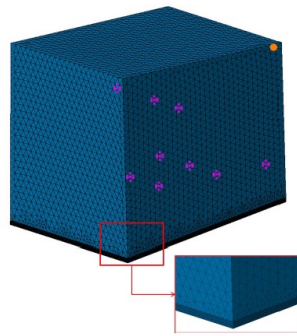


Fig. 3-C. Numerical counterpart model for absorption configuration

3 Comparison between experiments and simulations

The damping material, covering the full bottom floor, is a polyurethane foam and has been characterised in terms of its Biot parameters (see Table 3-C). Following the poroelastic theory in [21], these values can be translated in either a complex frequency dependent surface impedance value, or, in case of in a complex frequency dependent bulk modulus and fluid density for an equivalent fluid representation.

Table 3-C. Polyurethane foam material properties

Parameter		Value
Porosity	[-]	0.94
Flow resistivity	[Pa.s/m ²]	27700
Thickness	[m]	0.025
Tortuosity	[-]	1.2
Thermal length	[μm]	120
Viscous length	[μm]	40
Density	[kg/m ³]	65.2

Using these two models, the SPL at two microphones locations is computed and compared to direct measurements (see Fig. 4-C). A good agreement can be seen. Moreover, the two simulations (i.e. direct BE and FE) give very similar results. The good agreement shown between the two numerical methods suggests that the sound absorption properties of this type of foam can be modelled using a normal impedance condition as a good first order approximation.

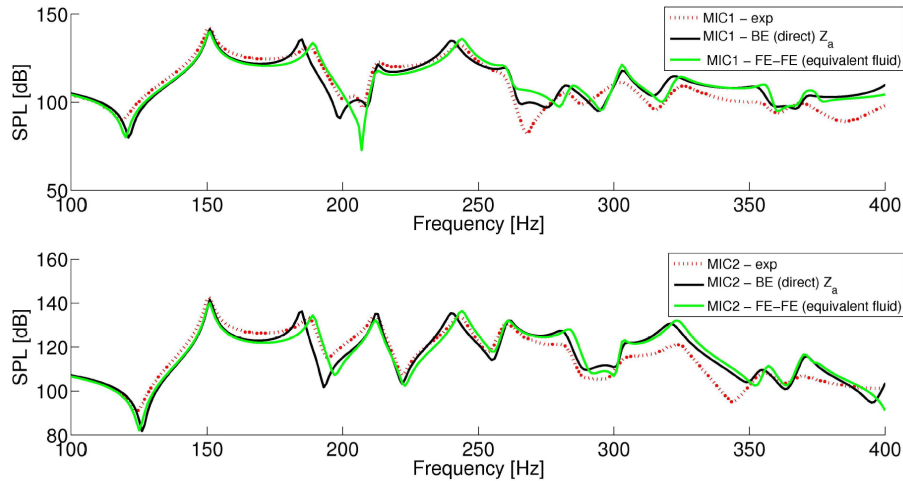


Fig. 4-C. SPL at two microphones inside the acoustic cavity with a damping layer (polyurethane foam) covering the full floor for experimental results (red dotted line), direct BE model with impedance (black solid line) and FE simulations with an equivalent fluid (green solid line)

External configuration (lightweight panels)

1 Experimental

The second, external configuration of the setup is based on the classical transmission suite. The difference with the previous configurations is obviously that in the external configuration the front wall no longer is completely closed; it now has a test window, that can be left open (e.g. Fig. 5-C), thus allowing the box to directly radiate sound to the environment or can host a test specimen. Using a 10 mm thick frame with a double bolt row, this specimen can be effectively clamped to the front wall. This way, the noise radiated by and through the panel can be evaluated.



Fig. 5-C. Intensity measurement in case of an open test window

The test specimen can be characterised in terms of acoustic insertion loss (IL) using two measurements – one with and one without the test panel mounted. In both configurations, the radiating surface, be it the open window or the plate mounted in the window, is scanned using an intensity probe.

As mentioned above, one should bear in mind when evaluating the IL that it accounts also for the cavity modal behaviour and for the mutual coupling with the test sample dynamics, whereas the classical Transmission Loss (TL) only incorporates panel behaviour and does not account for strong two-way vibro-acoustic coupling. However, in many typical applications (e.g. a car cavity), the vibro-acoustic coupling is very pronounced. The use of the IL on the sound box can thus be considered to be closer to the actual application. The fact that there no longer is a general, setup independent, characterisation is a small price that needs to pay for the increased versatility and the easiness of working with a small acoustic cavity.

2 Numerical

For both the open case, as for the case with the panel, a separate WBM counterpart model is constructed. Compared to the bounded WB model, a number of modifications are necessary.

As the interface between the test window and the inner cavity does not cover the whole frontal surface, a division into subdomains is desirable to prevent discontinuous boundary conditions, which could slow down the convergence. The 9 resulting internal subdomains are illustrated in Fig. 6-C by the dotted lines (.....).

Since the sound propagates through the test window, the acoustic domain exterior to the cavity also needs to be modelled. Fig. 6-C shows the hemispherical truncation sphere (—) where the transition between bounded wave functions and semi-unbounded wave functions which take care of the radiation. Within the truncation hemisphere, 6 additional bounded domains are added.

An FE model is added for the structure (Fig. 6-C right). The difference between the model for the open case (Fig. 6-C left) and the closed case (Fig. 6-C right) is in the coupling terms between the interior bounded and exterior bounded domain tangent to

the window in the front wall. For the open case, these domains are directly coupled to each other. In the case of a hosted panel, the interior and exterior acoustic domain are coupled through an FEM model of the panel in a hybrid way.

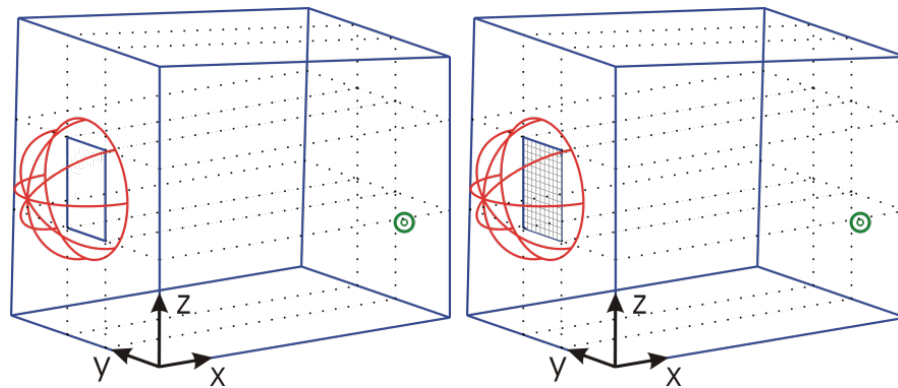


Fig. 6-C. Hybrid vibro-acoustic (FE-)WB model: Open (left) and with panel (right)

3 Illustration of the numerical-experimental synergy

As the WBM is a meshless method, it straightforwardly allows for model modifications, such as different panel configurations, boundary conditions, reinforcements, etc., without intensive remeshing steps. The combination of the experimental and the numerical approach facilitates easy measurement interpretation and allows for (inverse) material identification.

This is illustrated by the following case where the transmission through a 3mm aluminium A4-sized panel is studied. The clamping frame, which is designed to effectively clamp the sample to the box, is replaced by clamped edge boundary conditions. However, when comparing the experimental IL (Fig. 7-C) with simulations, clear discrepancies can be seen; both the level as well as on the position of the resonance-driven dips. This suggests that the panel boundary conditions are too stiff.

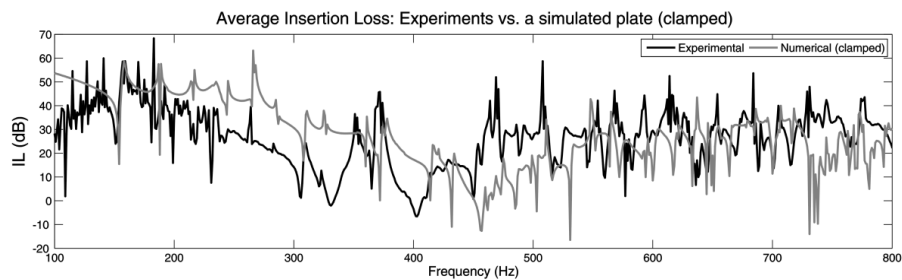


Fig. 7-C. Experimental vs. numerical IL for clamped boundary conditions

Through an updating of the rotational boundary conditions to a finite value, the boundary conditions become an intermediate case between clamped (infinite rotational stiffness) and simply supported (no rotational stiffness). This resulted in a value of 5300 Nm/rad/m, which is still quite stiff but finite, but can accurately predict the IL over the considered frequency range (Fig. 8-C).

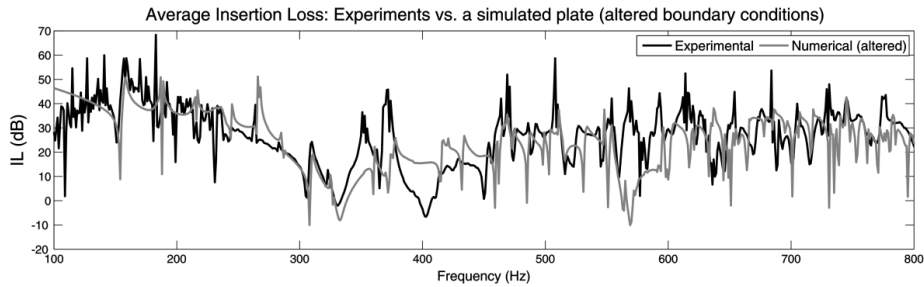


Fig. 8-C. Experimental vs. numerical IL for updated boundary conditions

Through the combination of measurements with experiments, the models can thus be effectively updated to better represent the physical reality of the measurements and to get a better view of what is actually measured. This offers a step-up towards material characterisation, where the parameters of unknown materials are updated by matching a numerical template model with the measurements.

3C.5 Conclusions

This paper presents the synergy numerical methods and measurements in the vibro-acoustic characterisation of lightweight materials, especially using a novel test setup for fast and easy characterisation of acoustic damping materials and lightweight panels.

From an experimental point of view, the setup allows for of both acoustic absorptive materials as well as lightweight panels of different sizes. It shows a high versatility; both airborne (by means of a full-range speaker) or structural (by means of an electrodynamic shaker or an impact hammer) can be applied and the response can be measured either acoustically (by means of microphones or intensity probes) or structurally (by means of lightweight accelerometers).

From a numerical point of view, simulation tools, such as the element-based approaches and the Wave Based Method can be used to predict the vibro-acoustic behaviour of the setup and the hosted material samples.

The synergy between experiments and simulations is discussed for two configurations of the setup:

- i. The acoustic cavity is closed: By placing an acoustic damping layer on the cavity floor, the properties of these layers (such as the absorption) can be investigated.

- ii. The cavity front wall has a window with a test panel. This configuration allows studying the transmission characteristics (such as the IL) of lightweight panels.

This synergy can be used either on its own, to validate and understand experimental results, as well as in an inverse approach to update model parameters. This combined numerical-experimental approach can lead to a very efficient method for *in situ* material characterisation. Using a parametric template model of the setup, relevant parameters can be estimated. The setup with support of efficient models could even be used to determine hard-to-measure microscopic variables, such as the Biot parameters for poroelastic foams from a limited number of macroscopic measurements.

Acknowledgements

The authors would like to acknowledge Marianna Vivolo for her valuable contributions. The research of E. Deckers is funded by a grant from the Fund for Scientific Research – Flanders (F.W.O.). Furthermore, the authors would like to acknowledge the European Commission for the ENLIGHT research project (GA 314567). The Research Fund KU Leuven is also gratefully acknowledged for its support.

3C.6 References

- [1] H. Martin, Sound transmission rooms - A comparison, PhD thesis, Technische Universiteit Eindhoven, 1986.
- [2] C. Gonzales Diaz, M. Vivolo, B. Pluymers, D. Vandepitte and W. Desmet, “Transmission suite design for vibro-acoustic characterisation of lightweight panels,” in ISMA 2010, Leuven, Belgium, 2010.
- [3] M. Vivolo, Vibro-acoustic characterization of lightweight panels by using a small cabin, PhD thesis, K.U.Leuven, division PMA, 2013.
- [4] S. Jonckheere, M. Vivolo, B. Pluymers, D. Vandepitte and W. Desmet, “Vibro-acoustic characterisation of lightweight structures: A numerical-experimental approach,” in 7th International Styrian Noise, Vibration & Harshness Congress (ISNVH2012), Graz, Austria, 2012.
- [5] O. Zienkiewicz and R. Taylor, The finite element method - The three volume set (6th ed.), Butterworth-Heinemann, 2005.
- [6] O. Von Estorff, Boundary elements in acoustics: Advances and applications, Southampton: Applicable mathematics series - WITpress, 2007.
- [7] W. Desmet, A wave based prediction technique for coupled vibro-acoustic analysis, PhD thesis, K.U.Leuven, division PMA, 1998.

- [8] E. Deckers, O. Atak, L. Coox, R. D'Amico, H. Devriendt, S. Jonckheere, K. Ku, B. Pluymers, D. Vandepitte and W. Desmet, "The Wave Based Method: an overview of 15 years of research," *Wave Motion* 51(2014) 550-565.
- [9] E. Trefftz, "Ein Gegenstück zum Ritzschen Verfahren," in 2nd international congress on applied mechanics, Zürich, Switzerland, 1926.
- [10] M. Blaszkak, "Acoustic design of small rectangular rooms: Normal frequency statistics," *Applied Acoustics* 69-12(2008) 1356-1360.
- [11] Acoustics - Determination of sound power levels of noise sources using sound pressure - Precision methods for reverberation rooms, ANSI/ASA S12.51-2002/ISO 3791 (1999).
- [12] Acoustics - Measurement of sound absorption in a reverberation room (ISO 354), 2003.
- [13] B. Van Genechten, O. Atak, B. Bergen, E. Deckers, S. Jonckheere, J. Lee, A. Maressa, K. Vergote, B. Pluymers, D. Vandepitte and W. Desmet, "An efficient Wave Based Method for solving Helmholtz problems in three-dimensional bounded domains," *Engineering Analysis with Boundary Elements* 36(2012) 63-75.
- [14] B. Bergen, B. Van Genechten, D. Vandepitte and W. Desmet, "An efficient Trefftz based method for three-dimensional Helmholtz problems in unbounded domains," *Computer Modeling in Engineering & Sciences* 61-2(2010) 155-175.
- [15] B. Van Hal, W. Desmet, D. Vandepitte and P. Sas, "Hybrid finite element - wave based method for acoustic problems," *Computer Assisted Mechanics and Engineering Sciences* 11(2003) 375-390,.
- [16] B. Van Genechten, B. Pluymers, D. Vandepitte and W. Desmet, "A hybrid wave based - modally reduced finite element method for the efficient analysis of low- and mid-frequency car cavity acoustics," *SAE International Journal of Passenger cars - Mechanical systems* 2-1(2009) 1494-1504.
- [17] B. Van Genechten, D. Vandepitte and W. Desmet, "A direct hybrid finite element - wave based modelling technique for efficient mid-frequency coupled vibro-acoustic analysis," *Computer Methods in Applied Mechanics and Engineering*, vol. 200, no. 5-8, pp. 742-764, 2011.
- [18] S. Jonckheere, E. Deckers, B. Van Genechten, D. Vandepitte and W. Desmet, "A direct hybrid Finite Element - Wave Based Method for the steady-state analysis of acoustic cavities with poro-elastic damping layers using the coupled Helmholtz-Biot equations," *Computer Methods in Applied Mechanics and Engineering*, vol. 263, pp. 144-157, 2013.
- [19] J. Allard and N. Atalla, *Propagation of Sound in Porous Media: Modeling Sound Absorbing Materials*, West Sussex, United Kingdom: John Wiley & Sons, 2009.
- [20] M. A. Biot, "The theory of propagation of elastic waves in a fluid-saturated porous solid," *Journal of the Acoustical Society of America* 28(1956) 168-191.
- [21] T. Courtois, C. Bertolini and J. Ochs, "A procedure for efficient trimmed body FE simulations, based on a transfer admittance model of the sound package," in 6th Styrian Noise, Vibration & Harshness Congress (ISNVH 2010), Graz, Austria, 2010.

- [22] U. Tengzelius, N. Horlin, U. Emborg, M. Gustavsson, H. Van der Auweraer and M. Iadevaia, Correlation of medium frequency and FE-models for a trimmed Aircraft test section, AIAA, no. 97, p. 1618.
- [23] M. Vivolo, B. Pluymers, D. Vandepitte and W. Desmet, Vibro-acoustic study of lightweight components based on a new experimental setup, in 18th International congress on Sound & Vibration (ICSV 18), Rio de Janeiro, Brazil, 2011.
- [24] P. Bouillard and F. Ihlenburg, "Error estimation and adaptivity for the finite element method in acoustics: 2D and 3D applications," *Computer Methods in Applied Mechanics and Engineering* 176(1999) 147-163.
- [25] S. Marburg, "Six boundary elements per wavelength: is that enough?," *Journal of Computational Acoustics of the Acoustical Society of America* 10(2002) 25-51.
- [26] Mid-Frequency Consortium, "Mid-Frequency" CAE Methodologies for Mid-Frequency Analysis in Vibration and Acoustics, 2012.
- [27] W. C. Sabine, *The American Architect*, 1900.
- [28] B. Pluymers, B. Van Hal, D. Vandepitte and W. Desmet, Trefftz-based methods for time-harmonic acoustics, *Archives of Computational Methods in Engineering* (2007) 343-381.
- [29] W. Desmet, B. Bergen, E. Deckers, B. Pluymers, B. Van Genechten, K. Vergote and D. Vandepitte, "A wave based prediction technique following a Trefftz approach: a possible solution to the mid-frequency modelling challenge in acoustics and vibration?!", in *Noise and Vibration: Emerging Methods (NOVEM2009)*, Oxford, United Kingdom, 2009.
- [30] B. Pluymers, Wave based modelling methods for steady-state vibro-acoustics, PhD thesis, K.U.Leuven (division PMA), 2006.
- [31] B. Bergen, B. Pluymers, B. Van Genechten, D. Vandepitte and W. Desmet, "A Trefftz based method for solving Helmholtz problems in semi-infinite domains," *Engineering Analysis with Boundary Elements* 36(2012) 30-38.

Annex 3D

An inverse methodology for low-frequency transmission loss characterization of a lightweight panel in a small reverberant transmission suite

Vittorio D'Ortona¹, Eugène Nijman¹

¹Virtual Vehicle Research Center, Inffeldgasse 21/A, 8010 Graz, Austria,
vittorio.dortona@v2c2.at, eugene.nijman@v2c2.at

Abstract. A new procedure for the low frequency Transmission Loss (TL) characterization of panels, by means of a small reverberant transmission suite is discussed. Moreover, in the case of lightweight panels the measurements are affected by a strong vibro-acoustic coupling between the sample tested and the fluid in the cabin, resulting in an unreliable TL prediction below the Schroeder's frequency. This paper proposes a novel methodology to retrieve the structural interface mobility matrix of lightweight panels, unaffected by the fluid coupling, using the Patch transfer Function (PTF) sub-structuring method. The retrieved mobility matrix allows then for reliable and standard-like TL predictions in different environments. This new approach has been numerically validated by a simple reference case of a homogeneous Aluminum plate coupled to a small cabin with simply supported boundary condition. The results show a very good matching between the known reference mobility and the estimated one. The limitations of this new procedure, possible applications and further studies are also discussed.

3D.1 Introduction

In order to investigate and predict Noise, Vibration and Harshness (NVH) properties of lightweight components, small reverberant chambers are being more and more implemented in the automotive, railway and aerospace fields. Compared to the standards (chambers of 80 m³), the dimensions of these chambers allow for building own designed testing, resulting to be practical and fast tools for testing and evaluating the vibro-acoustic behavior of lightweight panels of common use in the transport industry.

On the other hand, small reverberant chambers have a wide frequency region in which the field cannot be considered diffuse. The Schroeder's frequency is high, and below it a strong vibro-acoustic coupling between the sample and the cabin might be present. The achieved noise reduction properties are then affected by the test rig in which they are measured and cannot be considered as representative for the tested panel's behavior. The lack of diffusivity is a common issue for small cabins and it does not allow for reliable Transmission Loss (TL) investigations in the low frequency region. A test campaign performed by the author on a sandwich panel with honeycomb core [1] enlightens this problem by comparing the noise reduction

properties measured in a small reverberant chamber, designed at KU Leuven and named PMA Soundbox, with the TL measured in a standard facility.

In order to investigate the diffusivity problem, analytical and numerical models have been employed to show the influence of different parameters in the sound reduction index at low frequencies [2, 3]. Teresa Bravo and Stephen J. Elliot [4] try to address the problem from an experimental point of view by proposing the use of an array of loudspeaker, driven by partially uncorrelated signal in the near field of the partition, in order to reproduce a diffuse sound pressure field impinging on the tested surface. Although there exist a lot of experimental and theoretical work on the variability of measurements at low frequencies, no effective solution has been found to address this problem. It still represents a big issue about obtaining a complete characterization of the noise reduction properties of lightweight structures and generating trustworthy numerical models to predict their behavior in practical applications.

Here a fast and new indirect procedure to retrieve the mobility matrix of structural components in the fully vibro-acoustic coupled frequency region is introduced, independently from the environment in which it is tested. The methodology allow for the determination of the panel's mobility by using the PTF (Patch Transfer Function approach) and involving (i) direct measurements of the Sound Pressure Level on the inner surface of a sample tested in a small cabin, (ii) good knowledge of the acoustic characteristics of the test rig. The aim is to develop a hybrid numerical-experimental procedure in order to get, from a not standard test rig such as a small reverberant cabin, a reliable prediction of the standard noise and vibration properties of lightweight panels.

The present paper is structured as follow: an overview of the PTF method and its applications is given in the first section, then the proposed methodology is explained in detail and validated with a numerical reference case. In the last section, conclusions and an overview on possible future works are listed.

3D.2 Patch Transfer Functions approach

The PTF method has been initially developed with the goal to be a useful alternative tool to reduce the computational cost when solving coupled multi-system problems, while keeping a good accuracy in the results. Introduced by Ouisse et al. [6], it has been applied for acoustic coupling problems by Pavic [7], for a plate-cavity system by Aucejo et al. [8] and for transmission loss calculation of a multi-layer system by Chazot and Guyader [9]. A hybrid prediction scheme has been proposed and validates by Jan Rejlek et al. [10] to extend the PTF approach to vibro-acoustic systems containing numerically characterized fluid domains and experimentally characterized structural parts. Recently Veronesi et al. [11] implemented it to develop a novel experimental method for the characterization of poro-elastic materials.

3D.3 Methodology

The PTF approach is modular, allowing for different procedures (numerical, experimental, analytical solution) to be used in order to assess impedance relation of each sub-system. The presented methodology takes advantage of this feature in order to develop an indirect procedure to characterize the mobility of a panel coupled to a small cabin excited by a set of acoustic sources. The first step is to divide the entire system in two subsystems coupled on a coupling surface, and then apply the theorem formulated by Bobrovnitskii [5]. If one of the sub-systems hosts sound sources while the other is passive, the global sound field can be represented by the superposition of two simpler field components: the field produced by the running sources with the coupling surface fully blocked (blocked pressure field), and the one due to the velocity, at the coupling surface of the coupled system, when the internal sources are switched off. Applying this principle at the panel inner surface, i.e. the coupling surface, it is possible to retrieve its mobility. What is required is the knowledge of the following three quantities: the global pressure field, the blocked pressure field and the surface impedance of the fully blocked coupling surface.

Governing equations

Let us consider a simple fully coupled vibro-acoustic system (Fig. 1.a) consisting in a thin flat plate and a small cavity excited by a monopole source. For practical reasons the coupling surface is considered to match the interface of the two sub-system, i.e. the panel's inner surface.

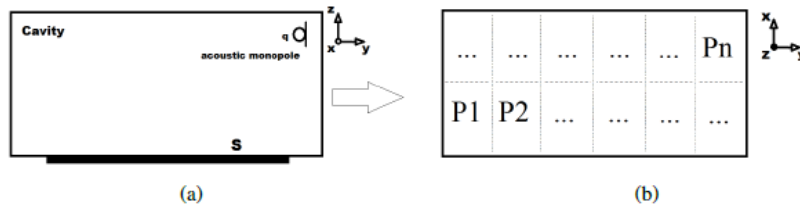


Fig. 2-D. Vibro-acoustic system: cavity, vibrating surface and acoustic monopole (a) - Division of the vibrating surface in N patches (b)

The PTF approach consists in subdividing the coupling surface S in N elementary surfaces ΔS_i (Fig. 1-Db), also referred to as patches. On each patch the dynamic quantities are averaged and considered to assume a constant value. For the i-th patch, the averaged pressure and velocity are given by:

$$\bar{P}_i = \frac{1}{\Delta S_i} \int_{\Delta S_i} P_i(x, y) dS \quad \text{Eq. 1-D}$$

$$\bar{V}_i = \frac{1}{\Delta S_i} \int_{\Delta S_i} V_i(x, y) dS \quad \text{Eq. 2-D}$$

For the subsystem cavity, the transfer functions between the j-th excited patch and the i-th receiving one can be written in terms of blocked impedance as follow:

$$Z_{ij} = \frac{\bar{P}_i}{\bar{V}_j} |_{\bar{V}_{k \neq j} = 0} \quad \text{Eq. 3-D}$$

For the subsystem plate the transfer functions between the j-th excited patch and the i-th receiving one can be written in terms of mobility as follow:

$$Y_{ij} = \frac{\bar{V}_i}{\bar{P}_j} |_{\bar{P}_{k \neq j} = 0} \quad \text{Eq. 4-D}$$

Z_{ij} represents the averaged pressure P_j of the i-th patch when a unit velocity is imposed on the j-th patch while keeping all the others patches blocked, i.e. $\bar{V}_k = 0$ for $k = 1, \dots, N$ and $k \neq j$. Y_{ij} represents the averaged velocity \bar{V}_i of the i-th patch when a unit pressure is imposed on the j-th patch while keeping all the others patches free, i.e. $\bar{P}_k = 0$ for $k = 1, \dots, N$ and $k \neq j$. Applying Eq. 3-D and 4-D to all the patches, the impedance and mobility matrix \underline{Z} and \underline{Y} can be built. They are symmetric square matrix with dimensions $N \times N$. Considering the acoustic sub-domain (indicated by the superscript 1), the total pressure on the i-th patch of the coupling surface, can be expressed as:

$$P_1^i = P_b^i + Z_{blocked}^{ij} V_j \quad \text{Eq. 5-D}$$

P_b^i is the averaged blocked pressure on the i-th patch due to the running source and keeping the coupling surface fully blocked. V_j is the velocity, at the coupling surface of the coupled system, when the internal sources are switched off. Writing Eq. 1-D for each patch, the vectors \bar{P}_1 and \bar{V}_1 can be built. They are vectors of dimensions $N \times 1$ containing respectively the averaged pressures and velocities on every single patch. Eq. 1-D can be than rewritten as follow:

$$\bar{P}_1 = \bar{P}_b + \bar{Z}_{blocked} \bar{V}_1 \quad \text{Eq. 6-D}$$

Because of the continuity conditions between the two sub-systems, the pressures and velocities acting on the coupling surface have to be the same:

$$\bar{P}_1 = \bar{P}_2 = \bar{P}_{interface} \quad \text{Eq. 7-D}$$

$$\bar{V}_1 = \bar{V}_2 = \bar{V}_{interface} \quad \text{Eq. 8-D}$$

Considering that \bar{P}_2 and \bar{V}_2 are related by mean of the panel's mobility as follow:

$$\bar{V}_2 = \underline{Y}_{panel} \bar{P}_2 \quad \text{Eq. 9-D}$$

Eq. 9-D can be used together with the coupling conditions 7 and 8 in Eq. 6-D, and changing the sign of V_2 when moving from sub-system 2 to subsystem 1, we obtain:

$$\bar{P}_S = \bar{P}_b - \underline{Z}_{blocked} \underline{Y}_{panel} \bar{P}_S \quad \text{Eq. 10-D}$$

With some algebra Eq. 10-D can be written as:

$$(\underline{I} + \underline{Z}_{blocked}\underline{Y}_{panel})\underline{\bar{P}}_S = \underline{\bar{P}}_b \quad \text{Eq. 11-D}$$

The aim is to indirectly retrieve the mobility matrix \bar{Y}_{panel} by using Eq. 11-D. For this purpose a matrix equation needs to be built. This goal can be reached by using a set of at least N acoustic loads. For the i-th acoustic excitation a vector equation like Eq. 11-D can be written:

$$(\underline{I} + \underline{Z}_{blocked}\underline{Y}_{panel})\underline{\bar{P}}_S^i = \underline{\bar{P}}_b^i \quad \text{Eq. 12-D}$$

Writing Eq. 12-D for each acoustic load, and considering that the matrices $\underline{Z}_{blocked}$ and $\underline{Y}_{surface}$ are constant, being characteristics of the system and independent from the acoustic load, a set of N equations can be built and grouped in a matrix form as follow:

$$(\underline{I} + \underline{Z}_{blocked}\underline{Y}_{panel})\underline{P}_S = \underline{P}_b \quad \text{Eq. 13-D}$$

$$\text{where } \underline{P}_S = [\underline{\bar{P}}_S^1 \quad \dots \quad \underline{\bar{P}}_S^i \quad \dots \quad \underline{\bar{P}}_S^N] \text{ and } \underline{P}_b = [\underline{\bar{P}}_b^1 \quad \dots \quad \underline{\bar{P}}_b^i \quad \dots \quad \underline{\bar{P}}_b^N].$$

Eq. 13-D can be solved for Y panel, obtaining:

$$\underline{Y}_{panel} = \underline{Z}_{blocked}^{-1}(\underline{P}_b\underline{P}_S^{-1} - \underline{I}) \quad \text{Eq. 14-D}$$

Care has to be taken in the choice of the acoustic loads set. As shown in Eq. 14-D the matrix \underline{P}_S has to be inverted, so the N acoustic excitations have to be such that a set of N independent pressure fields will be generated on the coupling surface.

The quantities \underline{Z}_{cavity} and \underline{P}_b are only related to the testing room and the complete knowledge of its properties (like for an in situ designed small reverberant chamber or for simple regular geometries) allows for calculating them via FEM/BEM or analytically. \underline{P}_S takes in account the global coupled response of the vibro-acoustic system and it can be experimentally achieved by mean of a set of microphones placed close by the inner surface of the tested panel.

3D.4 Numerical example

The proposed approach is presented here by means of a numerical example and the acquired mobility matrix compared with a reference one. As a vibro-acoustic system, a small rectangular cavity coupled to an homogeneous aluminum plate is considered (Fig. 1-D). The plate is 5mm thick and its dimensions on the xy plane are 1:5m and 0:3m along x and y directions respectively.

The panel surface is also considered as coupling surface, it covers entirely one wall of the cavity, which dimensions are then 1:5m, 0:3m and 0:4m along x, y and z. Simply

supported boundary conditions are imposed on each edge of the plate. The frequency range investigated goes from 0Hz to 250Hz.

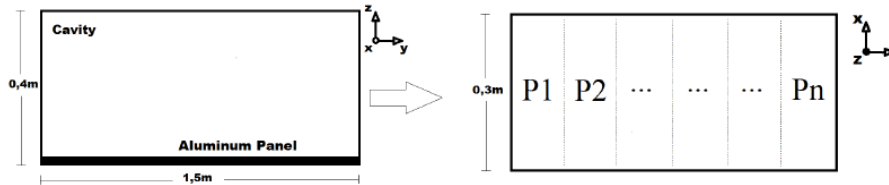


Fig. 3-D. Rectangular cavity and Aluminum plate's size

The material properties of the two subsystems are shown in Table 1-D.

Table 1-D. Material properties used for modeling the fluid inside the acoustic sub-domain and the Aluminum plate

Material	Density (Kg/m ³)	Phase speed (m/s)	Young's modulus (N/m)
Air	1,21	340	—
Aluminum	2770	—	72 * 10 ⁹
Material	Poisson's ratio (ν)	Damping ratio(ξ)	Absorption coefficient (α)
Air	—	—	0,005
Aluminum	0,33	0,001	—

In order to choose an optimal configuration for the number of patches to be used and for the typology of the subdivision in patches for the structural sub-system, a modal analysis has been performed in advance. Table 2-D shows acoustical and structural eigenfrequencies together with the associated number of half-wave along x and y , for the plate, and x , y and z for the cavity.

Table 2-D. The natural frequencies and semi-wave number of the related eigenmodes of each uncoupled system

Subsystem	Order	Eigenfrequency [Hz]	Type
Cavity	1	0	(0,0,0)
	2	113	(1,0,0)
	3	227	(2,0,0)
Panel	1	141	(1,1)
	2	157	(2,1)
	3	184	(3,1)
	4	222	(4,1)

In the frequency range of interest the panel has only mode shapes having one semi-wave along y, while the maximum number of semi-wave along x is four. The panel has been then divided in one row of 8 patches along x in order to have at least two patches for semi-waves in the whole frequency range analyzed. Is it important to

underline that only one row of patches along y has been used because of the pressure will change predominantly along x resulting, in the analyzed frequency region, quite constant along y instead. Having another row of patches would translate in adding more load cases and creating bigger matrices, increasing the computational cost and decreasing the quality of the mobility matrix prediction. Indeed, at a fixed coordinate x, the pressure on the two patches along y would be almost the same, generating in the matrix \underline{P}_s linearly dependent rows, which will give singularity problems.

Reference Mobility Matrix

The reference mobility matrix of the Aluminum plate has been calculated by mean of FEM analysis. A finite element model of the in vacuum plate with simply supported boundary conditions has been generated and 8 analysis have been performed. The i-th run consists in a frequency response analysis of the plate under a uniform unit pressure load acting on the i-th patch. At the i-th unit pressure load, the averaged velocity of the j-th patch corresponds to the component $Y_{reference}^{ij}$ of the reference mobility matrix, so, for each run, the structural frequency response has been averaged on each patch in terms of structural velocities allowing for the determination of the 8×8 $\underline{Y}_{panel}^{reference}$ matrix.

Blocked Impedance

The rectangular shape of the acoustic sub-system allows for the use of an analytical model, based on modal superposition, in order to determine the blocked impedance matrix $\underline{Z}_{blocked}$ on the coupling surface. In the acoustic sub-domain, the steady-state acoustic pressure perturbation field $p(\mathbf{r})$ is governed by the Helmholtz equation [12]:

$$\nabla^2 p(\mathbf{r}) + k^2 p(\mathbf{r}) = 0 \quad \forall \mathbf{r} \in \Omega_a \quad \text{Eq. 15-D}$$

where k the acoustic wave number and c the speed of sound. For a rectangular rigid cavity of dimensions L_x , L_y and L_z , the eigenmodes of the Helmholtz equation can be written as follow:

$$\phi_i(\mathbf{r}) = \zeta_i \cos\left(\frac{m_x(i)\pi x}{L_x}\right) \cos\left(\frac{m_y(i)\pi y}{L_y}\right) \cos\left(\frac{m_z(i)\pi z}{L_z}\right) \quad \text{Eq. 16-D}$$

$$\zeta_i = \sqrt{2^s}, \quad s = \text{sign}(m_x(i)) + \text{sign}(m_y(i)) + \text{sign}(m_z(i)) \quad \text{Eq. 17-D}$$

The Eigenfrequencies are:

$$\omega_i = \pi c \sqrt{\left(\frac{m_x(i)}{L_x}\right)^2 + \left(\frac{m_y(i)}{L_y}\right)^2 + \left(\frac{m_z(i)}{L_z}\right)^2} \quad m_x, m_y, m_z = 0, 1, 2, \dots \quad \text{Eq. 18-D}$$

with the integers $m(i)$ chosen to give a monotonous increase of ω_i with i increasing, $i = 1, 2, \dots$. The patch-to-patch impedance between two patches of size Δx , Δy and $\Delta x'$, $\Delta y'$ centered at r and r' , respectively, is given by Pavic [7] as:

$$Z_{blocked}(r, r') = i\omega\rho c^2 \Delta x \Delta y \sum_i \frac{\phi_i(r)\phi_i(r')}{\omega_i^2 - \omega^2 + 2i\varepsilon\omega} \operatorname{sinc}\left(\frac{m_{x,i}\Delta x}{2Lx}\right) \operatorname{sinc}\left(\frac{m_{y,i}\Delta y}{2Ly}\right) \operatorname{sinc}\left(\frac{m_{x,i}\Delta x'}{2Lx}\right) \operatorname{sinc}\left(\frac{m_{y,i}\Delta y'}{2Ly}\right) \quad \text{Eq. 19-D}$$

where ε represents the equivalent damping due to a small wall absorption coefficient $\alpha \ll 1$, and it can be expressed as:

$$\varepsilon = \alpha c \frac{1}{Lx} + \frac{1}{Ly} + \frac{1}{2Lz} \quad \text{Eq. 20-D}$$

The amplitude of a wave propagating with a speed c of is assumed to be reduced by α when traveling across the cavity length. Eq. 20-D is based on the simplification that in the z direction the damping is only half of the values in the other directions. That is because along z one surface is used for the coupling, this surface is then blocked per definition and therefore rigid without any damping.

Results

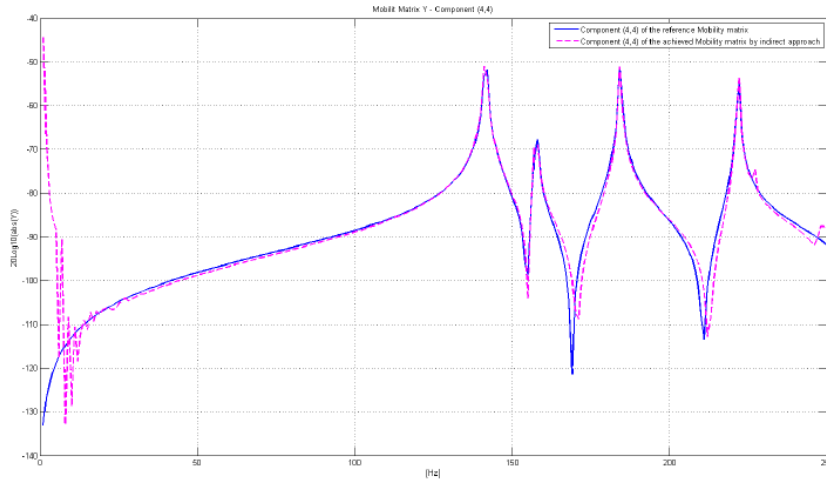


Fig. 4-D. Comparison between the component (4,4) of the reference Mobility matrix (blue curve) and the achieved one by mean of an indirect approach (dashed magenta curve)

In the last step, a set of $M > N$ different acoustic loads has been chosen and applied to (i) the FE model of the coupled vibro-acoustic system in order to retrieve \underline{P}_S , (ii) the

FE model of the sole acoustic sub-system having the coupling surface blocked in order to retrieve \underline{P}_b .

The reason why the number of acoustic loads is bigger than the number of patches, i.e. the minimum number of loads to solve the set of equations, is related to the necessity to get N independent pressures vectors \bar{P}_S^i . How to obtain this goal is not known a priori, so $M > N$ load cases have been used with a random choice of the monopoles' positions and a pseudoinverse matrix \underline{P}_S^{-1} has been calculated. A methodology to understand a priori how would be a set of exactly N load cases able to generate N independent pressure field \bar{P}_S^i is under investigation. Using Eq. 14-D the mobility matrix \underline{Y}_{panel} has been calculated and compared with the reference one $\underline{Y}_{panel}^{reference}$. Fig. 3-D shows a comparison between the components (4,4) of the above mentioned matrices.

Is it possible to notice how the two curves matches really well in the frequency range of interest? A small shifting of the anti-resonant peaks can be observed; it is related to the averaging process of the velocity over the patches.

3D.5 Conclusion

The proposed procedure has shown the capability to accurately estimate the mobility matrix of a homogeneous Aluminum plate by mean of an indirect approach. The procedure has only been validated numerically, but the possibility to experimentally apply this method to a small cabin reverberant chamber is quite appealing since (i) a coupled Sound Pressure Field can be achieved by acoustic measurements with a set of microphones placed inside the cavity, (ii) thanks to the deep knowledge about shape and acoustic properties of the test rig, it is possible to estimate the blocked impedance and blocked pressure matrices by mean of numerical simulations involving FE method.

The next step will be to validate the proposed approach by a set of experiments made on an Aluminum homogeneous plate coupled to a small rectangular cabin located at ViF's (Virtual Vehicles) laboratory in Graz.

Moreover, other three possible scenarios about future research works are now possible:

- To investigate the capability of scaling the acquired Mobility and predict the noise reduction properties of a standard sample in a standard facility.
- To investigate the feasibility of performing sensitivity studies in order to: (i) understand the influence of the test rig to the acoustic properties of the tested sample, (ii) correct the measurements to achieve a trustworthy experimental prediction of the noise reduction properties, i.e. to achieve standard like results unaffected by the test environment.
- To extend the presented method to the study of noise reduction properties of multilayer systems.

About the last point listed above, it is worth to mention that, for studying noise reduction properties of multilayer structures, methodologies based on sub-structuring

the global system are quite often used [9, 13, 14, 15]. Given a certain incident sound pressure field, the transmitted one is achieved going step by step through every single layer; so the knowledge of their characteristic impedance and/or mobility properties is crucial and not easy to get by a direct experimental procedure. A numerical approach is often used, so the possibility to experimentally apply the here introduced procedure is of great interest in order to tackle this issue in a faster, and easier to realize, way.

Acknowledgements

The research work of Vittorio D'Ortona has been funded by the European Commission within the ITN Marie Curie Action project eLiQuiD under the 7th Framework Programme (EC grant agreement no. 316422). The authors acknowledge the financial support of the COMET K2 - Competence Centres for Excellent Technologies Programme of the Austrian Federal Ministry for Transport, Innovation and Technology (BMVIT), the Austrian Federal Ministry of Science, Research and Economy (BMWFW), the Austrian Research Promotion Agency (FFG), the Province of Styria and the Styrian Business Promotion Agency (SFG). Finally, the authors gratefully acknowledge the support of COST action TU1105.

3D.6 References

- [1] V. D'Ortona, M. Vivolo, B. Pluymers, D. Vandepitte and W. Desmet, Experimental identification of noise reduction properties of honeycomb panels using a small cabin. In Proceedings of Transport Research Arena 2014, TRA 2014, Paris, France, 2014.
- [2] T. Kihlman, On the meaning of the sound reduction index at low frequencies. *Acustica*, 18, 11-20, 1967.
- [3] W. Kropp, A. Pietrzyk, T. Kihlman, Sound radiation into a rectangular room. Applications to airborne sound transmission in buildings. *Acta Acustica*, 2, 379-392, 1994.
- [4] T. Bravo and S. J. Elliott, A Simulation Analysis of Low Frequency Sound transmission Measurements. In Proceedings of International Congress on Acoustic 2004, ICA 2004, Kyoto, Japan, 2004.
- [5] Y. I. Bobrovnikskii Y, A theorem on the representation of the field of forced vibrations of a composite elastic system. *Acoustical Physics*, 47, 507-510, 2001.
- [6] M. Ouisse, L. Maxit, C. Cacciolati and J. Guyader, Patch transfer functions as a tool to couple linear acoustic problems. *Journal of Vibration and Acoustics*, 127, 458-466, 2005
- [7] G. Pavic, Air-borne sound source characterization by patch impedance coupling approach. *Journal of Sound and Vibration*, 329(23), 4907-4921, 2010.
- [8] M. Aucejo, L. Maxit, N. Totaro and J. Guyader, Convergence acceleration using the residual shape technique when solving structure-acoustic coupling with the patch transfer functions method.

- [9] J. Chazot and J. Guyader, Prediction of transmission loss of double panels with a patch mobility method. *Journal of the Acoustical Society of American*, 121, 267-278, 2007. *Computers & Structures*, 88(11-12), 728-736, 2010.
- [10] J. Rejlek, G. Veronesi, C. Albert, E. Nijman, A Combined Computational-Experimental Approach for Modelling of Coupled Vibro-Acoustic Problems. In *Proceedings of Society of Automotive Engineers 2013 Noise and Vibration Conference and Exhibition*, SAE 2013 Noise and Vibration Conference and Exhibition, Grand Rapids, Michigan, USA, 2013.
- [11] G. Veronesi, C. Albert, E. Nijman, J. Rejlek, Patch Transfer Function Approach for Analysis of Coupled Vibro-Acoustic Problems Involving Porous Materials. In *Proceedings of Society of Automotive Engineers 2014 Noise and Vibration Conference and Exhibition*, SAE 2014 Noise and Vibration Conference and Exhibition, Graz, Austria, 2014.
- [12] F. Fahy, *Sound and Structural Vibration: Radiation, Transmission and Response*. Academic Press, ISBN 0122476719, 2000. *Journal of Sound and Vibration*, 233(4), 669-705, 2000.
- [13] M. Villot and al., Predicting the acoustical radiation of finite size multi-layered structures by applying spatial windowing on infinite structures. *Journal of sound and vibration*, 245(3), 433-455, 2001.
- [14] M. Villot and al., Using spatial windowing to take the finite size of plane structure into account in sound transmission. In *Proceedings of International Conference on Emerging Technologies of Noise and Vibration Analysis and Control 2005*, NOVEM 2005, Saint Raphael, France 2005.
- [15] H. Nelisse, T. Onsay, N. Atalla, Structure borne insertion loss of sound package components. In *Proceedings of Society of Automotive Engineers 2003 Noise & Vibration Conference and Exhibition Technical Papers*, SAE 2003 Noise & Vibration Conference and Exhibition Technical Papers, Traverse City (MI), 2003.

Annex 3E

NVH Signature Analysis of Electric Drive Systems

Mathieu Sarrazin, Karl Janssens, Colin Andersen, Herman van der Auweraer

Siemens Industry Software NV, Interleuvenlaan 68, 3001 Leuven, Belgium,
mathieu.sarrazin@siemens.com

Abstract. This chapter reviews. The integration of electric motors in a wide range of vehicles creates multiple challenges, of which the Noise-Vibration-Harshness (NVH) behaviour is an important one, quite different in nature and engineering approach than this from a conventional Internal Combustion Engine (ICE). Contrary to the low-order acoustic noise from an ICE, the electric driveline sound features multiple pure and modulated high-frequency tones which, despite their low level, are perceived as unpleasant. The type of electric motor, the power electronics, the control strategy and the vehicle integration aspects all contribute to this signature and hence need to be investigated. Moreover, the motor controller and its construction interact with each other as a full system causing structural vibrations and noise by multi-physic coupling rendering source identification a difficult task. This contribution shows that multiple causes affect the acoustic radiation of the driveline in its environment, including the Power Control Units (PCU), the working principle and the configuration of the machine. A comprehensive experimental analysis in the electric and vibro-acoustic domain provides insight in these aspects.

3E.1 Introduction

Automotive manufacturers have to comply with stringent standards to assure the competitiveness of their products [1]. The introduction of the electric motor in road vehicles causes that decades of experience in designing brand-specific sounds, based on noise and vibration generated by combustion engines, cannot be transferred to the new generation [2]. The differences in the sound produced by the powertrain in the electric and ICE driven vehicles *can be* summarized as follows [3]:

- (1) Hybrid and Electric Vehicles (HEV) feature new source components such as the electric motor(s), the control unit(s) and the battery (e.g. cooling). These components feature different frequency characteristics and working conditions than conventional combustion engines. Typical are the tonal components caused by the magnetic fields during electric driving and regenerative braking. In addition, the Variable Speed Drive (VSD) modulation generates typical off-zero harmonics in the noise spectrograms due *to* the non-sinusoidal motor supply voltage produced by the VSD. All these harmonics are perceived as unpleasant whining or whistling noise in the vehicle interior.
- (2) Due to the reduced masking effect of the internal combustion engine (ICE) in EV, the noise of secondary sources such as the transmission, the HVAC system, the oil/water pump, the tyres, etc. become audible.

The discussion will further focus on the harmonic structure of the noise generated by the electric drivetrain, i.e. the drive, the controller and the motor. Tire noise [4] and other phenomena are not considered. Two electric motor types, a PMSM (Permanent Magnet Synchronous) and a SRM (Switched Reluctance) machine and their drives are studied in order to evaluate their behaviour inside a vehicle body. In the following sections, it is demonstrated that the impact of the different motor design variables, the electrical topology and the stator/rotor configuration, and the control methodology have a significant influence on the noise and vibration levels. Different measurements with a high quality data acquisition system are performed to assess the electric driveline signatures in the electrical and the vibro-acoustic domain.

3E.2 Noise and Vibration Sources in Electrical Drivelines

In most electric drive systems, the dominant acoustic response is produced by the magnetic forces which are generated by the stator currents. Fig. 1-E shows the flow of an acoustic noise generation process for an electrical machine. In a first step, the phase currents flowing through the stator coils generate time-varying radial forces in the air gap between the stator and rotor poles. In a second step, these radial forces excite vibrations in the stator which are propagated through the mechanical structure. The largest vibration levels arise when the natural modes of the stator are excited by the pulsating radial forces [5, 6]. In a final step, the deformations of the machine, the stator and the attached components, cause air vibrations resulting in pressure differences detectable by the human ear.

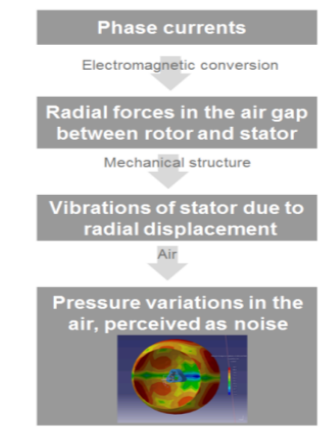


Fig. 1-E: Acoustic noise generation process

Electric drive systems require, next to the electric machine itself, power electronics based VSDs to control the rotational speed. Semiconductor-based components are implemented to allow the transformation of a DC-voltage into a controllable AC-voltage through high frequency switching. The control action of these switches corresponds to a modulation. One of the most common used modulation methods in electrical powertrains is the Pulse Width Modulation (PWM) technique. A drawback

of this particular technique is the generation of higher harmonics in the voltage and current signals (Fig. 2-E). The off-zero harmonics modify the air gap flux density distribution spectrum and consequently the magnetic noise, the vibration and the acoustic spectra. The new harmonic content depends on four main parameters: the applied control strategy [7], the switching frequency, the inverter bridge configuration and the motor configuration. To remove the acoustic noise generated by the Power Control Unit (PCU), the switching frequency can be increased above the human audible boundary of 20 kHz. However, the switching losses will increase and decrease the efficiency of the whole driveline.

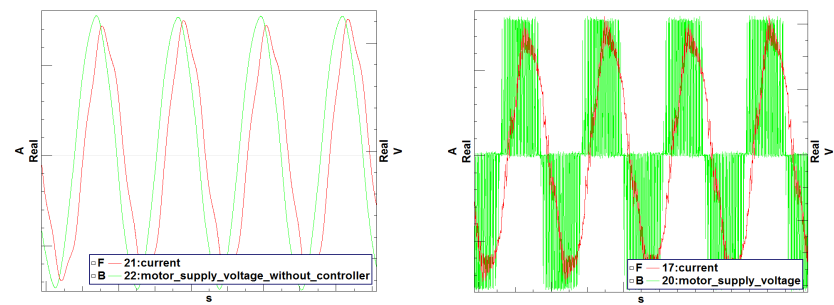


Fig. 2-E: Line-to-line voltage and stator winding current supplied by an AC grid of 50Hz (left) and a PCU (right)

Finally, additional mechanical noise can make the noise spectrum even more complex. The main causes of pure mechanical vibration are unbalance, misalignment, looseness and distortion, defective bearings, gearing and coupling inaccuracies, various forms of resonances, rotor/stator misalignments, bent rotor shafts. The way the electric powertrain is mounted inside the vehicle also impacts the structure borne and airborne transmission through multiple paths and hence the dynamic design of machine and the structural connections, require a proper understanding of the interactions that take place among for example these viscoelastic mounts and the neighboring structures. Eventually, the vibration and the noise radiated by the electrical powertrain can be classified into two big categories: i) the electromagnetic noise related to the motor configuration, stator or rotor structure, and the supply and ii) the pure mechanical noise related to the full assembly.

3E.3 Examples of Signature Analysis for (H)EV Applications

An analysis of the frequency spectrum as a function of the rotation speed (so-called “signature analysis”) was performed on two types of road vehicles, a panel truck and a passenger car. One vehicle is equipped with SRMs and the other one with PMSMs (Table 1-E).

Table 1-E: Studied (H)EV applications

	Vehicle case 1	Vehicle case 2
Motor type	SRM	PMSM
Rotor with permanent magnets	No	Yes
Stator winding principle	Concentrated	Distributed
Control switching frequency	Random	Fixed
Number of electrical phases	4	3

Electric vehicle with two 8/6 SRMs

In this first case, the experiments were performed under laboratory conditions where a battery electric vehicle prototype was installed on a four-wheel chassis dynamometer. The electric car had two SRMs [8]. Both SRMs consist of a rotating part, a laminated rotor with six salient poles, and a static part, a laminated stator with eight salient poles. Concentrated coils are located on the stator similar to a DC-machine. The SRM working principle is based on minimum reluctance, the magnetic analogy of an electrical resistance: the rotor will align itself with the magnetic field to minimize the reluctance of the magnetic field. In order to have self-starting capability and bidirectional control, the stator has more poles than the rotor. The SRMs are connected to each other through a gearbox with a single gear transmission ratio.

An extensive set of measurements was performed including several simultaneously acquired electrical, acoustic and vibration recordings, for different operational speeds and road load conditions. The accelerations and the sound pressures were measured at a large number of locations inside the vehicle, both in the motor and passenger compartment. Two types of results are further discussed: from data obtained while driving at a constant speed and from data obtained while accelerating from zero to a certain speed. By means of a special high quality angular position sensor (“zebra tape”), an optical sensor and the corresponding gear ratio, an accurate prediction of the rotational speed is reached.

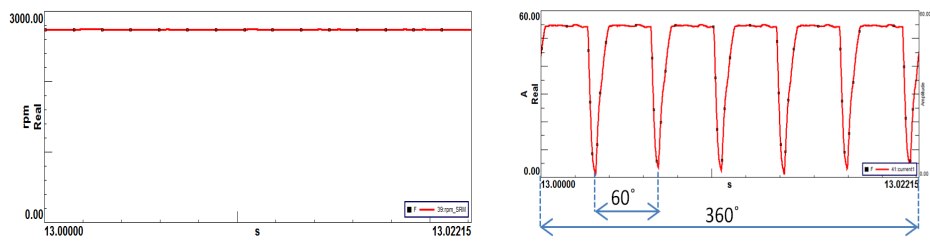


Fig. 3-E: One phase current signal (right) and corresponding rotation speed profile (left) of a 4 phase 8/6 switched reluctance motor

Fig. 3-E shows for a SRM the relation between the mechanical rotational frequency derived from a measured phase current time signal and the mechanical shaft speed (2739rpm) obtained from a tacho measurement. Both frequencies are equal to 45Hz. In one rotation of 360 mechanical degrees, each stator phase should be excited six times per revolution for a four-phase 8/6 SRM.

The order spectra of three measurement time signals at a constant rotational speed of 2739 rpm or 55kph wheel speed are reflected in Fig. 4-E. A clear correlation is shown between the spectra of a phase current profile, a motor vibration on the stator shell and a sound signal close to the motor. It is clearly visible that order six and its harmonics are dominant in the three signals which is a result of the pulsating pattern of the time current shape. The following relation exists between the fundamental frequency f , the rotational speed N_s , the rotor poles R and the first dominant order O_1 :

$$f = \frac{N_s * R}{60} = \frac{N_s * O_1}{60} \quad [1]$$

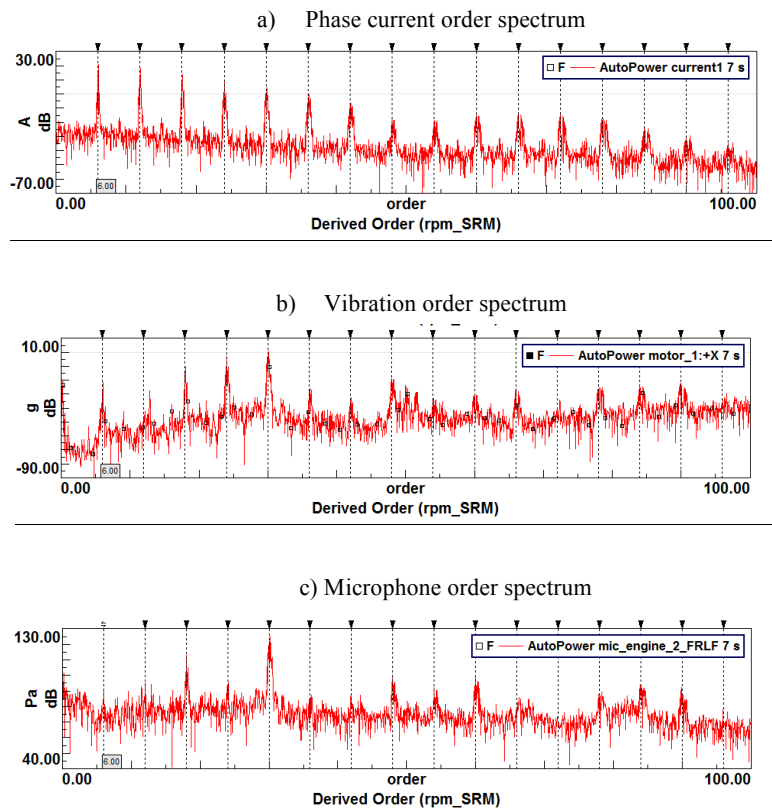


Fig. 4-E: Spectrum analysis of simultaneous recorded signals at a constant speed operation

A next step is to compare these three signals as a function of the rotational speed during a run-up from 0 to 110kph. In this way, it can be assessed that the dominant motor harmonics are indeed dependent on the rotational speed of the SRM. Fig. 5-E shows a spectrogram of the current, sound pressure and vibration as a function of the rotational speed. The dB-level of these motor harmonics is dependent on the torque level applied to the machine. The higher the torque level, the higher the sound pressure levels of the motor orders.

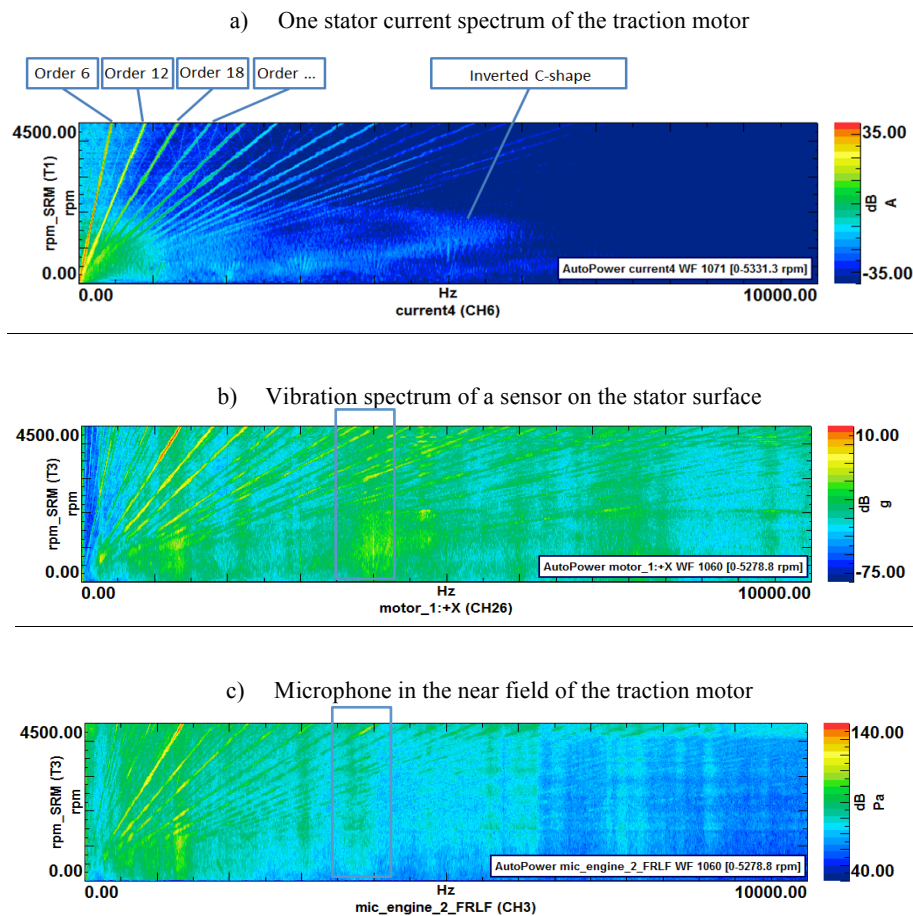


Fig. 5-E: Spectrograms of simultaneous recorded signals in run-up condition (0kHz - 10kHz)

Another interesting phenomenon is the current ripple phenomenon, the inverted c-shape which can also be noted in Fig. 5-E. It is a combined effect of the chopping function of the SRM controller and the back EMF produced inside the machine. At low and intermediate rotational speed a higher current ripple is present [9]. Due to the low back electromotive force (EMF), a quit rectangular current pulse with a ripple

profile is present which goes finally through the excited phase coils. At higher speeds, the back EMF increases and the current pulse is no longer rectangular, becoming slightly triangular and with a much lower ripple contribution. Soft chopping procedures [10] can reduce the current ripple and switching losses.

The presented results show that the shape and amplitude of the phase current are key control factors to optimize the sound radiation of a SRM. A reason is that the radial force and torque is directly dependent on the square of the current. The natural resonant frequency of the stator mode shapes are excited by these harmonics [9]. Typically, this phenomenon is marked by an increased amplitude of the harmonics at that specific resonance frequency. In the end, a typical tonal acoustic character is obtained by the presence of the radial magnetic forces in the air gap between the stator and the rotor.

In the higher frequency range (10 kHz to 20 kHz), no higher off-zero switching harmonics, originating from the PCU of this electrical machine, are present. The hysteresis control [11] of a SRM produces a broadband frequency content in the higher frequency range.

Hybrid vehicle with two interior PM motors tested in pure electric mode

A large class of current (H)EV is powered by interior permanent magnet synchronous machines (IPMSMs). In this case study, some results of a NVH analysis are shown for this type of machine. The test object is a hybrid vehicle equipped with two brushless IPMSMs and one ICE. IPMSMs have theoretically a sinusoidal distribution of the magnetic flux in the air gap and sinusoidal phase current shapes. As in the previous example, this vehicle has also been thoroughly investigated in different driving cycles. The presented results relate to measurements conducted while driving in pure electric vehicle mode. Each electric machine has a single layer topology (Fig. 6-E), eight interior permanent magnets and a different stator slot configuration, on with distributed stator windings and the other one with concentrated stator windings.

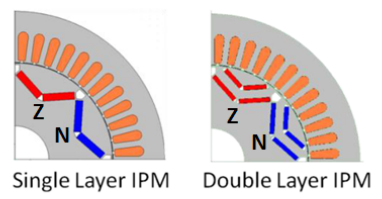


Fig. 6-E: Single layer and double layer topologies [12]

(H)EV applications use variable reluctance resolvers to control the electric machine with an angle position signal. This allows to directly derive the angular speed from available signals. The measured excitation signal and the two output signals of the variable reluctance resolver are decoded to get the rotational speed using a demodulation algorithm in combination with a Finite Impulse Response (FIR) filter

and the inverse tangent method. An extra resolver validation measurement was carried out with a zebra tape inside the wheels.

In PM motors, the mechanical and the electrical position are two important parameters. The mechanical position is related to the rotation of the rotor shaft. When the rotor has completed 360 mechanical degrees, the rotor is back in its original start position. The electrical position of the rotor is related to the rotation of the rotor magnetic field. Fig. 6 shows a cross section of a quadrant of a three-phase machine with eight magnetic poles, four pole pairs, and with 48 stator tooth. In case of a four pole pair PM machine, the rotor needs to rotate 90 mechanical degree to reach an identical magnetic configuration as its start position. The electrical rotor position is then related to the number of magnetic pole pairs inside the rotor. The electrical and the mechanical angular positions of the rotor are linked to each other by:

$$\theta_e = \theta_m * p \quad [2]$$

with p the number of pole pairs, θ_e the electric rotor position and θ_m the mechanical rotor position. The relation between position and angular speed is $\omega = d\theta/dt$:

$$\omega_e = \omega_m * p \quad [3]$$

In the ideal case, when a linear electrical load is connected to the system; it draws a pure sinusoidal current at the same frequency as the fed voltage to the machine but usually with a certain phase shift between the two signals:

$$\begin{aligned} I_a &= I \cdot \sin(\omega_e \cdot t) \\ I_b &= I \cdot \sin\left(\omega_e \cdot t - \frac{2\pi}{3}\right) \\ I_c &= I \cdot \sin\left(\omega_e \cdot t - \frac{4\pi}{3}\right) \end{aligned} \quad [4]$$

$$\begin{aligned} V_a &= I \cdot \cos(\omega_e \cdot t) \\ V_b &= I \cdot \cos\left(\omega_e \cdot t - \frac{2\pi}{3}\right) \\ V_c &= I \cdot \cos\left(\omega_e \cdot t - \frac{4\pi}{3}\right) \end{aligned}$$

The machine is in general powered from a symmetric and balanced three phase system which means that the applied voltages are shifted 120 degrees.

In real electric vehicle applications, the electric driveline components affect these signals which lead to many harmonics beside the fundamental harmonic. Fig. 7-E shows for a PMSM the relation between the mechanical rotational frequency derived from a measured phase current time signal and the mechanical shaft speed (3240rpm) obtained from a resolver measurement. Both frequencies are equal to 54Hz.

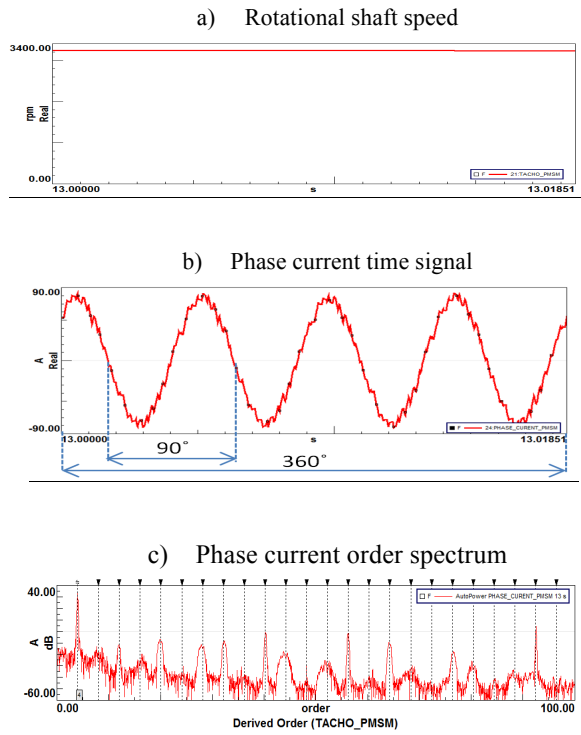


Fig. 7-E: One measured phase current signal in time-domain and frequency-domain with the corresponding rotational shaft speed profile of a 8-pole PWM-fed PMSM

A close relationship is also shown between the fundamental harmonic in the phase current spectrum, the rotor configuration and the rotational speed:

$$f = \frac{N_s * p}{60} = \frac{N_s * O_1}{60} \quad [5]$$

where f is the supply frequency of the synchronous motor, N_s the rotational speed, O_1 the first dominant order and p the number of pole pairs. By using eq. 3, the fourth order in the phase current order spectrum of Fig. 7-Ec corresponds to the pole pairs of the electrical machine. This shows that the dominant order inside the phase current signature, obtained by digital signal processing algorithms, is related to the physical rotor configuration of a PMSM. Some of the current harmonics related to the dominant order, the 4th order, come also back in the noise and vibration signature.

The electric phase current frequency-domain spectrum as well as the NVH spectra in Fig. 8-E show typical modulation phenomena caused by the VSD. These structures consist of central carrier frequencies surrounded by pairs of motor speed dependent sidebands. The first such structure appears around 2.5kHz which is the switching frequency of the IGBTs. The amplitude of the phase current harmonics is PWM control methodology related [7]. The harmonic noise emissions are mainly situated at twice the switching frequency, which is located within the most sensitive human hearing area, 2kHz to 5kHz, which can be very annoying. Similar phenomena are found in powertrains using induction motors and their VSD. Tuning of the PWM switching frequency can change the perceptibility in terms of sound quality allowing obtaining a suitable design [7]. To assess these effects, a virtual car sound synthesis tool is developed enabling to examine the sound perception of electric drivelines including these harmonic phenomena [13]. The tool uses measured signals, a Sound Quality Equivalent Model (SQEM) and contains algorithms to improve sound perception. This enables to engineer a brand specific sound and allows reproducing typical sound features of HEV during real-time driving simulations.

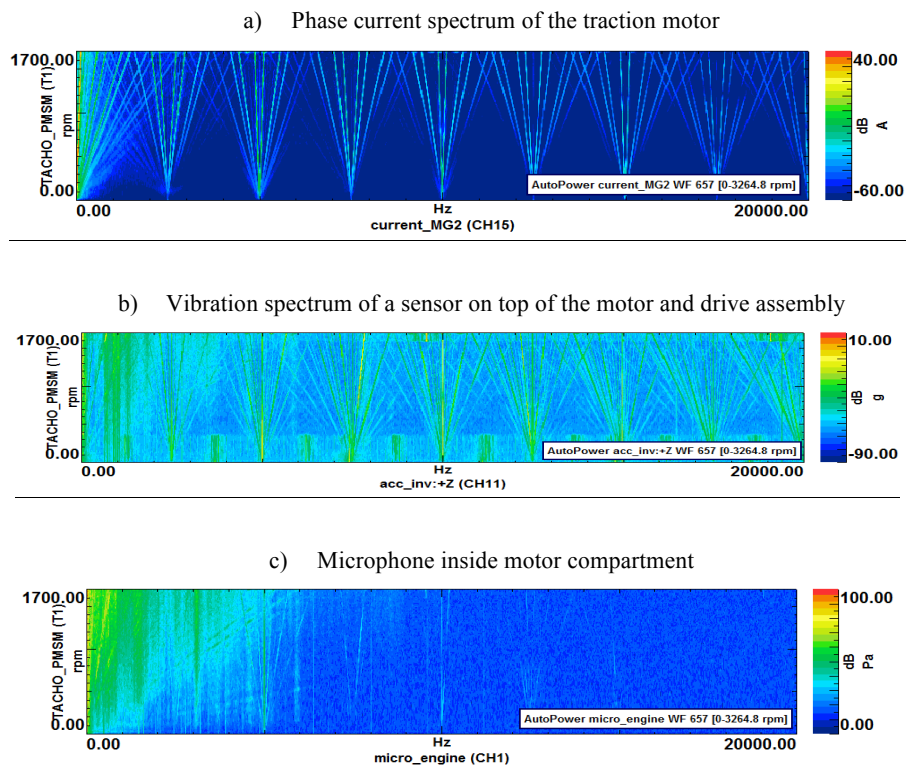


Fig.8-E: Phase current (above), vibration (middle) and noise (below) spectrum (0kHz – 20kHz)

3E.4 Conclusions

The noise and vibration signatures of hybrid and electric vehicles appear to be significantly different from those encountered with ICE powered vehicles. High frequency high order harmonics and fan-shaped modulation structures with kilohertz center frequencies are among the most characteristic phenomena, depending each on the electric motor type and the current control strategy and power electronics chopping frequency. A detailed understanding of the nature and origin of these signatures is required to allow to take the proper noise control measures in all phases of the vehicle design. A main conclusion is that decades of experience in designing brand-specific sounds for ICE driven vehicles cannot be transferred to the upcoming electric vehicles.

In the present study, advanced digital signal processing tools to analyze the spectral content of signals in a frequency range from 0Hz to 20kHz have been introduced with simultaneously recorded multiphysics measurement data. Two case studies were discussed in more detail, involving electric drivelines tested in different operational conditions to correlate and to explore harmonic components by means of the frequency representation of the vibration, acoustic noise and phase currents time signals. For example, a very clear relationship exists between the frequency spectra of the phase current, vibration and sound signals acquired on a SRM. It is also shown that both a PMSM and the controller introduce harmonics in the low frequency and high frequency ranges. A spectrogram in function of the rotational speed is a useful way to present and to compare current, noise and vibration frequency data of rotating machines. Ultimately, one can assess the particular sound and vibration character of two types, a PMSM and a SRM drive. Finally, all these tools help engineers on one hand to obtain insight in the electro-vibro-acoustic behavior of the full electric powertrain and on the other hand to optimize the final prototype in an early design process.

3E.5 References

- [1] H. Tischmacher, I.P. Tsoumas, B. Eichinger, U. Werner, "Case studies of Acoustic Noise Emission From Inverter-Fed Asynchronous Machines", IEEE transaction on Industry Applications 47(5), 2011.
- [2] G. Eisele, K. Wolff, M. Wittler, R. Abtahi, S. Pischinger, "NVH of Hybrid Vehicles", SIA Conf. on NVH of Hybrid and Electric Vehicles, Saint-Ouen, Paris, France, 4 Feb. 2010.
- [3] H. Van der Auweraer, k. Janssens, "A Source-Transfer-Receiver Approach to NVH Engineering of Hybrid/Electric Vehicles", SAE Technical Paper 2012-36-0646, 2012, doi:10.4271/2012-36-0646, SAE NVH Brazil 2012.

- [4] M. Sarrazin, C. Colangeli, K. Janssens, H. Van der Auweraer, "Synthesis techniques for wind and tire-road noise", *Internoise 2013*, Innsbruck, Austria, 2013.
- [5] W.C. Lo, C.C. Chan, Z. Zhu, D. Howe, K. Chau, "Acoustic noise radiated by PWM – controlled induction machines drives", *IEEE Trans. Ind. Electr.*, 47(4), 2000, pp. 692-697.
- [6] F.L.M. dos Santos, J. Anthonis, F. Naclerio, J. Gyselinck, H. Van der Auweraer, L. Sandoval Goes, "Multiphysics NVH Modeling: Integrated Simulation of a Switched Reluctance Motor Drivetrain for an Electric Vehicle", *IEEE Transactions on Industrial Electronics*, 61(1), 469 – 476, 2014, DOI 10.1109/TIE.2013.2247012 .
- [7] M. Sarrazin, K. Janssens, H. Van der Auweraer, "Influence of inverter PWM control schemes on noise signature of electric powertrains", *ICSV 20*, Bangkok, Thailand, 2013.
- [8] R. Krishnan, "Switched Reluctance Motor Drives: Modeling, Simulation", CRC Press, 2001.
- [9] M. Sarrazin, S. Gillijns, J. Anthonis, K. Janssens, H. Van der Auweraer, "NVH analysis of a 3 phase 12/8 SR motor drive for HEV applications", *EVS 27*, Barcelona, Spain, r 2013.
- [10] F. Blaabjerg, P.C. Kjaer, P.O. Rasmussen, C. Cossar, "Improved Digital Current Control Methods in Switched Reluctance Motor Drives", *IEEE Trans. Power Electronics*, 14(3), 1999.
- [11] A.V. Rajarathnam, K.M. Rahman, M. Ehsani, "Improvement of hysteresis control in switched reluctance motor drives", *IEEE International Electric Machines and Drives*, Seattle, WA, 1999..
- [12] I. Urquhart, D. Tanaka, R. Owen, Z.Q. Zhu, J.B. Wang, D.A. Stone "Mechanically actuated variable flux IPMSM for EV and HEV applications", *EVS 27*, Barcelona, Spain, 2013.
- [13] M. Sarrazin, K. Janssens, H. Van der Auweraer, "Virtual Car Sound Synthesis Technique for Brand Sound Design of Hybrid and Electric Vehicles", *SAE Technical Paper 2012-36-0614*, 2012, doi:10.4271/2012-36-0614, SAE NVH Brazil, 2012.

Annex 3F

Interior and exterior noise evaluation of bus concepts for public transportation

Alessandro Fortino¹, Jan-Welm Biermann¹, Lutz Eckstein¹ and Jens Viehöfer²

¹Institut für Kraftfahrzeuge - RWTH Aachen University, Germany,
fortino@ika.rwth-aachen.de

²fka Forschungsgesellschaft Kraftfahrwesen mbH Aachen, Germany
viehoefer@fka.de

Abstract. Fully and partially electric powertrain systems are increasingly used in the automotive sector in order to reduce the consumption of fossil fuels and related carbon gas emissions. Furthermore, the urban air quality and noise pollution can be improved by means of locally emission-free propulsion possibilities in electric drive mode. Besides the use of electric drives in the passenger car segment, another area of application of this drive concept is in the field of city buses for public transportation. In research projects such as CIVITAS DYN@MO alternative bus concepts are assessed for their impact on the environment and passengers by the Institute for Automotive Engineering (ika), RWTH Aachen University. On the one hand, achievable fuel savings and reductions of pollutant emissions are measured directly in field tests. On the other hand, the interior and exterior noise is evaluated in realistic driving maneuvers, such as bus departures with full and partial load acceleration. For this purpose, the noise and vibration in the passenger compartment and the radiated exterior noise are measured and analyzed. Based on these results, conclusions are drawn about the passengers' driving comfort and the impact on urban noise emissions.

3F.1 Introduction

Noise pollution represents one of the major environmental impairment in the residential area. Surveys of the Federal Environment Agency have shown that noise is perceived as more disturbing than air, water or waste pollution [1]. In this context, the road traffic resembles the most significant noise source. Since excessive noise exposure can lead to serious health risks, the Federal Environmental Agency and the World Health Organisation (WHO) defined a series of measures with regard to noise caused by road and rail traffic. One measure is the continuous reduction of noise limit values for road vehicles measured in the type approval test (pass-by noise test). However, a significant improvement on the urban noise pollution cannot be determined. Different reasons lead to this effect, e.g. increasing traffic volume and driving speeds in the past decades [2].

For this reason, inner-city environmental noise is extensively collected and mapped on the basis of the EU directive 2002/49/EC [3]. Various means of transportation contribute to the overall noise pollution and a separation between the individual noise sources would be very complex. Therefore, abstract calculation methods have been

developed for the determination of noise pollution that are currently used in practice and optimized [4].

In this context, the noise emissions caused by the public transportation and especially urban buses have to be considered as an important aspect. Besides conventional diesel buses, Municipal Transport Services are increasingly using alternative bus concepts (e.g. diesel electric hybrid buses) to reduce the fuel consumption of the fleet and to improve the urban noise and pollutant emissions. With onboard diagnosis hard- and software, objective values regarding the effective fuel consumption and pollutant emissions such as CO₂ and NO_x are obtained directly in the daily line operation taking the topology of the city as well as the speed and load profile of the bus into account. Exterior noise measurements for a general comparison between different buses cannot be carried out in the same way since reflecting objects and different background noises reduce the comparability. Thus, the noise emissions are measured in the same test environment as for the type-approval test. The buses are operated in representative driving maneuvers and the measuring equipment is placed on defined positions in order to determine the impact on the urban soundscape. In parallel to the evaluation of the exterior noise, the interior noise and the vibrations are measured and analyzed, as well. By distributing microphones and accelerometers in the passenger compartment it can be verified if innovative bus concepts can satisfy the increasing expectations regarding driving comfort.

3F.2 Methodology

With the ongoing urbanization, important goals are to improve the mobility and life quality of citizen. This is also the aim of the research project CIVITAS DYN@MO in which a total of 28 local partners in four European cities are implementing measures in the areas of sustainable transportation development planning, clean vehicles and improved traffic management [5]. In this context, city buses do not only have the primary task of transporting passengers under adequate conditions to their desired destination but they also have to meet economical and ecological demands in their operational environment. First investigations show that alternative bus concepts, e.g. with hybrid powertrains, deliver promising results to fulfill especially the ecological requirements [6]. Considering the aspect of noise emission and driving comfort, a total of six buses with different powertrain concepts have been investigated in the framework of this project to determine the potential of innovative bus concepts. An overview of the tested vehicles is given in Fig. 1-F.

vehicle type	powertrain	vehicle length
MAN Lion's City Hybrid	diesel electric hybrid	12 m
Mercedes Benz Citaro G BlueTec Hybrid	diesel electric hybrid	18 m (articulated)
ASEAG Electric (converted hybrid bus)	full electric	18 m (articulated)
VDL Citea LLE – 120 (lightweight bus)	diesel engine	12 m
Mercedes Benz Citaro	diesel engine	12 m
MAN Lion's City	diesel engine	18 m (articulated)

Fig. 1-F. Test vehicles of the research project CIVITAS DYN@MO

To maximize the variety of the conducted test series, diesel electric hybrid buses with different electric ranges and vehicle lengths are measured and compared to conventional diesel buses of the same length as a reference. Since the electric operation offers advantages regarding pollutant and noise emissions, the “Aachener Straßenbahn und Energieversorgungs AG” (ASEAG) converted an articulated hybrid to an all-electric bus. By removing the diesel engine and all corresponding components and adding battery packs with a total capacity of approximately 180 kWh the necessary range for a daily operation has been achieved [7].

In addition to the alternative powertrain concepts, vehicles based on lightweight structures are focused more and more in order to reduce the carbon gas emissions. Thus, an investigation of the NVH characteristics of this vehicle type is also included in this comparison.

3F.3 Measuring procedure

During the legally required type approval test, the noise emissions of buses are measured and evaluated for vehicle speeds above 30 km/h [8]. Contrary to this, the average speed of urban buses in most city cycles is in-between 5 and 15 km/h [9]. In order to evaluate the acoustic behavior of the different bus concepts in statistically more representative test conditions, test series with typical driving maneuvers and operating states have to be conducted.

One of the most typical driving maneuvers is the arrival and departure at bus stops with passengers getting off and on the bus. For that reason, variations of this maneuver are considered with different incoming speeds for deceleration and load conditions for acceleration. Accelerations with the right amount of partial load lead to best results regarding the efficiency of the powertrain and thus lowest energy consumption values. This is especially important for electric bus concepts with limited driving range caused by the capacity of the installed battery packs. Nevertheless, full load accelerations represent the most common bus departure maneuvers and therefore this driving condition also has to be included.

After the bus finished accelerating to the desired travelling speed, the next important driving condition is characterized by constant vehicle speed and low load. Three representative speeds in the urban area (15 km/h, 30 km/h and 50 km/h) are thus chosen for the test series. Depending on the operating strategy of the tested hybrid buses each maneuver is carried out with purely electric powertrain as zero emission vehicle (ZEV) and in addition with running diesel engine as hybrid electric vehicle (HEV).

The noise emitted by buses, which are powered by a diesel engine or an electric powertrain, is generated by several components. In addition, the body structure of a bus consisting of tubular steel profiles together with panels, the floor structure and additional parts (e.g. glass panes) represents a highly complex, vibro-acoustic system which needs to be taken into account, as well.

The following partial sound sources contribute in general to the overall noise of buses:

- Components of the conventional powertrain, including exhaust and intake system
- Components of the electric powertrain, e.g. the electric machines and inverters
- Auxiliary units, e.g. the climate control, battery cooling and pneumatic system
- Tire/road noise
- Aerodynamic (wind) noise

In order to increase the comparability of the tested vehicles' noise emissions, all measurements are carried out on the ika test track with conditions according to ISO 10844. For the evaluation of the exterior noise, on the one hand microphones are placed in a distance of 7.50 m to the centre line of the driving lane and 1.20 m height according to the measuring positions of ISO 362-1 [8].

On the other hand, a binaural measuring system (artificial head) is placed at a representative position for a pedestrian standing on a bus station to analyze the bus stop maneuvers in more detail. Fig. 2-F shows the sensor positions for the exterior noise measurements with a hybrid bus standing in the simulated bus stop.

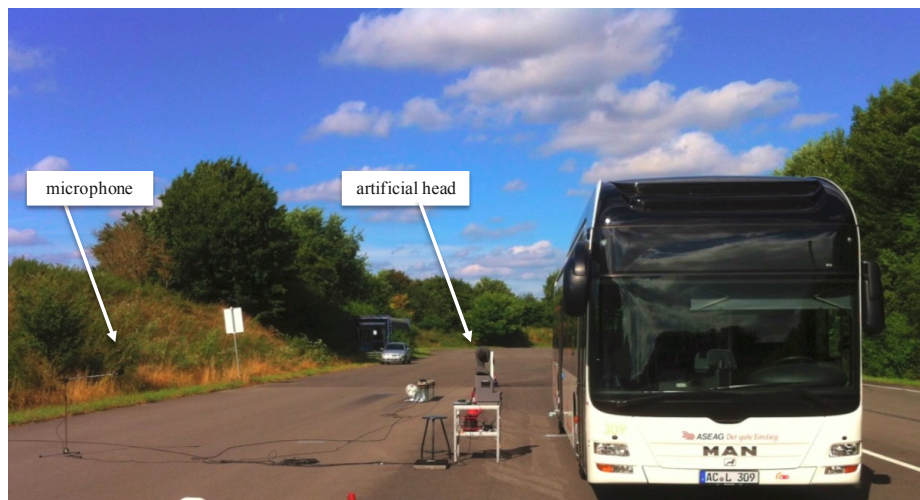


Fig. 2-F. Measuring positions exterior noise

The noise and vibration behavior in the vehicle interior is measured with accelerometers and microphones on each axis and at relevant positions regarding the driving comfort (grab handles, floor and seats). All microphones are set to a height of 1.50 m and an additional artificial head is placed in the last seating row. With a microphone placed at the driver's position, it is also possible to evaluate the impact of the different bus concepts on the driver's working environment. The sensor positions for the interior noise measurements are displayed in Fig. 3-F for an exemplary, articulated bus.

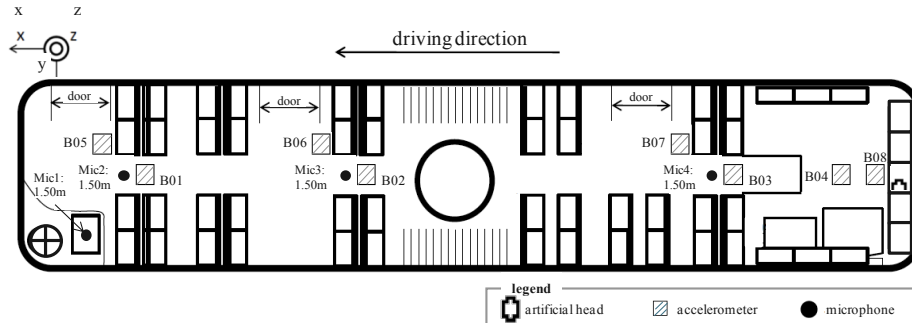


Fig. 3-F. Measuring positions interior noise and vibrations

By installing additional light barrier, telemetry and GPS systems, triggered and time-synchronous measurements for the exterior and interior noise are obtained. In this way, occurring noise phenomena can be correlated between the different measurements.

3F.4 Exterior noise

As a basic analysis method, the A-weighted sound pressure level is calculated for the evaluation of the exterior noise. The resulting level curves are plotted against the buses' distance instead of the measuring time. By defining the position of the artificial head (bus stop) as a reference point (0 m), the emitted noise is evaluated in dependency of the relative distance to the bus stop. In Fig. 4-F the sound pressure level of the pass-by tests with constant speeds is shown for the converted electric bus and a conventional diesel bus as reference. For the evaluation of these maneuvers, the microphone in a distance of 7.50 m instead of the closer artificial head is used in order to reduce the influence of air turbulences of the passing bus on the measuring result.

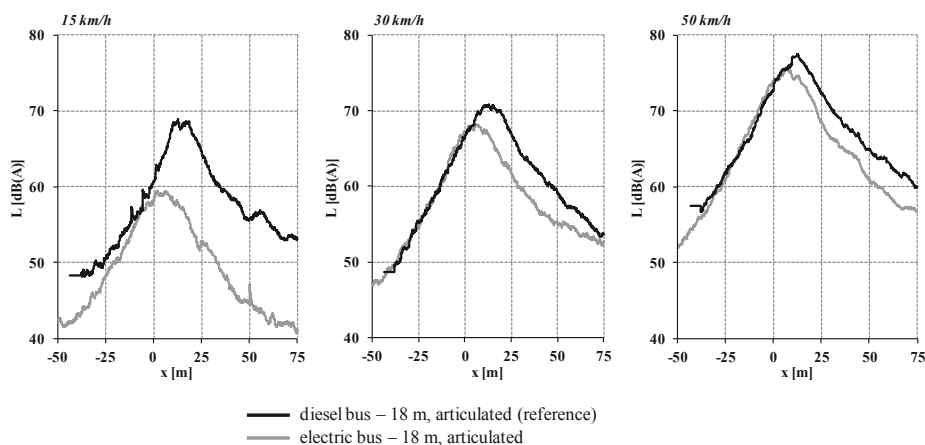


Fig. 4-F. Measured exterior noise for pass-by tests with constant speeds

It can be noticed, that it is possible to reduce the noise emissions with a pure electric powertrain at all driving speeds. Due to the increasing dominance of tire-/road and wind noise at higher vehicle speeds, the biggest difference between the buses can be observed at a speed of 15 km/h and is continuously narrowed in the tests with 30 and 50 km/h. For approaching vehicles (negative distance values), the level curves are almost identical and no significant difference between the two bus concepts can be noticed. But when the buses drive past the microphone position, the location of the maximum value is shifted in case of the diesel bus and an almost constant offset occurs for the departing buses (positive distance values). This effect is based on the missing diesel engine of the electric bus, which is typically located in the back of urban buses. Thus, the electric operation of buses does not only have advantages regarding the maximum noise emissions but also the average noise exposure whilst passing with constant speed.

This characteristic is even more distinctive considering bus departure maneuvers with partial and full load (Fig. 5-F). For this evaluation the right ear of the artificial head has been chosen since it is oriented into the driving direction of the bus.

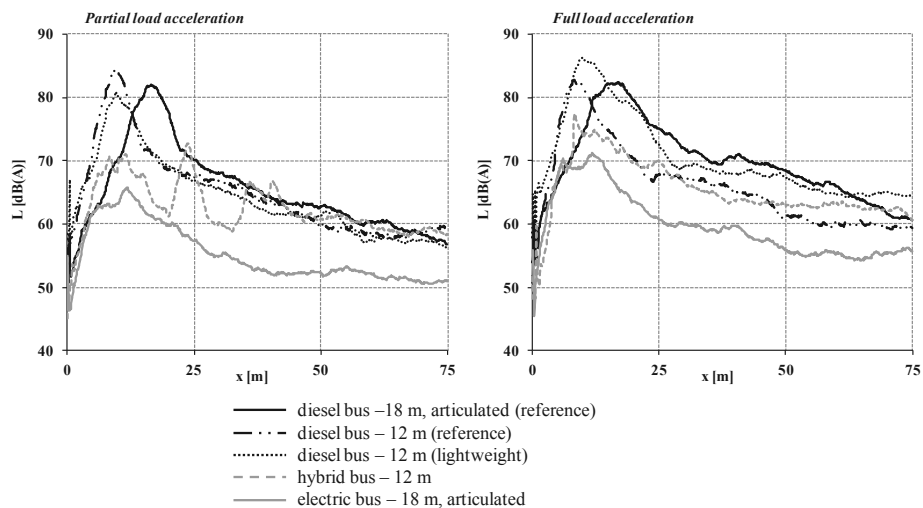


Fig. 5-F. Measured exterior noise for bus departures

In case of the diesel buses, a significant peak value of more than 80 dB(A) occurs in the moment the diesel engine and exhaust pipes pass the microphone position. Since the articulated bus is 6 m longer, the peak is shifted by this length in the diagrams. The highest values are measured for the lightweight bus when accelerated with full load. This could be caused by two reasons. Either the powertrain emits overall more noise or the vibrations are not damped as good as in the other buses due to the reduced mass of the lightweight structure. The analysis of the interior noise and vibrations will give a better insight to this matter.

A reduced first peak can be determined in the analysis of the noise emissions of the hybrid bus during partial load acceleration due to an electric start (5 m to 15 m). Resonance effects in the electric powertrain lead to a second peak in a distance of approx. 24 m before the diesel engine is switched on in a distance of 33 m. Once the diesel engine is running, the emitted noise level is almost identical to the measured conventional buses without electrical powertrain. The high resonance peak of the electric driven hybrid bus shows very well that although electrical powertrains offer a high potential of reducing noise emissions, the powertrain and the mounting concept have to be developed with care to avoid unwanted effects. Based on the first maximum value and compared to the results of the conventional diesel buses, the departure with the hybrid bus in partial load acceleration leads to a noise reduction of more than 10 dB. Accelerating the hybrid bus with full load still delivers better results regarding the maximum noise reduction, but the difference to the diesel buses amounts to only 5 dB. The reason is the low electric range of this bus concept, which stores the recuperated electrical energy in supercapacitors. Compared to Li-Ion batteries, this energy storage type has the advantage of fast exchange of electrical charge and therefore potentially absorbs more energy during fast retardation of the bus. The disadvantage is the limited capacity and thus the diesel engine is switched on in an early distance of 8 m because the stored energy is consumed very fast in full load acceleration maneuvers.

During the bus departure maneuvers the lowest exterior noise emissions are measured for the converted and all-electric bus both for partial and full load accelerations. With regard to the maximum sound pressure level a reduction of more than 16 dB has been enabled. But even in the further progress an average reduction of 10 dB can be determined over the entire measuring distance. Subjectively, this bus will be perceived less than half as loud as conventional buses and thus offers a high potential for reducing urban noise pollution. Of course, the prerequisite for this is an increased percentage of electric buses in the fleet of Municipal Transport Services.

3F.5 Interior noise and vibrations

The interior noise and the vibrations are evaluated in the same maneuvers as the exterior noise. For the tests with constant vehicle speed, energetic average values are calculated for each measuring position over the entire measuring duration ($t > 15$ seconds). This method can be applied because the measured signals can be described by periodic signals with nearly constant levels.

The analysis of the airborne noise is realized by the calculation of the A-weighted sound pressure level. For the analysis of the structure-borne noise, the measured accelerations are also weighted in all three spatial directions in order to evaluate the perceived driving comfort of passengers. The measured accelerations are frequency weighted according to VDI 2057 for whole-body excitation [10] and vibrations introduced into the hands [11]. With the help of these filtering curves (W_k , W_d and W_h) an analysis closer to the subjective vibration perception can be conducted. The corresponding frequency weighting curve has to be chosen in dependency of the strain criterion, the body position (sitting or standing) as well as the direction and

point of entry of the vibration. In order to analyze for example the well-being of a standing passenger, the filter curve W_k shall be used in the z-direction and W_d in the x- and y-direction for vibrations measured in the foot platform. The filter curve W_h is used for all three spatial directions for the analysis of hand / arm vibrations which are introduced over a hand holding a grab bar. In order to improve the clarity of the test results, the weighted vibrations are not analyzed in the single spatial directions, but summarized to a vibration total value according to Eq.1-F.

$$a_{wv} = \sqrt{a_{wx}^2 + a_{wy}^2 + a_{wz}^2} \quad \text{Eq. 1-F}$$

The results of the constant speed tests regarding the measured sound pressure levels (Fig. 6, top) and accelerations concerning whole-body excitation (Fig. 6-F, bottom) is again shown for the electric bus and the articulated diesel bus as reference.

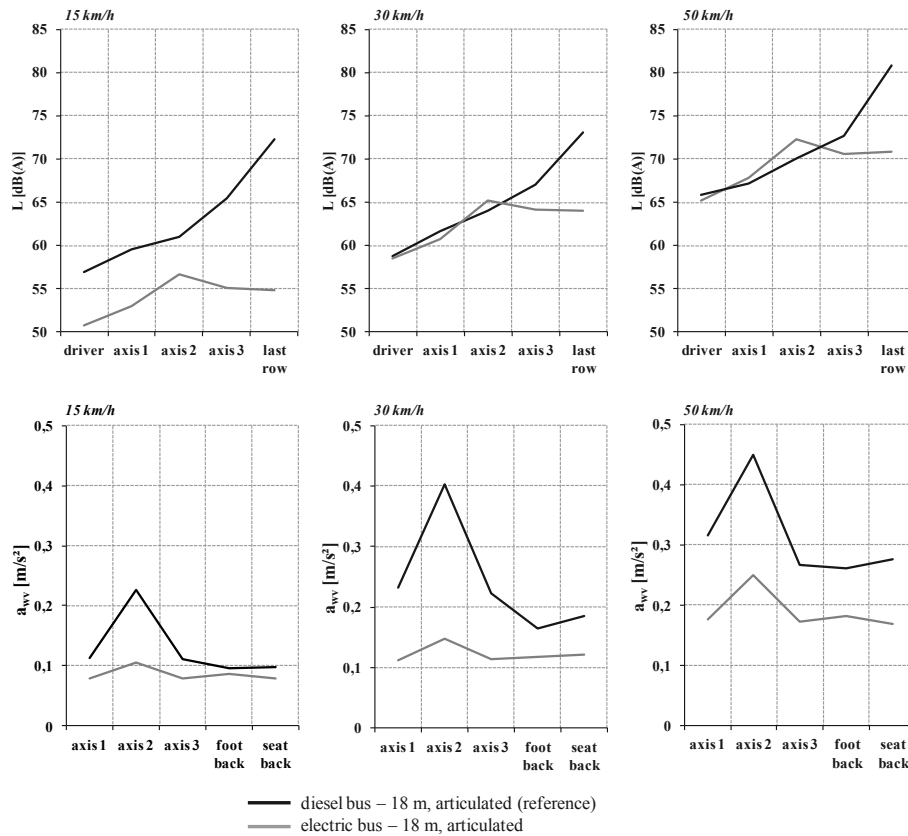


Fig. 6-F. Interior noise and vibrations at constant driving speeds

Due to the missing diesel engine in the back of the electric bus, the biggest differences regarding the air-borne noise measurements are obtained behind the articulation on the measuring positions on the last axis and in the last seating row.

Noise reductions from 10 to 17 dB can be observed in the back of the electric driven bus. In front of the articulation differences in the sound pressure level can also be noticed at low driving speeds, whereas at higher speeds the level values are almost identical in this area.

In the analysis of the frequency weighted accelerations, lower vibrations can be determined at all sensor positions and driving speeds for the electric bus. Interestingly, the highest vibrations of the diesel bus are measured on the first and second axis and not near to active parts of the powertrain. This leads to the assumption that in this bus the major part of structural vibrations is caused by roadway excitations when driven with constant speeds and low torque/power required for propagation.

By operating the buses with partial and full load accelerations, the influence of the load can be evaluated over a wide range of vehicle speeds. Fig. 7-F shows the sound pressure levels and total accelerations (unweighted) for selected buses and measuring positions in full load acceleration maneuvers. The analysis is carried out with the vehicle speed as reference variable (x-axis) in order to correlate specific events to the buses' driving speed.

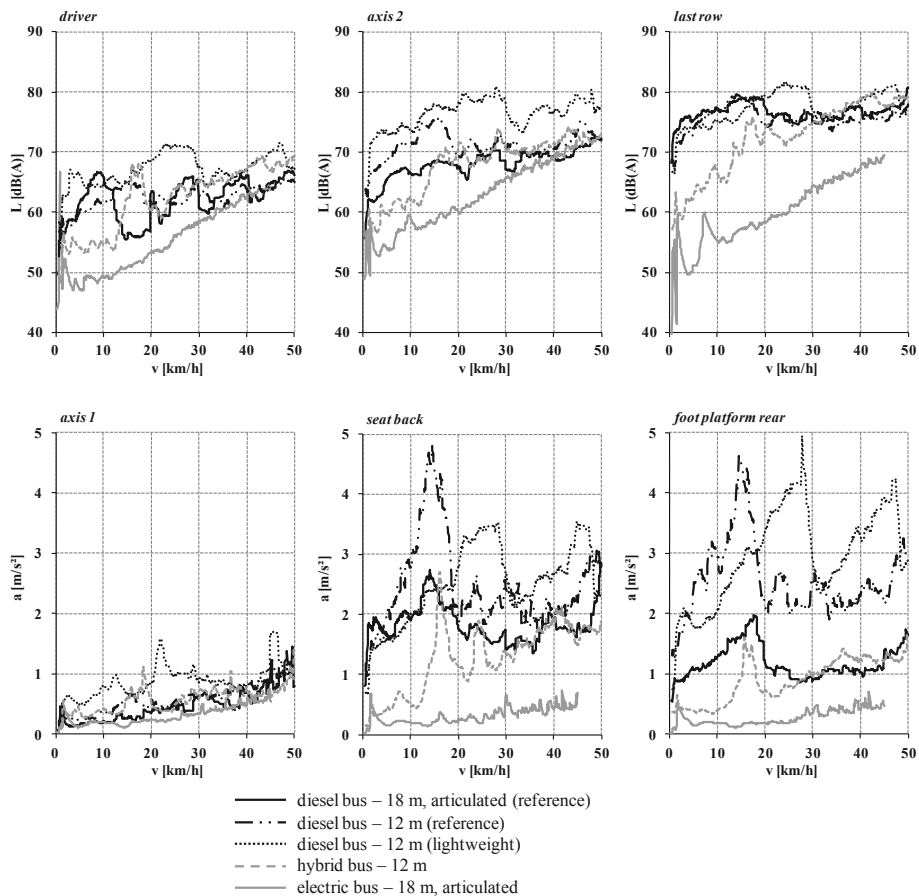


Fig. 7-F. Interior noise and vibrations at full load acceleration

As in the evaluation of the constant speed tests, a general tendency of decreasing sound pressure levels can be determined from the back of the bus to the front. Regarding the measured accelerations, the highest differences are identified in the back of the buses for the sensor positions seat and foot platform. The powertrain concept has almost no influence on the vibrations in the area of the first axis and all bus concepts are in a similar range regarding the vibration amplitude.

Compared to the other buses, the articulated electric bus shows slightly increased noise emissions in the area of the second axis and is therefore a little exceptional. This effect is caused by the layout of the powertrain, since this bus is powered by electric machines on both the second axis in front of the articulation and third axis behind the articulation. Due to the distance to the active components of the powertrain, in the last row of the tested buses the lowest sound pressure levels are measured by far in the articulated electric bus.

The conventional buses have similar noise emissions in the last row near the diesel engine. At first, the sound pressure level increases with the vehicle speed up until the first gear shift. After the shift, the diesel engine is operated in a lower rotational speed, which reduces the sound pressure level, as well. It is striking that the first gear shift of the lightweight bus is set to a higher vehicle speed of approx. 30 km/h. Thus, the diesel engine of this bus remains longer in the area of high rotational speeds and in-between 20 and 30 km/h highest values regarding noise and vibration are determined on all measuring positions for this bus.

While the noise emissions of these buses are very similar in the last row, the lightweight bus stands out with the highest noise emissions on the second axis and the driver's position. Following on from the results of the exterior noise measurements it can be assumed that the lightweight structure has a negative effect on the damping characteristics of structural vibrations, which in this case leads to increased noise levels both in the in- and outside of the vehicle. On the other hand, reduced fuel consumptions in a range from 8 to 14 % have been measured during realistic line operations in the city of Aachen. With an empty weight of 9.2 t, a weight reduction of approx. 2 t against comparable 12 m buses and a positive effect on the efficiency have been achieved. Furthermore, it should be mentioned that due to the structural changes of the lightweight concept the admissible total weight has been reduced, as well. With a vehicle payload of 5.7 t, fewer loads can be applied to this bus which has an influence on the number of transportable passengers. Overall, this leads to a conflict of aims between pollutant emissions and noise emissions. Improving the carbon gas emissions results in higher noise emissions and reduced driving comfort.

In comparison to this, it is interesting to note that up to 30 km/h the measured hybrid bus shows low noise emissions even though the diesel engine is activated during the full load acceleration. Taking the topology of the powertrain into account, this effect can be explained. Due to the serial structure of this hybrid vehicle the diesel engine is only used for the generation of electrical power and the operational point of the engine is therefore not directly linked to the actual vehicle speed. This allows an operation of the diesel engine in optimized rotational speeds regarding efficiency and noise emissions. However, in the speed range of 15 km/h discontinuities and a distinct increase in noise and vibrations can be observed. At this driving speed, the resonance

effect caused by the components of the electric powertrain occurs which has been previously mentioned in the analysis of the exterior noise. Since this resonance effect leads to high amplitudes both in the exterior and interior noise measurements, it is recommended to focus this topic for further developments of this bus concept.

For the analysis of the interior noise it can be noted that in case of the electric bus the noise immission on passengers sitting in the middle and rear of the bus can be reduced by up to 20 dB over a wide range of vehicle speed. In combination with low vibration excitation of the passenger compartment, the best driving comfort will be perceived in this bus concept. This conclusion has also been confirmed with a survey in which the passengers have been asked to rate different aspects of driving comfort in this specific bus.

But not only will the passengers benefit from the reduced noise emission. At the driver's position differences of 5 to 15 dB in-between the tested bus concepts can be observed. This leads to a better driving comfort and also improves the working environment of the driver. After all, excessive noise exposure can lead to health risks and decreases the attention [12].

3F.6 Conclusion

Buses with an electric powertrain offer promising results for improving energy efficiency as well as noise and pollutant emissions in the area of public transportation. In order to evaluate the noise emissions of different bus concepts, a measuring procedure has been established to characterize the buses' exterior noise and NVH behaviour in the vehicle interior.

Regarding the exterior noise, the analysis of the experimental data has shown that electrically propelled buses offer significant benefits in terms of reducing noise emissions in the low speed area up to 15 km/h. At higher vehicle speeds the tire-/road and wind noise represent the major noise source and the buses' powertrain concept has almost no significant influence on the radiated noise. In previous studies it has been shown that frequent stops at bus stations and traffic lights plus traffic jams result in low average speeds considering urban bus routes. Comparing the average speed of the buses with the results from the noise measurements leads to the conclusion that an increased number of electric buses will have a noteworthy impact on the urban soundscape.

Also in the resulting interior noise and vibrations significant differences can be determined between the bus concepts. Due to the removed diesel engine, highest reductions have been measured in the rear of the electric bus. The sound pressure level is in average reduced by 14 dB and considering the maximum difference by 20 dB. This objective measured improvement is reflected in a survey, which has been conducted in addition to the measurements and shall not be discussed in detail in this article. As an essential result it can be stated that a high percentage of passengers (80 %) have rated the bus ride as more comfortable compared to a conventional diesel bus.

Overall, a variety of technologies has been introduced into the daily line operation of public transportation in order to solve the climate and noise issues over the last years.

On the one hand, buses with lightweight structures represent one solution for reducing the energy demand and therefore the fuel consumption when operated by a diesel engine. Compared to conventional diesel buses, this benefit is accompanied by a deterioration of the NVH characteristics. On the other hand, electrified powertrains like in diesel-electric hybrid, fuel cell or all-electric buses show highest reduction possibilities regarding noise emissions both on the out- and inside of the vehicle. However, for a complete changeover of the Municipal Transport Services' fleet further developments have to be made regarding the reduction of acquisition costs, technical reliability and the range of all-electric buses.

Acknowledgement

The research project CIVITAS DYN@MO has been funded through the EC's Seventh Framework Programme for Research and Technological Development.

3F.7 References

- [1] Pless, H., Maßnahmen gegen Verkehrslärm – Politische Handlungsansätze für eine leise Zukunft, Verkehrsclub Deutschland (VCD), Broschüre, 2003
- [2] Biermann, J. W., Vehicle Acoustics – Lecture Notes, Institute for Automotive Engineering (ika), RWTH Aachen University, 2010
- [3] European Parliament, Directive 2002/49/EC of the European Parliament and of the council of 25 June 2002 relating to the assessment and management of environmental noise, 2002
- [4] Ministerium für Umweltschutz NRW, Lärmschutz in Nordrhein-Westfalen – Lärmkartierung und Aktionsplanung nach der EU-Umgebungsrichtlinie, Domröse Druck GmbH, 2008
- [5] CIVITAS DYN@MO, <http://www.civitas.eu/content/dynmo>, 2015
- [6] Ruschmeyer, S., Untersuchung zum Akustik- und Schwingungsverhalten eines Linienbusses mit Hybridantrieb, Institute for Automotive Engineering (ika), RWTH Aachen University, 2012
- [7] Vom Hybrid- zum Elektrobus, www.aseag.de, 2015
- [8] Measurement of noise emitted by accelerating road vehicles, ISO 362-1:2015
- [9] Homann, J., Geulen, G., Töpler, F., et al., Smart Wheels Electric Bus – A Concept for Electric Mobility in Public Transportation, 20th Aachen Colloquium Automobile and Engine Technology, 2011
- [10] Human exposure to mechanical vibrations - Whole-body vibration, VDI 2057 Blatt 1, Düsseldorf, 2002
- [11] Human exposure to mechanical vibrations - Hand-arm vibration, VDI 2057 Blatt 2, Düsseldorf, 2014
- [12] Passchier-Vermeer, W., Passchier, W. F., Noise Exposure and Public Health, Environmental Health Perspectives, Vol 108, Supplement 1, 2000.

Annex 3G

Influence of electric vehicles in noise maps

Hector Campello Vicente¹, Ramon Peral Orts¹ and Nuria Campillo Davo¹

¹Mechanical Engineering and Energy Department, Miguel Hernández University of Elche, Av de la Universidad, S/N - 03202, Elche, Spain, hcampello@umh.es,

Abstract. The electric vehicle is the best positioned alternative to ICE conventional vehicle due to, among other reasons, its friendly environmental properties. One of most significant is its quiet electric engine, which can be a good tool for decreasing noise pollution in cities.

Regarding that, the electric vehicle can be acoustically assessed from different points of view; on one hand, as a moving point source and studying its detectability or annoyances for pedestrians, and, on the other hand, as part of traffic flow in a road and becoming part of a whole noise map. In this Annex it was studied and quantified the effect of introducing a flow of electric vehicles in real urban traffic. For this purpose, it was used experimental procedures to add to the NMPB ROUTES noise prediction model the electric vehicle as a potential noise source in the traffic flow.

3G.A Introduction

Sales of electric (EV) and hybrid electric (HEV) vehicles have been increased in the recent years, becoming more common in urban fleets. The electric technology, in addition to reducing the emission of polluting gases, also impacts on the noise maps of the cities. The absence of mechanical noise is supposed to reduce significantly the noise levels in urban areas, having a positive effect on noise maps.

According with the Directive 2002/49/CE [3], a noise map is a graphic designed for the global assessment of noise exposure in a specific area due to different noise sources or for overall predictions for such an area. EU Member States are required to produce strategic noise maps in their main cities (and other infrastructures and industrial sites). The main target is to make a general diagnosis of noise pollution that can lead to action plans, and a noise management that can be implemented in terms of action plans and acoustical planning. There are several models for making noise maps. Some of them use empirical models, based on experimental approaches, but most of the models are based in the physics of propagation of sound outdoors and a theoretical sound power generation model that changes with the characteristics and amount of traffic sources. In any case, the potential presence of electric vehicles is considered.

This contribution presents the assumptions and experimental tests developed to integrate the EV as a noise source in a traffic noise prediction model, as well as the expected effect of those vehicles in a noise map under different traffic conditions.

3G.2 Methodology. New model and influence of warning sounds

To be able to develop computational noise maps, it is necessary to use a prediction model that simulates the real conditions of the area of study. With this purpose and considering the recommendation of the European Directive, the French official noise prediction model, NMPB ROUTES has been used to evaluate noise levels in function of traffic flow conditions.

French model needs different inputs to develop the simulation, main of them are:

- Flow of light vehicles per hour (weight<3.500kg)
- Flow of heavy vehicles per hour (weight>3.500kg)
- Speed of both type of vehicles
- Boundary conditions

After introducing the parameters in the model, it provides the sound pressure level (dB(A)/hour) along the area of simulation, taken into account reflections and the effect of elements as barriers, buildings or green areas.

In order to introduce the electric vehicles in the noise prediction model, it is necessary to know the sound power level emitted by an electric vehicle, and develop an algorithm to models the sound level depending on the source's velocity.

The modelling process was carried out based on an initial assumption "The acoustic behaviour of an electric vehicle could be assumed as a conventional ICE vehicle without mechanical noise", underpinned by some experimental measures of several ICE and E vehicles under coast-by and pass-by conditions [4], Fig. 1-Ga and 1-Gb.



Fig. 1-Ga. Pass-by test of an Electric Vehicle

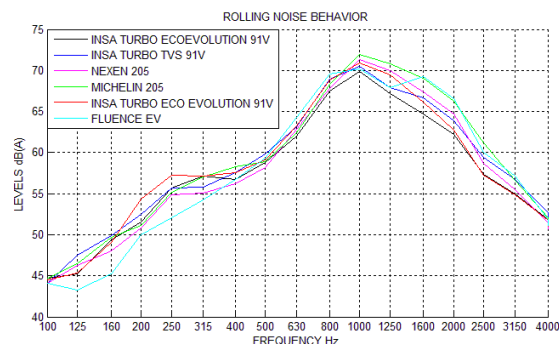


Fig. 1-Gb. Comparison of sound emitted by an electric vehicle vs ICE vehicles tyre/road noise

In order to implement this assumption on the French noise traffic prediction model, it was carefully studied the algorithms to obtain the sound power level of the different noise sources. According with the guidelines of the model, noise radiated by a vehicle is divided in two main independent sources; see Eq. 1-G and Fig 2-G:

- The Engine and other mechanical sources
- Tyre/road source, rolling noise (aerodynamic sound is considerate like part of this source)

$$L_A(V, R, p, a) = L_{rolling}(V, R) + L_{engine}(V, p, a) \quad \text{Eq. 1-G}$$

Where:

- L_A is Pass-by level of the vehicle [1]
- R is the road platform surface category
- p is the road gradient
- a is the traffic flow type (steady speed, acceleration, deceleration)

Therefore, to be able to model the sound level emitted by the EVs, only tyre/road noise source (rolling noise) has been considered, removing all mechanical noise sources from the algorithm that calculates the power level of an EV. As it is done with the other type of vehicles, the power level of an EV was evaluated in function of traffic speed and added to the general algorithm of the French model, see Eq. 2-G.

$$L_{Awi} = 10 * \log_{10} \left((E_{vl} + 10 * \log_{10} Q_{vl}) + (E_{vh} + 10 * \log_{10} Q_{vp}) + (E_{ve} + 10 * \log_{10} Q_{ve}) \right) \quad \text{Eq. 2-G}$$

Where:

- $E_{v(i)}$ Sound power emitted for each category of vehicle (l – light vehicle, h – heavy vehicle, e – electric vehicle),
- $Q_{v(i)}$ Average flow rate for each category,

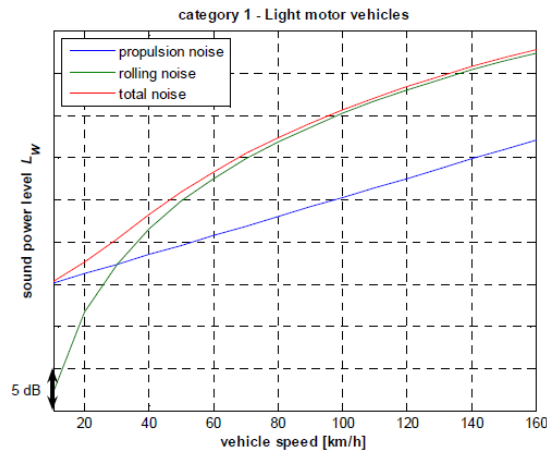


Fig. 2-G. Contribution of different sub-sources to the total sound emitted by a vehicle [5]

Once the modifications of the French model were completed, it was able to be used to analyse different traffic conditions adding the EV as a noise source.

Free field traffic lane with electric vehicles

Before developing the general study about the effect of electric vehicles in real noise maps, it was proposed to analyse the noise emitted by a free field traffic line of vehicles and assess the variations on the emitted sound pressure levels by changing the proportion of electric vehicles on the traffic flow.

With this objective, a road with a constant traffic flow of conventional ICE vehicles was implemented, simulated and validated with real traffic noise measurements.

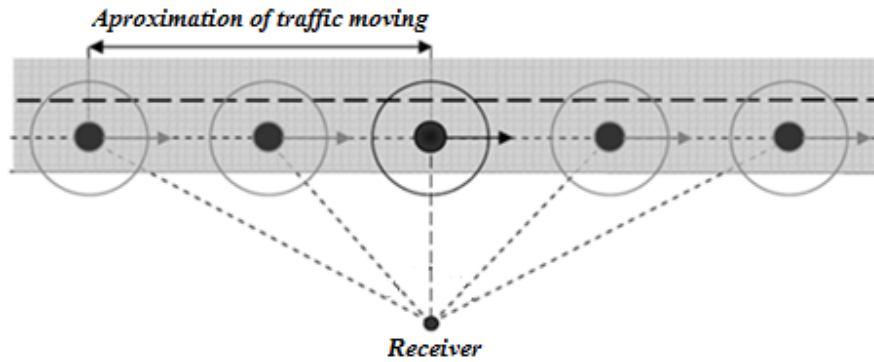


Fig. 3-G. Free field traffic lane

To evaluate the effect of electric vehicles on those conditions, it was varied the proportion of electric vehicles on the total amount of light vehicles, Eq. 3-G, and calculated the sound level emitted by the traffic lane.

$$Q_{\text{light-ICEV}} = Q_{\text{TotalIV}} - Q_{\text{EV}} \quad Q_{\text{eEV}} = N\% \cdot Q_{\text{TotalIV}} \quad \text{Eq. 3-G}$$

Free field traffic lane with AVAS electric vehicles

Considering that there is expected that EV's are provided with Acoustic Vehicle Alerting Systems (AVAS), it was integrated in the model the optimal sound power level of the warning sound, according with previous studies developed at INSA-Lyon [6].

This aspect of the research was developed in collaboration with the Laboratoire Vibrations Acoustique of Insa-Lyon, as a short-term scientific mission (STSM) of the COST action TU 1105 "NVH analysis techniques for design and optimization of hybrid and electric vehicles".

The objective of the collaboration was to evaluate the repercussion of inserting electric vehicles provided with AVA Systems in noise maps. Those AVAS are deemed necessary due to the lack of mechanical sounds of electric vehicles, and it is estimated that increasing the total sound pressure level of an EV in 2 dB at 20 km/h, the detectability will be near to an ICE vehicle [6]. For that simulation, the model was adapted to include the emission of the warning sound by all the electric vehicles, and it was compared the environmental effect of EV's with AVAS against ICE vehicles.

Noise Maps with electric vehicles. Real Case

Finally, it was assessed the variation of sound pressure level in a real noise map after considering electric vehicles running through the streets. Regarding that, the European Directive 2002/49/CE [3] requires that municipalities prepare noise maps whose results reflect the number of inhabitants affected by noise on different ranges of annoyance. That information must be extracted from noise maps, using the maximum façade noise level assigned to all the inhabitants in the building. There are several methods to calculate the number of people exposed to noise in urban areas and, after analysing the different methods studied by Arana [8] or Licitra [9], the study has been developed using the German National Method VBEB [7].

The method VBEB evaluates the noise levels received on the façade of a building by means of a grid of receivers located at different heights on the façade, see Fig. 4-G. Once the levels in the facade have been obtained, the next step is to establish how much inhabitants are in each building, according with their characteristics. For this purpose it was used the Eq. 4-G.

$$EZ_{building} = \frac{G_{building} \cdot GZ_{building} \cdot 0.8}{WE} \quad \text{Eq. 4-G}$$

Where:

- $EZ_{building}$ is the number of Inhabitants.
- $G_{building}$ is the surface of Building.
- $GZ_{building}$ is the total Height.
- WE Square meters allocated per inhabitant on the area.

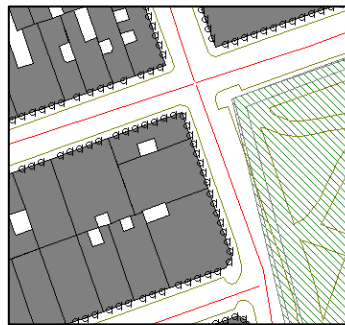


Fig. 4-G. Distribution of receivers along the façade of buildings

On the assessment process two different cases were studied. The first one analysed the current state of traffic flow (no electric vehicles), and the second one took the assumption that all light vehicles were electric vehicles. Both cases have been applied on an urban area of Elche (Spain) whose surface is approximately 450000 m² and 875 buildings of different heights, see fig. 5-G.

The urban noise map was simulated using the commercial software Predictor, adding the sound power levels emitted by the flow of electric vehicles by means of the modification implemented to the French Model by Matlab. Finally, taking into consideration the real traffic on the studied area, it was evaluated the acoustical situation of 12232 inhabitants, by means of 5600 receivers located on the buildings' facades and the receivers located in a grid of 5m x 5m, see fig. 5-G.

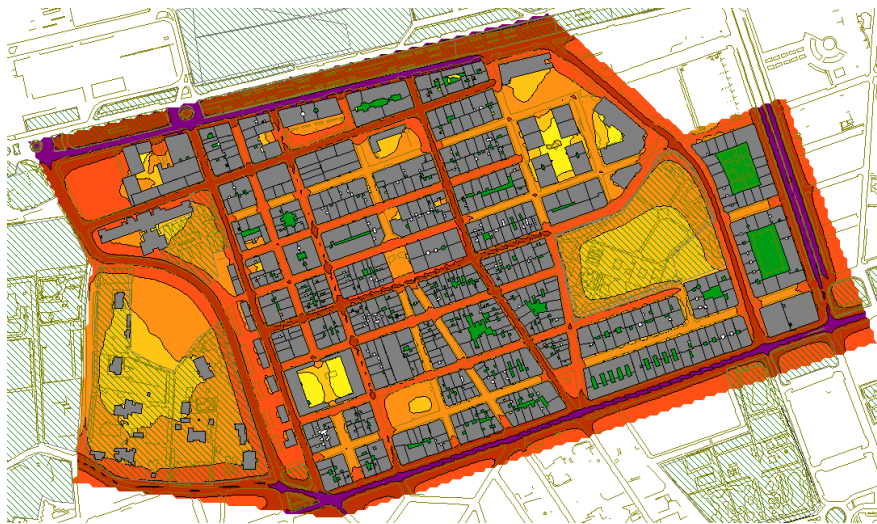


Fig. 5-G. Result of the noise mapping simulation

3G.3 Results

The results shown in this section are the A-weighted sound pressure levels emitted by a traffic flow under different traffic conditions, considering that all calculations were developed according to the conditions assumed by the French Noise Prediction Model NMPB ROUTES:

- Constant speed
- Constant traffic flow
- Favourable environmental conditions (no rain, no wind...)
- Only traffic noise source

Free field traffic lane with electric vehicles

The Fig. 6-G shows the results of the simulation of a free field lane traffic flow, considering two different cases: all vehicles are ICE light vehicles and all vehicles are EV; in both cases, the total flow of vehicles is 1350 units and they are running on the same conditions.

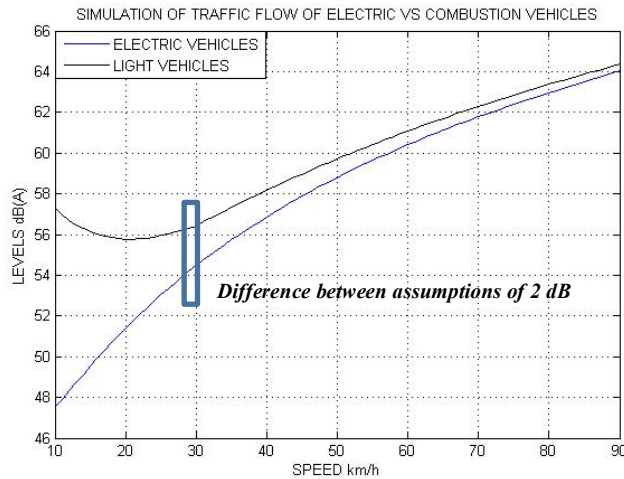


Fig. 6-G. Simulation of traffic flow of Electric vs Combustion vehicles

Focusing the attention on a representative low speed, for example 30km/h [10], the difference between a traffic lane of ICE vehicles and the same one running only EVs is 2 dB. This difference grows quickly if it is evaluated a lower speed traffic (it is not common to simulate a traffic street on a noise map with a velocity lower than 30 km/h) and the difference is approaching to zero with speeds higher than 50 km/h, see Fig. 7-G.

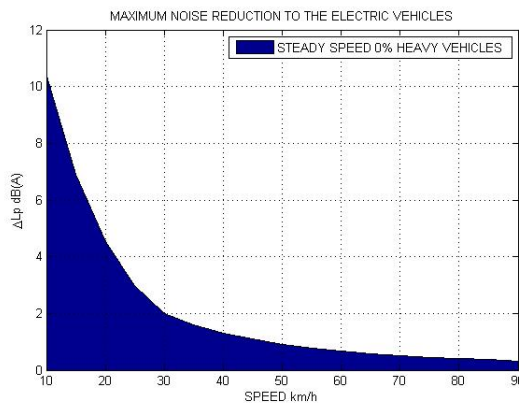


Fig. 7-G. Differences between 100% EV vs 100% ICEV traffic flows, no heavy vehicles

Fig. 7-G shows the difference between a flow of EVs and ICEVs without heavy vehicles running.

That sequence changes when heavy vehicles are considered in the traffic flow. In this case, the heavy traffic was taken into account as a 5% of the total traffic, due to the French Model recommends a maximum of 5% of heavy vehicles in urban areas, see Fig. 8-G. Once the heavy vehicles were introduced in the traffic flow, the decrease generated for electric vehicles is lower than 2dB(A) in any case, and at 30km/h it is of 1,2 dB(A).

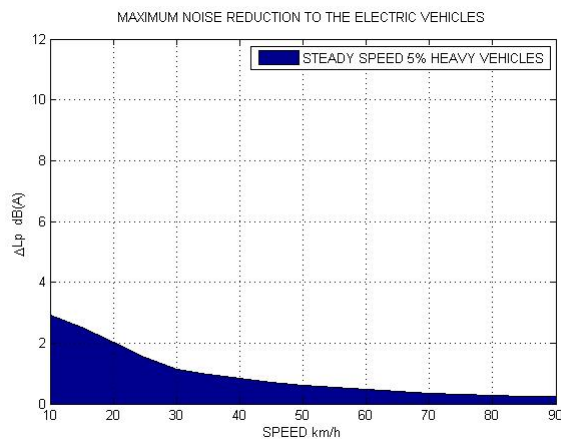


Fig. 8-G. Differences between 100% Light EV vs 100% Light ICEV traffic flows, 5% Heavy vehicles of the total flow

Free field traffic lane with AVAS electric vehicles

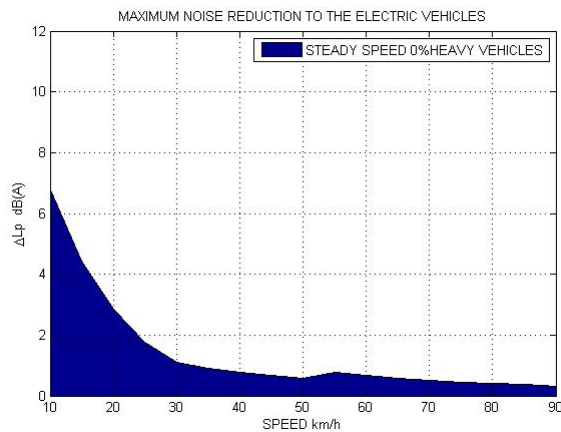


Fig. 9-G. Differences between 100% AVAS-EV vs 100% ICEV traffic flows, no heavy vehicles

As well, it was evaluated the expected effect of introducing warning sounds on electric vehicles. The warning sounds developed at Insa-Lyon were taken into consideration (increasing the level of EV's in 2 dB(A)), getting as a result that the noise emitted by a EV's with AVAS is, in any case, lower than the emitted by ICEVs under same conditions as shown Fig. 9-G.

The repercussion of electric vehicles using warning sounds is lower than electric vehicles without them but they don't exceed levels of combustion vehicles. In this case the decrease is 1 dB(A) approximately if there are not heavy vehicles, and when they are considered in the traffic flow, then the decrease is lower than 0,6 dB(A).

Noise Maps with electric vehicles

Finally, in order to have a real example it was compared the results of a noise map with and without EVs. For this purpose, the map was calculated in accordance with the Spanish legislation [11], that limits to 65dB(A) the maximum sound level permitted to be registered on the façade of a building or receiver.

For developing this part of the study, two complete noise maps of an area of Elche, Spain, were calculated. For the first one it was used only ICEVs and for the second only EVs. In both cases, the traffic flow was extracted from real measurements carried out in the area, where the traffic is composed from light vehicles and heavy vehicles indistinctly. The speed limitation in the area of study was 30km/h.

The comparison of results of these two maps, see Fig. 10-G, shows the number of citizens which improve their acoustical conditions, receiving levels lower than 65 dB(A). The repercussion of using 100% EVs as light vehicles would generate an improvement of 10% of citizens which might be under the limits fixed by the Spanish legislation.

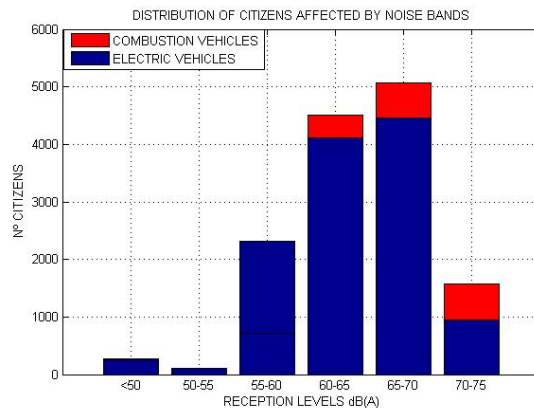


Fig. 10-G. Difference of simulation of traffic flow of Electric vs Combustion vehicles

3G.4 Conclusions

The work presented in this paper describes the expected noise effects of EVs in noise maps by measures and simulation of the noise emitted by an EV. The simulations have been based on a modification on the French Noise Prediction Model NMPB ROUTES and results have been shown for three cases:

- Electric vehicle running in free field traffic lane
- Electric vehicle provided by AVAS running in free field traffic lane
- Electric vehicle running in a real urban area.

The emergence of traffic flow without engine noise should improve the acoustics environmental conditions but it has been checked that in extra-urban speed, up to 50 km/h, the benefits are low or worthless due to the dominant contribution of rolling noise. When a whole flow of EVs running at 30km/h is studied in an free field lane, the estimated reduction of the sound pressure level is 2 dB(A), whether all light vehicles are electrics and heavy vehicles don't appear in the simulation.

On the other hand, if electric vehicles use warning sounds to improve security of pedestrians, the result changes and in this case de reduction is 1 dB(A) without heavy vehicles in the traffic flow.

Finally, a real noise map was simulated to show that the substitution of combustion vehicles for electric vehicles would generate an improvement of 10% of citizens who would improve their acoustic environment, getting it lower than the limit valour of the Spanish legislation.

Acknowledgments

The authors thank the support provided by the Laboratoire Vibrations Acoustique of Insa-Lyon during the STSM mission, under the framework of the COST Action TU1105, of Dr. Campello to Lyon and especially to his hosts Jerome Antoni and Etienne Parizet. Also, the authors acknowledge the financial support from the COST Action TU1105 for the STSM mission of Dr. Campello.

3G.5 References

- [1] Road Noise Prediction 1 - Calculating sound emissions from road traffic Sétra. Service d'études sur les transports, les routes et leurs aménagements, June 2009
- [2] Road Noise Prediction 2 - Noise propagation computation method including meteorological effects (NMPB 2008). Service d'études sur les transports, les routes et leurs aménagements. June 2009
- [3] Directive 2002/49/CE of the European Parliament and Council of 25 June 2002 relating to the assessment and management of environmental noise.

- [4] Campello, H.; Campillo, N.; Peral, R.; Velasco, E. Caracterización sonora experimental de un vehículo eléctrico. XX Congreso Nacional De Ingeniería Mecánica. Malaga 2014.
- [5] Blokland, G.; Peeters B. Modeling the noise emission of road vehicles and results of recent experiments. Internoise 2009. Ottawa (Canada).
- [6] Parizet, E; Ellermeier, W.; Robart, R. Auditory Warnings for Electric Vehicles: Detectability in Normal-Vision and Visually-Impaired Listeners. Applied Acoustics 86(2014) 50-58.
- [7] Vorläufige Berechnungsmethode zur Ermittlung der Belastetenzahlen durch gebungslärm (VBEB): Preliminary calculation method for determining the exposure figures caused by environmental noise. Federal German Gazette of 20th April 2007; p.4, 2007.
- [8] Arana, M., Perez, D., Nagore, I. Using Noise Mapping to Evaluate the Percentage of People Affected by Noise. Acta Acustica 95(2009) 550-554.
- [9] Licitra, G., Ascari, E., Brambilla, G. Comparative analysis of methods to evaluate noise exposure and annoyance of people. 20th International Congress on Acoustics, ICA 2010
- [10] Calvo, J.A., San Román, J.L., Álvarez, C., Quesada, A. Influencia de los Parámetros de Conducción en el Ruido Emitido por un Automóvil en el Tráfico Urbano. XIX Congreso Nacional De Ingeniería Mecánica Castellón 2012.
- [11] Real Decreto 1367/2007, de 19 de octubre, por el que se desarrolla la Ley 37/2003, de 17 de noviembre, del Ruido, en lo referente a zonificación acústica, objetivos de calidad y emisiones acústicas.

Annex 3H

An innovative noise measurement method using OBSIe

Adam Zofka¹, Maciej Maliszewski¹ and Ewa Zofka¹

¹Road and Bridge Research Institute (IBDiM), Poland, Instytutowa 1, 03-302 Warsaw, azofka@ibdim.edu.pl, mmaliszewski2@ibdim.edu.pl, ezofka@ibdim.edu.pl,

Abstract. The purpose of this chapter is to present an innovative method of measuring sound intensity called On-Board Sound Intensity on electric (EV) or hybrid electric vehicle (OBSIe). Typical sources of noise emitted by modern vehicles in urban areas are propulsion noise and noise generated at the tyre/pavement interface. Thinking of a future we can imagine cities full of silent, zero-emission cars. Propulsion noise becomes insignificant while tyre/pavement contact noise can still dominate in the urban, low-speed areas. Current methods of pavement noise measurements are not suited for the application in such scenarios and only partially eliminate the propulsion noise. Thus there is a need for research methods that can assess tyre/pavement noise at speeds lower than 50 km/h which is a threshold between propulsion noise and tyre/pavement noise. Our method developed at Road and Bridge Research Institute (IBDiM) in Poland is especially well suited to measure noise intensity in densely populated urban areas where vehicle transport generated noise is problematic. High manoeuvrability of a testing vehicle, quick installation and low cost are only some of the benefits of the OBSIe.

3H.1 Introduction to pavement noise

Mechanisms of noise generation

Sound is a rapid change of pressure (vibration) of air or water or another medium, which carries the sound. Sound propagates in the medium from its source, while the medium involves a damping effect and drops the sound level from maximum to total silence within a particular distance. It is characterized by frequency and energy of medium vibration and it can rise from many different sources. Human perception of sound is possible thanks to ears. When a sound occurs it involves an acoustic pressure onto eardrums and hearing apparatus which are interpreted by human brain as sound.

As mentioned above, sound can be characterized by different frequency (or wavelength) and level (pressure). Human can experience sound pressure as low as 0,00002 Pa (hearing threshold) or higher than 100 Pa. Observations made on human hearing proved that change from sound pressure from for instance 0,02 Pa to 2 Pa (increase of 0,18 Pa) is perceived as same as change from 0,5 to 5 Pa (increase of 0,45 Pa). According to these observations it was assumed that human hearing perception can be described using Eq.1 below [2].

$$\text{Sound level [dB]} = 20 \times \log \left(\frac{\text{Sound pressure [Pa]}}{\text{Hearing threshold pressure [Pa]}} \right) \quad \text{Eq. 1-H}$$

Noise is characterised as mix of different sound types, which is perceived as being unpleasant for human or in some cases can be harmful to physical conditions and health.

Sources of noise generation

Traffic noise is understood as a sound generated by passing cars, trucks, vehicles, planes, vessels, etc. The vehicle noise can be generated by different sources, like propulsion noise, transmission noise, aerodynamic resistance noise and tyre pavement interaction. In conventional, internal combustion engine cars (ICE) most of the movement noise to a certain speed, known as crossover speed, is generated by propulsion, while above this speed tire/pavement contact noise plays significant role in the overall vehicle generated noise. In summary, before reaching the crossover speed one can hear the car engine or exhaust system noise as dominant, while after exceeding this speed, one can hear the tire/pavement noise above other sources of noise. The crossover speed for passenger cars varies from 16 to 40 km/h and for trucks varies from 56 to 80 km/h during cruise speed and grows from 32 to 48 km/h for passenger cars and over 80 km/h for truck during acceleration [2]. In modern hybrid-electric vehicles (HEV), electric vehicles (EV) or latest fuel-cell electric vehicles (FCEV) the propulsion and transmission noise becomes insignificant, so tire-pavement interaction noise becomes dominant regardless the vehicle speed. It can be assumed that crossover speed is close to 0 km/h in this type of vehicle.

Influencing factors

Noise as already mentioned is a batch of different sounds with regards to soundwave length or frequency and sound level. The propagation of noise and its perception by humans is affected by different environmental factors including temperature, air pressure and humidity. Other factors such as obstacles, barriers or their surface type also play significant role. Different noise sources are even likely to decrease the overall noise perception, by interfering with each other destructively, resulting in the noise cancellation effect.

Researchers found several mechanisms of noise generation and amplification for pavement noise originating from tyres. This particular type of noise might be generated by:

- radial vibrations of tyre tread,
- air compressing and decompressing during wheel pass,
- tread tangential motion (called “stick-slip”)
- breaking of adhesion of tread rubber to the pavement (called “stick-snap”).

Amplification mechanisms are responsible for noise emphasis and cannot be omitted in overall tyre/pavement noise generation analysis. The following amplification mechanisms can be mentioned:

- horn amplification effect,
- radiation of resonant air (Helmholtz resonance),
- pipe resonances in channels formed in the tire footprint,
- tyre sidewall vibrations,
- cavity resonance in tyre tube.

All those factors result in the overall final noise during vehicle pass-by. It is difficult to isolate these factors from each other, but there exist methods for objective noise measurement.

3H.2 Methods of noise measurement

General

Human beings hear and perceive noise in different and subjective way. Various noise characteristics can be felt differently by observers thus there was a need to work out standardized test methods. The goal of these test methods is to measure traffic noise in unified and objective way using standardized measurement device. Two main types of noise level measuring methods can be distinguished, one by source and the other by overall noise. Following methods are currently used to evaluate traffic noise:

- SPB – Statistical Pass-By (overall noise method) – this method utilizes set of microphones located in a certain distance to evaluated road and vehicles; microphones register the overall noise generated by randomly passing vehicle, while the observer measures its actual speed; in this method the registered noise consist of the summary of noise generated by all mentioned noise sources or amplification methods [1]. Different vehicles and different pavement types can be observed in this method; special circumstances (distance to obstacles) should be ensured to conduct proper measurements;
- CPB – Controlled Pass-By (overall noise method) – similar to SPB method, with the difference that passing vehicles are instructed to pass with the setup measurement speed; also particular vehicle types or pavements can be chosen for evaluation;
- CPX – Close Proximity method (by source method) – method of evaluation of the tyre / pavement noise; this is a trailer method, where the set of microphones are mounted on a single wheeled trailer, attached to a measurement car; the trailer is designed with a special sound insulated cover which decreases bounced sounds and is generally designed to measure pure noise emission generated by the tyre and pavement interaction; different tyres or pavement types can be used for evaluation; this method is more popular in Europe;
- OBSI – On-Board Sound Intensity method (by source method) – this method is similar to CPX method but there is no need of using special trailer; the

pair of synchronised sound intensity probes is attached directly to the car wheel; measurement takes place during the car movement; no special sound insulation is used, so measurement can be affected by other vehicles, obstacles in close surrounding or noise generated by testing vehicle itself; to measure the tyre / pavement interaction noise, the crossover speed should be carefully controlled during testing; this method is more popular in the USA [1];

- OBSI_e - On-Board Sound Intensity on electric (EV) or hybrid electric (HEV) car (by source method) – this method is an evolution of OBSI method, so it does not utilize special trailer; the pair of synchronised sound intensity probes is attached directly to the electric car wheel; measurement takes place during the car movement; no special sound insulation is used, so measurement can be affected by other vehicles, obstacles in close surrounding but noise generated by testing vehicle itself can be omitted or treated as unimportant; tyre / pavement interaction noise can be measured from as low speeds as 10 km/h, thanks to that crossover speed in this case is very low; this method was for the first time presented by IBDiM in Poland;

OBSI_e (On Board Sound Intensity on electric car)

OBSI_e noise measurement method is an easy and robust method and could be treated as an alternative to CPX method. This method is meant for conducting measurement at any speed but it is especially recommended for use in urban or low-speed areas, where the trailer methods would be inconvenient or even impossible to use. OBSI_e method gives opportunity to be used in such scenarios as on historic pavements made of stone paving brick, concrete paving brick and other types of wearing courses, for example to decrease its noisiness by a paving technique or maintenance technology. It could also help to evaluate methods or technology of increasing noisiness of EH's, HEV's or FCEV's - for example with special tyre technology or additional equipment installed on-board.

The OBSI_e method comprises the following elements:

- Two pairs of sound intensity probes with wheel hub mounting assembly (Fig.1-H),
- Digital/Analog Converter,
- PC computer with registration and interpretation software,
- Wiring.

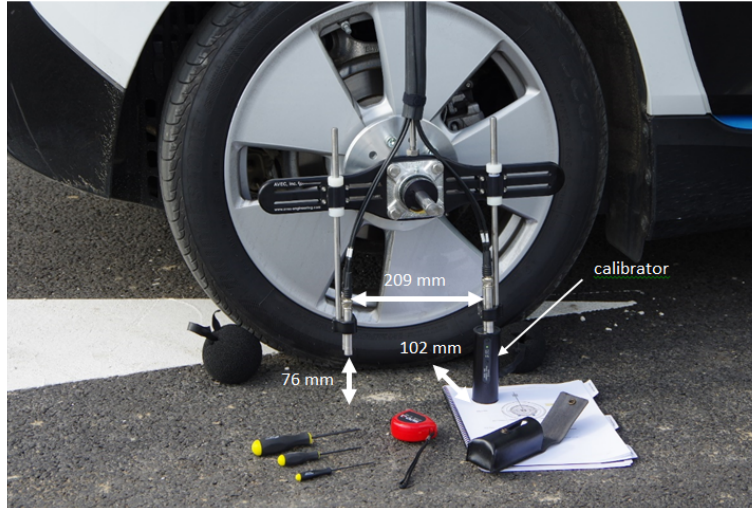


Fig. 1-H. Sound intensity probes mounted on wheel hub; calibration process in progress

The measuring set is mounted onto an EV, HEV or FCEV, of which the plug-in HEV (PHEV) type would be most convenient or practical. Since EV only vehicle has limited range to ca. 120 km in order to perform measurements as long as possible it needs to be transported by a car carrier. HEV's or PHEV's are able to drive in Pure Electric mode and if it can be activated by the driver, it would be very convenient solution for carrying OBSIe set (Fig. 2-H).



Fig.2-H. OBSIe measurement set installed on EV, BMW i3

The following activities should be performed before each measurement:

- Sound probe calibration,
- Record of tyre rubber hardness, temperature and tyre pressure,
- Record of pavement temperature,
- Record of ambient temperature, humidity and pressure.

Preliminary test results

First tests on the OBSI_e system were conducted on several road test sections. These were asphalt and cement concrete wearing courses paved on roads located in Poland. Following sections were tested:

- SMA 11 at Nowolazurowa Str, Warsaw (road under construction),
- quiet asphalt pavements test road in scope of CIDRO project, located near Bolimow,
- SMA 11 and PCC on S-8 motorway near Mszczonow,
- old and new PCC on S-8 motorway near Polichno,
- new PCC at S-8 motorway crossing with A-1 highway at Rzgow intersection,
- BBTM 8 and SMA 11 with rubber in Pruszkow,
- stone paving brick on Krakowskie Przedmieście Warsaw.

Test results obtained on those test sections are presented in Fig.3-H.

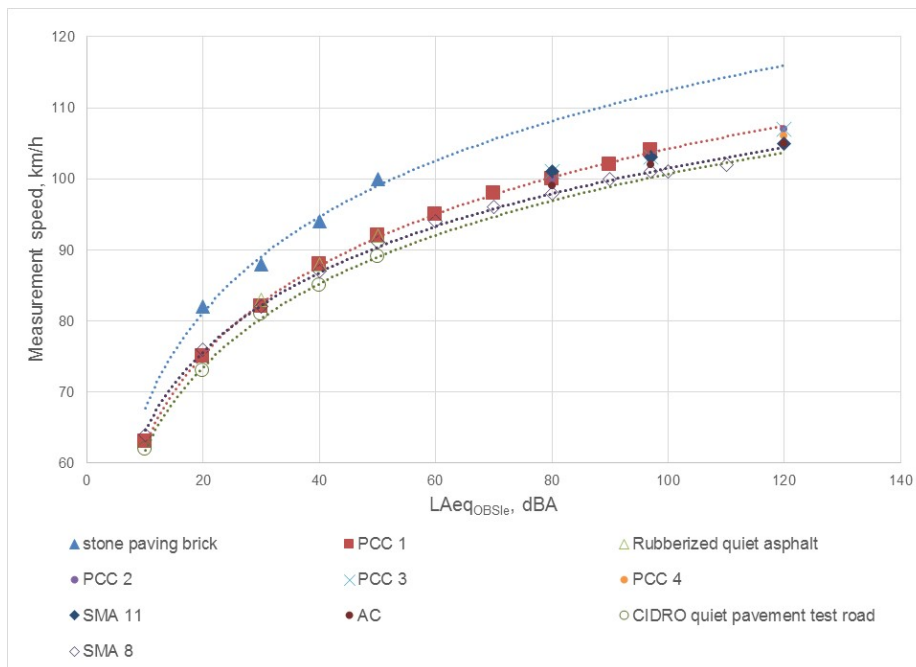


Fig.3-H. Test results from OBSI_e method

The preliminary test results showed that measurements can be conducted at speeds as low as 10 km/h. Unsurprisingly, stone paving brick was the loudest pavement type and generated equivalent noise levels as loud as at 10 or 20 km/h higher speeds for other pavements. This study will be continued in scope of “RID – Noise”, new research project which starts in 2016 and will be conducted and managed by IBDiM (more results will be available during the course of the project).

3H.3 Potential outcome discussion and future development

The OBSIe method gives an opportunity to evaluate some aspects concerned with use of EV, HEV or FCEVs. These are amongst others:

- Tyre / pavement noise generation,
- Tyre construction and thread type,
- Intentionally generated sound signals outside the vehicle,
- Additional equipment helping or preventing

In the future there are extensive plans on performing analysis of not only noise generated outside the vehicle, but also to analyse noise inside the car, as regards different pavement types, different tyres or different measuring conditions. The detailed analysis will also include noise spectrum, which means that different frequencies will be evaluated, not only the equivalent noise level.

3H.4 Computational methods

The p-p measurement principle employs two pressure microphones. The particle velocity component in the direction of the axis of the probe is obtained by a finite-difference approximation to the pressure gradient in Euler’s equation of motion, and the sound pressure is simply the average of the two pressure signals. The most important limitations of this measurement technique are caused by the finite difference approximation, scattering and diffraction, and instrumentation phase mismatch.

The two microphone method principle

The p-p method uses the principle of measuring the pressure gradient by finite difference approximation. Two signals are captured from two microphones separated by a small spacer: one method derives an expression of the intensity in the time domain (analogue intensity measurement) while the other derives an equivalent spectral formula using Fast Fourier Transform analysis (FFT intensity level meter) [3].

As the particle velocity in the acoustic field is not measured directly, the relationship defined by Euler may be employed that states equivalence between the velocity and the pressure gradient under linear and steady state conditions, as depicted in Eq. 2-H:

$$v_r = \frac{-1}{\rho} \int \frac{\partial p}{\partial r} dt \quad \text{Eq. 2-H}$$

The velocity is obtained by integration of the pressure gradient estimated for the acoustic centre of the probe, by taking the difference in pressure from the two readings and dividing by the distance between them. This is referred to as the finite difference approximation of the acoustic velocity, calculated in the direction r , from pressures measured by two microphones separated by a distance Δr , as presented below [2]:

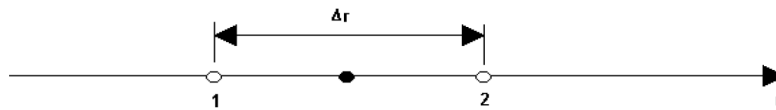


Fig. 4-H. Representation of distance Δr

$$\tilde{v}_r = \frac{-1}{\rho} \int \frac{P_2 - P_1}{\Delta r} dt \quad \text{Eq. 3-H}$$

$$\%p = \frac{P_2 + P_1}{2} \quad \text{Eq. 4-H}$$

The Eq. 4-A is an approximation of the average pressure for the acoustic centre, a point situated between the two microphones. The value approaching the component in the r direction of the acoustic intensity [2] is:

$$\tilde{I}_r = \langle \tilde{p} \cdot \tilde{v}_r \rangle = \frac{1}{2\rho\Delta r} \langle (p_1 + p_2) \int (p_1 - p_2) dt \rangle \quad \text{Eq. 5-H}$$

This formula for acoustic intensity is derived from the sound pressure signals captured from two microphones as a function of time. The schematic representation below in Fig.5-H shows the structure of a measurement instrument that uses analogue electronic circuits [4]:

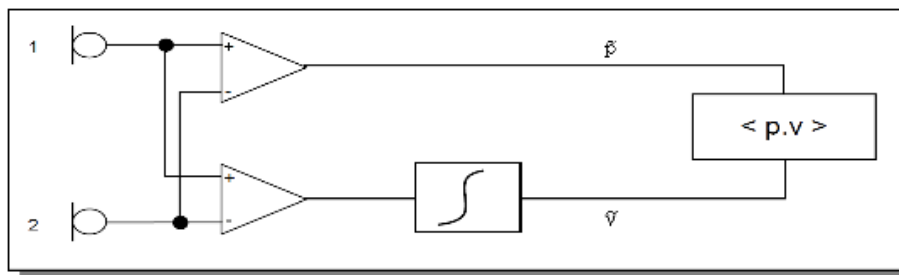


Fig. 5-H. Schematic of the structure of a time based acoustic intensity meter

If some filters (third octave for example) were included in the circuit, one would obtain a spectral analysis of the acoustic intensity. There is another method to bring about a spectral representation of the acoustic intensity: the use of the Fourier Transform [5].

For stationary signals, one notes an equivalent spectral representation according to Eq. 6-H below.

$$I_r = \langle p \cdot v_r \rangle = \int_{-\infty}^{+\infty} I_r(\omega) \frac{d\omega}{2\pi} \quad \text{Eq. 6-H}$$

Where $I_r(\omega)$ is the spectral density of the intensity represented by the real part of the cross spectrum between pressure and velocity (Parseval theory) [6]:

$$I_r(\omega) = \text{Re} \{S_{pv}\} \quad \text{Eq. 7-H}$$

By using Euler's relationship as depicted in Eq. 2-H in terms of the Fourier Transform and approximations for $\frac{\partial p}{\partial r}$ and p , it is possible to reach an expression describing the spectral intensity using the imaginary part of the cross spectra of the pressure signals obtained from the two microphones [6].

$$\tilde{I}_r(\omega) = \frac{1}{\rho \Delta r} \frac{\text{Im}\{S_{21}\}}{\omega} \quad \text{Eq. 8-H}$$

This formula is a significant development in the two-microphone method as it offers a simple measurement system for acoustic intensity using FFT spectra for 2 channels: The principle

is illustrated below in Fig.6-H [4].

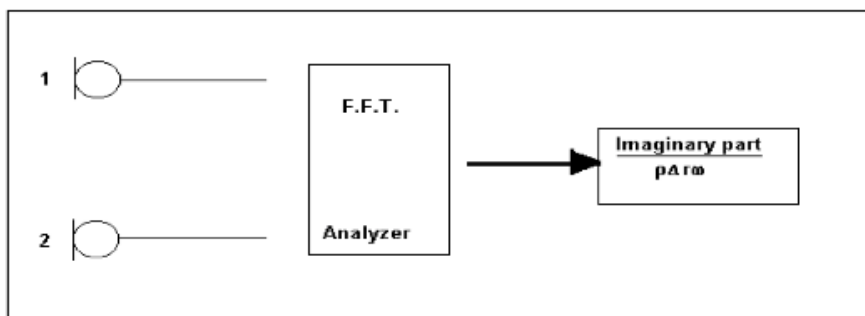


Fig. 6-H. Diagram of an acoustic intensity meter based on FFT analysis

3H.5 Limitations to microphone based intensity meter

i. Systematic errors: finite difference approximation principle

The first source of error is linked directly to the finite difference approximation underlying the measurements. Spatial information is lost as soon as their order of magnitude corresponds to the distance Δr that separates the two microphones. It is an effect known as “instrumental convolution” that amounts to a low frequency limit as it tends the intensity meter range towards the high frequencies [5]. It is represented by the convolution factor, described by the following Eq. 9-H.

$$\delta = \frac{\text{approaching intensity } \bar{I}_r}{\text{real intensity } I_r} \quad \text{Eq. 9-H}$$

For a progressive wave, the fading is greatest when the wave propagates in the direction r according to the alignment of the microphones. Thus it is possible to define an operative frequency limit that tends towards the high frequencies by using the attenuation criteria of 3dB for a plane wave (convolution factor $\delta = 1/2$) [2].

$$\text{Theoretical cut off frequency } F_T = \frac{1.9c}{2\pi\Delta r} \quad \text{Eq. 10-H}$$

The instrumental convolution effect can also create errors when the two-microphones device is too close to a point source. Increasing the distance between point source and microphones quickly reduces the influence of these additional errors. As a precaution it is advisable to have a distance of at least ($\approx 5\Delta r$) between the point of measurement and local noise sources [7].

ii. Systematic errors: microphone transducers

The second source of error is due to the microphone transducers that cause interactive disturbances in the pressure field. The effects of diffraction may be observed whose severity depends on the size and geometry of the microphones. If diffraction effects are on a small scale compared to the distance Δr (for example, 1/8- inch microphones for a distance Δr in the order of cm) the perturbations are barely perceptible.

If this condition is not satisfied (for example 1/2 inch microphones for $\Delta r = 1$ cm) the arrangement of the microphones is more serious [7].

iii. Systematic errors: distortions of measuring instruments

Thirdly, the disturbance caused by the measurement apparatus may introduce significant errors to the intensity calculation even if the apparatus meets current Standard requirements.

In particular the relative phase difference between measurement channels is the most important factor in determining the accuracy of the results [2].

3H.6 Challenge and future work

Our future plans are to focus on the advanced interpretation of the sound spectra recorded and processed by the p-p probe method (i.e. OBSI and OBSIe). Particular interest is to identify and quantify the influence of different pavement features (e.g. micro- and macro-texture, pavement surface type, pavement temperature, surface porosity and stiffness) on different regions of the sound spectra.

3H.7 References

- [1] Jacobsen, F., de Bree, H-E. A comparison of two different sound intensity measurement principles. Acoustical Society of America. Journal 118-3 (2005) 1510-1517.
- [2] Rasmussen, R., Bernhard, R., Sandberg, U., Mun, E. FHWA. (2007). The Little Book of Quieter Pavements, FHWA-IF-08-004, USA.
- [3] Vorlander, M., Auralization: fundamentals of acoustics, modelling, simulation, algorithms and acoustic virtual reality, Dordrecht : Springer, Germany. (2007).
- [4] Jacobsen, F., de Bree, H-E., A comparison of two different sound intensity measurement principles. Acoustical Society of America. Journal, Volume 118, Issue 3, 1510-1517. 10.1121/1.1984860.,USA. (2005).
- [5] Muller, G., Moser, M., Handbook of Engineering Acoustics, ISBN, Munich, Germany. (2013).
- [6] Microsoft. Sound Power Determination According to ISO9614 Standard, Symphonie measurement system – dBFA32 software package Application Notice. (2001).
- [7] Trinth, V., Measurement of Sound Intensity and Sound Power, MRL Technical Report MRL-TR-93-32, DSTO Materials Research Laboratory, Australia. (1993).

Annex 3I

Multi-axial dynamic testing for design/functional/durability testing

Daniele Brandolisio¹, Claus Claeys², Tommaso Tamarozzi³, Bert Pluymers⁴, Wim Desmet⁵, Paul Sas⁶

¹ Department of Mechanical Engineering, KU Leuven, Celestijnenlaan 300B, 3001 Heverlee (Leuven), Belgium, daniele.brandolisio@kuleuven.be, claus.claeys@kuleuven.be, tommaso.tamarozzi@kuleuven.be, bert.pluymers@kuleuven.be, wim.desmet@kuleuven.be, paul.sas@kuleuven.be,

Abstract. During the design of a new car, vibration tests on a prototype or one of its components, using hydraulic test rigs, are important to adjust comfort and durability properties. To make the vibration tests representative for the further life-time of the vehicle, target signals (accelerations or forces) are recorded during a test drive on a test track. These target signals are reproduced on the test rig and often repeated until failure occurs. The calculation of the control signals for the hydraulic actuators of the vibration test rig, such that the measured signals on the test rig match the target signals, is a multivariable tracking problem. The following text refers to multi-axial dynamic testing of ICE vehicles and components, an activity widely performed at KU Leuven Vehicle Technology Lab. Regarding alternative powered vehicles, such as EV, due to the new powertrain components and a different mass and inertia distribution, the NVH (Noise Vibration and Harshness) behaviour differs quite substantially from the ICE vehicles one. Therefore, an advanced dynamic and NVH testing procedure is needed in order to characterize EV (also at component level), and to steer novel optimal design. Nonetheless, the described test rig and testing methodologies represent a valid base for EV dynamic testing, and the integration with tailored approaches will be able to fulfill the experimental requirements.

3I.1 Introduction

Vibration testing, whether employing a sinusoidal input, random input or replication of a deterministic waveform has proven to be a critical step in the successful development of new equipment. Traditionally, vibration tests have been conducted by sequentially applying uniaxial excitation to test articles along three orthogonal axes, using a linear shaker and rotating the test load after each test.

The major shortcoming is that sequential uniaxial excitation may not excite all the critical modes of the test object concurrently and therefore may fail to detect defective design. Although the vast majority of vibration testing uses a single vibration exciter, some conditions exist where a single shaker is not appropriate for the task at hand. Examples of this include:

- Design and Qualification testing of products where a single attachment point might damage the test article when applying the needed force to achieve the desired test levels.
- Testing of objects where the physical configuration of the unit under test would require the design and fabrication of a prohibitively expensive fixture.
- Testing of massive objects where the required force is greater than that available from a single shaker.
- System identification or Characterization in which several waveforms in different direction are necessary to obtain a proper model.

It has been shown that tri-axial excitation can cause approximately twice the fatigue damage as similar test levels and duration in single axis testing. In addition, the order in which uniaxial vibration is applied during a test can cause a significant variance in time-to-failure.

While these results do not confirm a serious lack in uniaxial testing procedures, they represent an important step in the rigorous investigation of differences between the results obtained with multi-axial and uniaxial methodologies.

It is accepted that multi-axial testing excites all modes of the test object and induces a more realistic vibrational stress-loading condition. Properly applied, it can produce a more rapid accumulation of stress and can consequently reduce the time to produce failure.

The CUBE

KU Leuven Vehicle Technology Lab is equipped with the CUBE (Fig. 1-I), a high-frequency 6 DOF shaker table from Team Corporation which belongs to the category of multi-axial shaker tables. It is capable of reproducing real-world vibration conditions by using translations along the x, y and z axes as well as rotations around these axes. The shaker operates at frequencies up to 300 Hz in closed loop (i.e. position control), with a maximum stroke of 101.6 mm in the vertical direction and of 50.8 mm in the longitudinal and transversal. It is capable of reproducing up to 10 g acceleration but its use is normally restricted to 6.8 g. The dynamic force rates at 82 kN and the maximum payload is around 450 kg from specifications. The CUBE is quite revolutionary by its fully integrated concept. In contrast with a conventional hydraulic test system, the six integrated actuators are located on the inside. Fig. 2-I shows on the left the inside arrangement and numbering of the actuators, on the right a look-through scale model on the foreground and the actual shaker in the background. The red arrows indicate the mapping of the actuators between the inside schematic and the scale model. Each orthogonal direction (X-Y-Z) has two actuators in a parallel configuration, further referenced as an actuator pair. Each single actuator consists of two hydraulic pistons, with the high performance two-stage servo valves located in between. Each piston is used for a single direction of motion, with the magnesium outer shell connecting the pistons, such that they move as one entity and thus closing the kinematical chain. Hydrostatic bearings are used for the piston and

the piston head, resulting in almost frictionless operation. An LVDT position sensor is attached to one of the piston heads of each actuator. Locating the hydraulic valves in between both pistons reduces the hydraulic path to a strict minimum and thus increases the bandwidth of the shaker system. The six degrees of freedom are realized by jointly or oppositely driving the three actuator pairs. There is one pair for each orthogonal direction, with two degrees of freedom, one translation and one rotation, for each pair.



Fig. 1-I. The CUBE setup

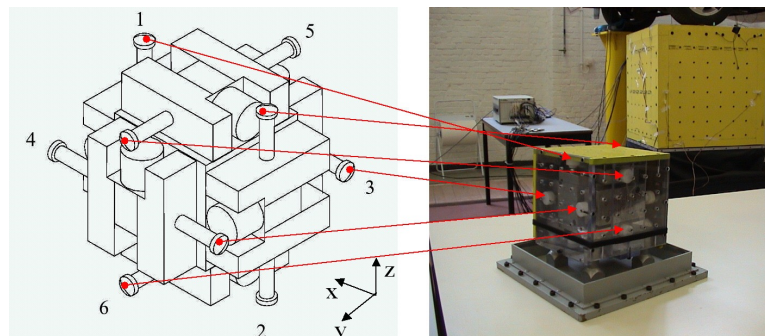


Fig. 2-I. Internal arrangement of the CUBE

Testing possibilities

The purpose of this test rig can be very broad. Particularly the KU Leuven CUBE is mainly used for:

- Single DOF shock and vibration testing.
- Multi DOF random vibration control and road reproduction: road load data, which has significant frequency content over 100 Hz, can be accurately replicated in all 6 DOF. The servohydraulic actuators, fully enclosed within the CUBE, minimize the amplitude of noise contributed by the test system.

- Full Vehicle testing under quasi-operational loading condition.
- Highly dynamic multi-axial testing of vehicle components.
- Accelerated life-time prediction and durability testing of different components: the CUBE is used to assess the durability of a wide variety of components and subassemblies. Test methods are usually based on simulation of multi-axis service conditions where maintenance of phase between the axes is important. However, the unique kinematics of the CUBE design offers the ability to employ combinations of single axis motions where preservation of multi-axial phasing is not a consideration. Cycle or block cycle loading can be used where accelerated tests of simple components need to be accomplished.
- Structure-born road noise investigation: the system can replicate the excitation environment as measured in the vehicle at emitted noise levels that permit the identification and localization of any sound attributable to vibration. Low-level excitation is generally found in the passenger compartment of a typical automobile; the CUBE is an ideal multi-axis test solution capable of reproducing these levels without creating an unacceptably high background level of noise.
- System identification of nonlinear components.

Besides these proven methods, robust for industrial testing, novel research is in progress using the CUBE for subcomponent testing of larger systems with complex dynamics. Here the aim is to employ the CUBE to mimic impedance of the larger structure, making possible to test the subcomponent (i.e. a vehicle suspension) in operating conditions thanks to the multi-axial excitation capabilities.

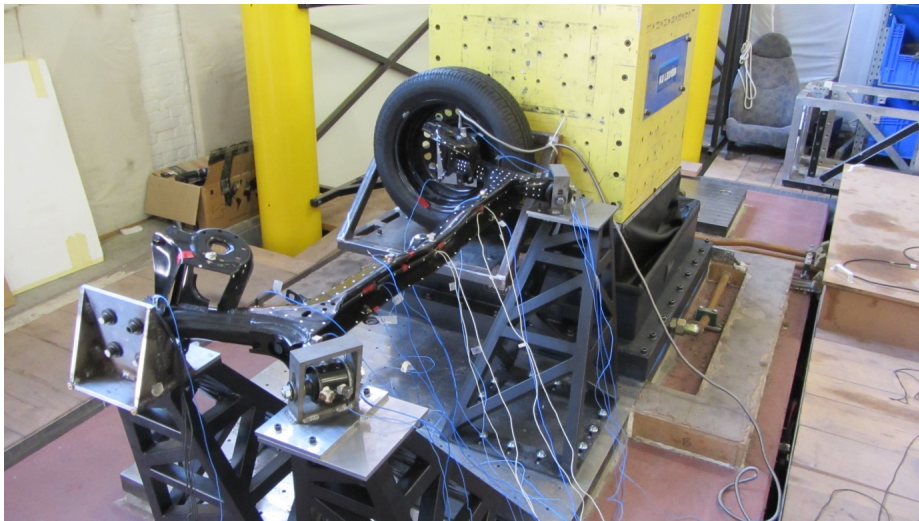


Fig. 3-I. Example of vehicle component testing

3I.2 Examples of multi-axial dynamic testing

Measurement of the tire dynamic stiffness [1]

While driving, the road surface texture excites the tire at the contact patch, resulting in dynamic excitation forces at the vehicle spindle. These excitations cause noise and vibrations in the vehicle interior. The tire dynamic transfer stiffness describes how a displacement enforced at the tire contact patch results in a force at the spindle-wheel interface. Therefore, the tire dynamic transfer stiffness provides insight in the generation of vehicle interior tire/road noise and vibrations.

It is known that the tire dynamic properties depend on the vibration amplitude. The excitation levels during tire dynamic characterization tests should therefore be similar to the excitation levels during operation of the tire. With the developed test setup, which makes use of the CUBE high-frequency 6-DOF hydraulic shaker table, the tire dynamic transfer stiffness can be determined at operational excitation levels in the frequency range 20-235 Hz (see Fig. 4-I).

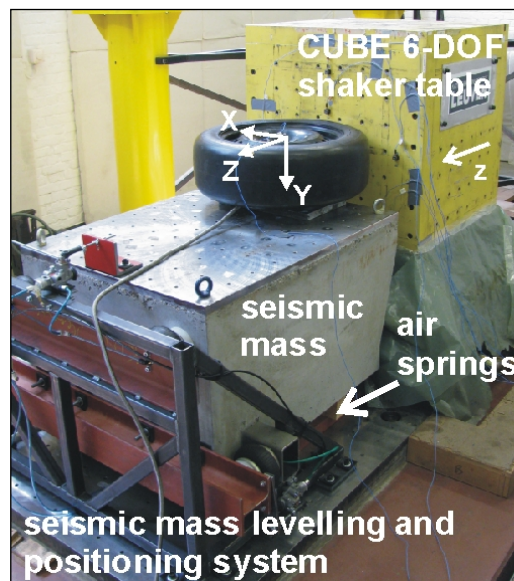


Fig. 4-I. Tire dynamic stiffness measurement

Non-linear MDOF vehicle suspension testing [2]

The CUBE shaker table is also used for non-linear MDOF vehicle suspension testing. In addition to this state of the art shaker, a contactless high accuracy 6-DOF displacement measuring system is used, with up to four independent bodies monitored in the frequency range of interest. Classic acceleration and 6-DOF input force

measurements complete the test setup. MDOF road excitations are recorded on a test track. These signals are then used as target signals for road reproduction experiments on the shaker table. Time Waveform Replication software is used to accurately reproduce the target signals.

a) 6-DOF force and displacement measurements

Measurement of the input forces is done using a force cell (Fig. 5-I) at the tire patch. This force cell allows calculation of 6-DOF forces and moments out of 8 piezo-electric measuring elements, using the appropriate transformation formulas. An important issue for the force cell measurements is the resonant frequency of the cell top platform, for every DOF. The rotation DOFs can be excluded, as the moments of inertia are very low and torque stiffness is high, compared to the dynamic mass and force cell stiffness for the translation resonances. Resonant frequencies are 1.7 kHz (horizontal) and 2.7 kHz (vertical) for an empty force cell. An additional steel plate, enlarging the top surface, is mounted, lowering the resonant frequencies to about 1 kHz (horizontal) and 1.4 kHz (vertical). This approach is neglecting the influence of the tire stiffness on the resonant frequency and is only valid for systems where the ratio between force cell stiffness and tire stiffness is very high. The lowest resonant frequency of approximately 1 kHz allows reliable force measurements up to about 500 Hz. The dynamic mass of the cell top platform should, of course, be compensated for. Measurement of the 6-DOF displacements of the wheel and car body is done using a high accuracy 6-DOF displacement measuring system (Fig. 6-I). This measuring system allows calculation of 6-DOF displacements, for up to four bodies simultaneously, out of LED-position measurements using 3 CCD cameras and triangulation formulas. With this system, simultaneous measurements of tire patch, wheel and car body are possible. From these measurements, using the relative displacements, the compression of tire and suspension system can be calculated. Dynamic measurements are possible even beyond 250Hz for a four independent body configuration. Next to dynamic measurements, the combination of the shaker table, the displacement measurement system and the force cell allows most Kinematics and Compliance (K&C) tests to be performed at the KULeuven Noise and Vibration Laboratory. Fig. 7-I shows displacement curves for wheel motion (blue), car body motion (green) and suspension compression (red). This graph is the result of a “0-to-45-to minus 45-to-0” mm slow vertical displacement of the shaker. The suspension compression is then proportional to the wheel displacement. Fig. 8-I shows a sine sweep signal, starting below the car body bounce frequency, resulting in proportional compression, and ending above this resonance, resulting in full suspension compression. The phase shift from 0° to -180° by passing through the resonance can clearly be identified from the measurements. On the right of this graph the phase shift between wheel (blue) and car body (green) is already at about -90° .

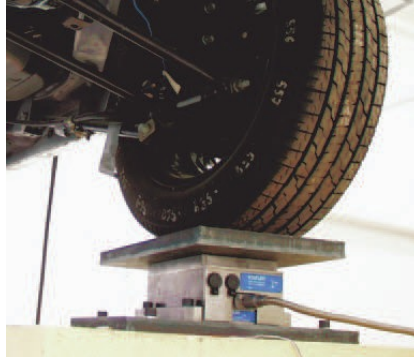


Fig. 5-I. Force cell at tire patch



Fig. 6-I. Displacement measuring system

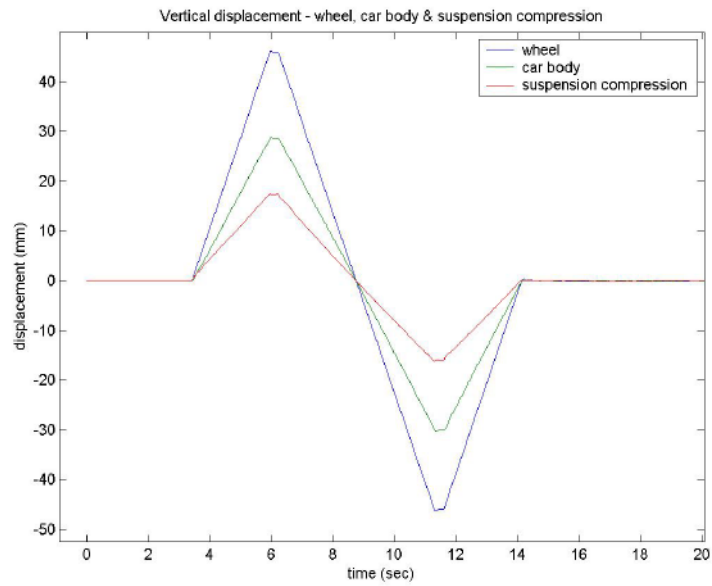


Fig. 7-I. Vertical displacement curve – slow triangular motion

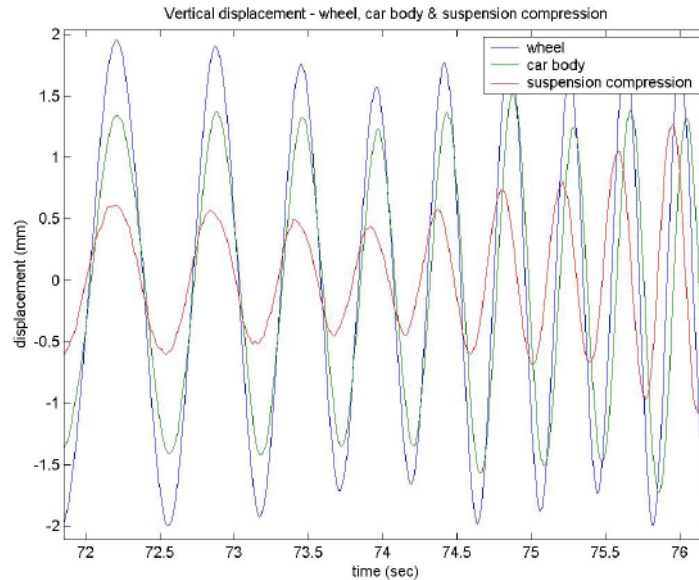


Fig. 8-I. Vertical displacement – sinesweep

b) Road recordings

An important issue when testing non-linear systems is the excitation signal. As system properties vary with the type and energy level of the input signal, appropriate testing signals need to be defined. When considering car suspension systems and tire patch excitation, as is the case in the KULeuven set-up, these signals should accurately represent actual driving conditions. For this purpose, the test vehicle is instrumented with accelerometers at the wheel knuckle and shock absorber strut and/or with a 6-DOF wheel-to-car-body relative displacement measurement system, called “Wheeltracker” (Fig. 9-I right.). Road recordings for vehicle suspension should always be measured in the most ideal conditions. When considering the signal to noise ratio (S/N) for accelerometer and displacement measurements it can be seen that at lower frequencies (0-50Hz), displacements between a few cm and tenths of mm are recorded. A signal with amplitude of 1 cm at 1 Hz yields an acceleration of 0.04 g. For a classic accelerometer with sensitivity 100 mV/g this leads to about 4 mV or 0.08 percent of the sensor dynamic range (50g). Because of the relatively high accelerations in the suspension system (10-20g) a higher sensitivity accelerometer cannot be used. When measuring the accelerations at stand-still with idling engine, a noise level standard deviation of 3.5 mV is recorded. The low frequency signal level is equal to this noise level. Some filtering can still be applied, but this example clearly indicates that accelerometer measurements are not easily usable in the very low frequencies, important for vehicle handling. In this research accelerometers are only used for road recordings above a corner frequency of 5 Hz. Next to this resolution problem, the acceleration signal needs a double integration to generate displacement targets and these signals need to be compensated for drift. For the wheel displacement

measurements, 1 cm represents 3.3 percent of the sensor range (range for X, Y, Z = 300mm) and is sampled at 200 Hz with a resolution of 2 microns. The dynamics of the wheel displacement measurements are limited by the sampling frequency of 200 Hz. These recordings can therefore only be used in the "ride & handling" frequency range from 0 to 50 Hz. An experiment on a smooth road was performed to investigate the limits of the displacement measurements. The noise level, at stand-still with idling engine, has a standard deviation σ of 0.06 mm. On Fig. 9-I the two times sigma line (green) represents the noise floor. Reliable measurements are therefore possible up to about 40 Hz. For closed loop control road reproduction purposes a S/N ratio of 20 dB is preferred; this is indicated by the red line. Performance is therefore limited to 17 Hz. The (smooth) road spectrum, typically dropping off at 9 dB/octave in the ride & handling frequency range, can easily be identified. Because measurements were performed on a smooth road, even better results are expected for medium and rough road recordings. A road recording (vertical road acceleration spectra) of a 'Belgian blocks'-road is given in Fig. 10-I for a car driven at 20km/h in 1st gear, 2nd gear, neutral and engine off. It can be seen that the wheel hop (± 15 Hz) peak for both driven curves (1st & 2nd gear) is almost equal and has lower amplitude than the non-driven curves (neutral & engine off). The driving conditions clearly influence the damping of this motion, yet leave the resonance frequency unchanged. The driven curves (1st & 2nd gear) differ very little from each other over the whole frequency range, showing that the sensor location close to or on the wheel has little disturbance from the engine and transmission. In the range 100-120 Hz a lower peak is visible on all curves. A small downward frequency shift is observed between driven and non-driven curves. This frequency shift can be attributed to the presence of transmission torque, changing the response of the tire-wheel system.

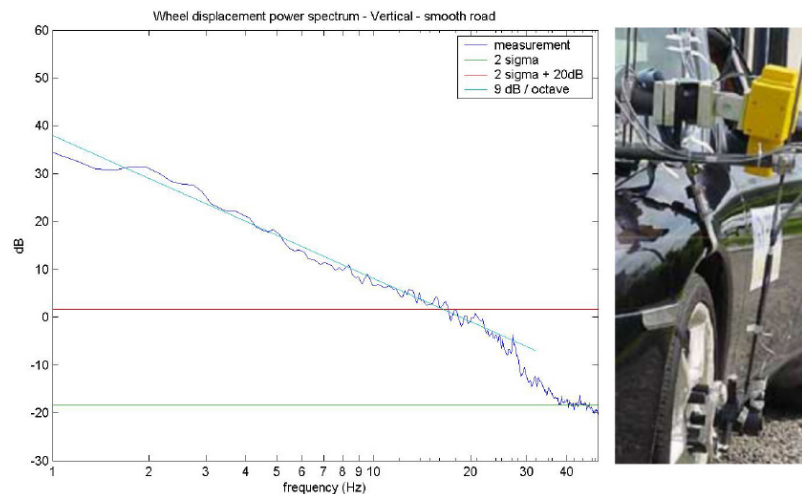


Fig. 9-I. Wheel displacement spectrum / 6-DOF Wheeltracker measurement system

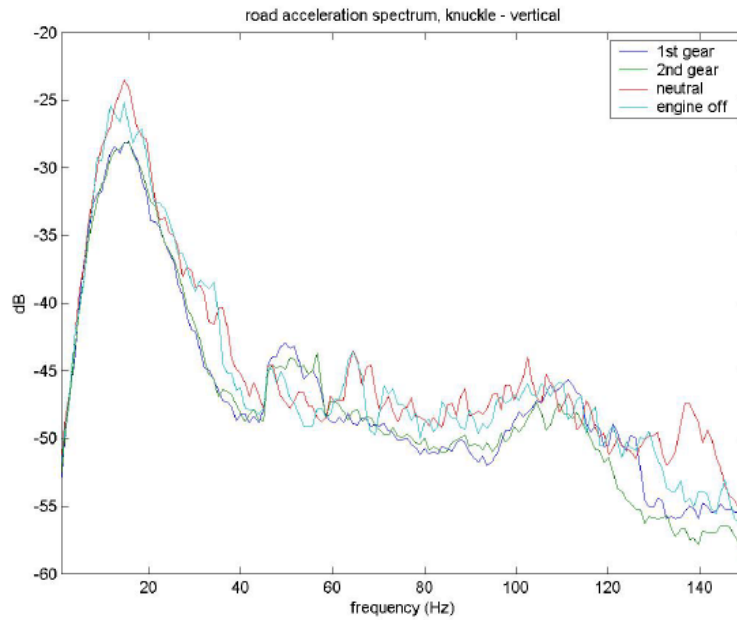


Fig. 10-I. Road acceleration spectrum - Knuckle vertical motion

c) Non-linear effects

As mentioned above, non-linear effects need to be accounted for when performing MDOF vehicle suspension testing. To illustrate this, a FRF between shaker table displacement and knuckle acceleration was recorded for the transversal excitation at the front tire (Fig. 11-I).

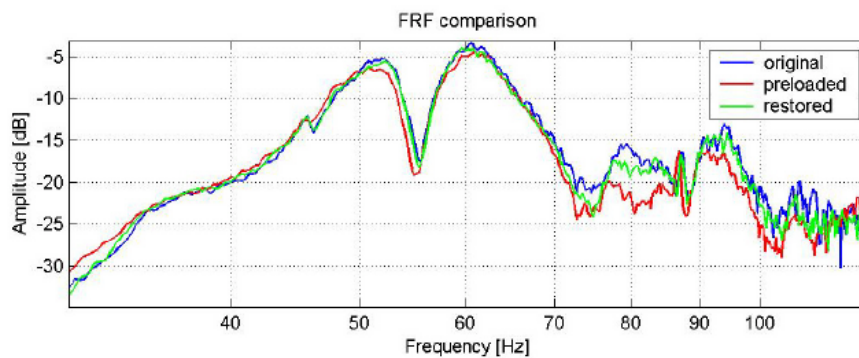


Fig. 11-I. FRF-comparison, transversal excitation, transversal preload

The first curve (blue) represents the original situation, the second (red) when applying a preload in the transversal direction and the third one (green) when the preload was removed again. The preload was applied by adding a geometric offset, which is not so

accurate; force measurements would certainly increase both accuracy and repeatability. Next to preloads, which represent dynamic manoeuvres like braking, accelerating and cornering, amplitude effects are important. Using the "Belgian blocks"-road recordings mentioned before, a 3-DOF road reproduction experiment was conducted.

d) Structure borne road noise

Results are evaluated based on their spectral and time series error. Fig. 12-I shows spectra for target and measurement for vertical (top), longitudinal (middle) and transversal (bottom) DOF. The spectral plots show three curves: target recording (blue), reproduction result after the System Identification (SI) procedure (green) and reproduction result after the Target Simulation procedure (red). The complete experiment took 12 model updates (SI) and 5 iterations (TS) to achieve the presented results. The test duration is dependent on the tuning data length. For a SI target of 1 minute and a TS target of 2 minutes, the experiment took about 3 hours. For longer target lengths the time increase is less than proportional. The spectral error (measurement-target) is plotted in Fig. 13-I for all three DOFs. The results can be split in four sections over the frequency band: 5-55 Hz, 55-85 Hz, 85-120 Hz and 120-150 Hz. The first section shows very good reproduction results with the spectral error varying ± 0.6 dB. The second section shows more difficult reproduction with spectral errors between -3.2 and +5.1 dB. A closer look at the plot learns that the vertical DOF has an almost constant underexcitation of -2 dB. While the transversal DOF is overexcited (+1.6 dB) and the longitudinal DOF underexcited (-2.5 dB) at 64 Hz, the opposite (Transversal=-2.7 dB, Longitudinal=+5.1 dB) is true at 72 Hz. The performance improves between 85 and 120 Hz (-0.8 dB,+0.4 dB) and more reproduction error (+0.2 to +1.3 dB) in longitudinal and transversal axis is introduced from 120 Hz onwards. When comparing the results with Random Vibration Control (RVC) tests according to for example EN61373 or ASTM D4728, which have been successfully implemented on this shaker table, the longitudinal DOF exceeding the +3 dB error limit in the 69-78 Hz range would be found respectively unacceptable (EN) and perfectly acceptable (ASTM). Both norms specify SDOF table measured excitation, far less complicated than this MDOF vehicle response reproduction experiment. A SDOF and 2-DOF experiment preceded this work, with SDOF reproduction having no significant (\pm more than 1 dB) spectral error over the range 5-150 Hz. It was only for the 2-DOF experiments that these errors emerged. This phenomenon was used to illustrate that not any MDOF signal can be used for characterization of non-linear MDOF systems and that real road recordings are important for obtaining good reproduction results. In the SDOF-experiment measured and synthetic target signals were reproduced in a vertical SDOF configuration, with no difference in reproduction accuracy, whereas the 2-DOF case showed significant influence of the target nature (measured vs. synthetic targets). This does not mean that correct signal levels are only important in MDOF testing. They are equally, maybe even more, important in SDOF in order to have correct model identification, but this cannot be evaluated based upon reproduction accuracy. Models identified with non-recorded signal levels or spectra therefore not always correctly represent the identified system. Experiments aimed at (MDOF) system identification and FRF

measurement are required to achieve a higher level of accuracy than RVC testing or durability oriented road simulation experiments. From the time data series different error indicators can be calculated. These are summarized in Table 1-I. The first indicator compares rms values of target and measurement. RVC norms allow between 10 & 30 % deviation. The rms value of the tracking error versus target rms and peak value are given next, the proportion of both indicators being the crest factor (Peak/rms). Normal RVC tests keep the crest factor below 3 in order to achieve sufficient energy density with limited stroke or dynamic force and, in accelerated life testing (durability), to avoid specimen damage due to occasional high amplitude excitations. The crest factor of a road recording is generally well above 3 and care must be taken when signals are modified to reduce the crest factor. In this experiment the shaker table's performance and stroke permitted the use of unmodified signals. The second part of Table 1-I shows mean, peak and rms of the spectral error. When comparing the table values with the plot from Fig. 13-I, only the peak indicator reveals the existence of the 55-85 Hz problem band.

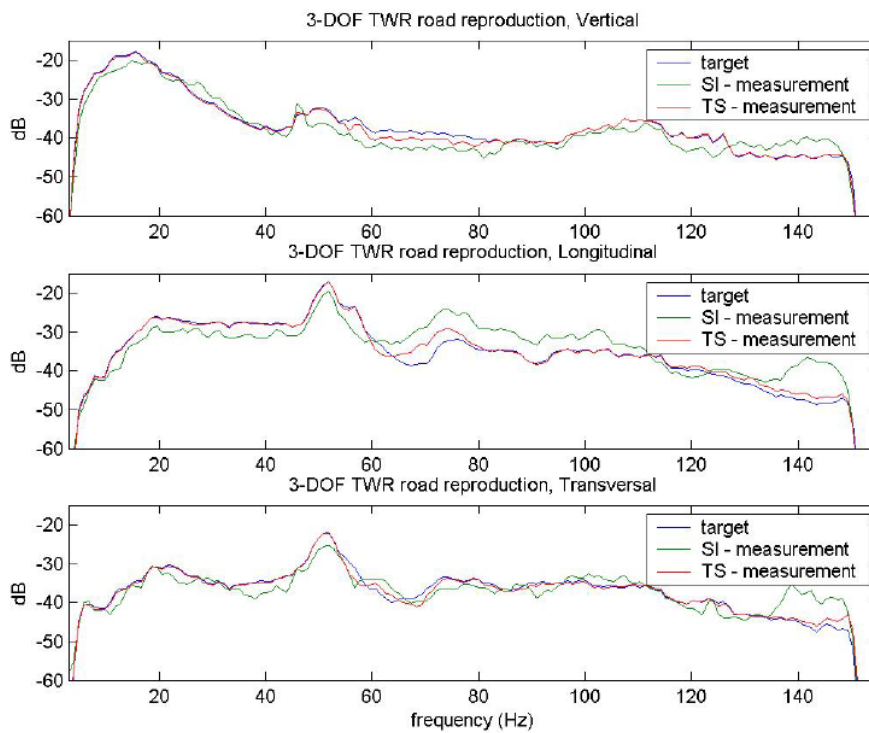


Fig. 12-I. Road reproduction results

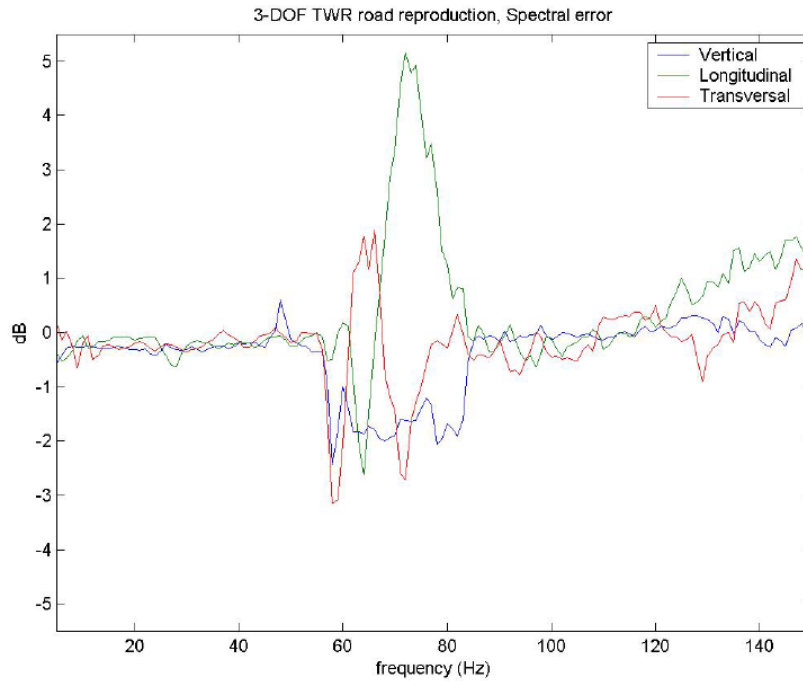


Fig. 13-I. Road reproduction results – spectral error

Table 1-I. Reproduction error indicator

Indicator	Vertical DOF	Longitudinal DOF	Transversal DOF
rms(meas)-rms(target)	-3.4%	-2.5%	-0.3%
rms(error)/rms(target)	8.7%	22.3%	24.8%
rms(error)/peak(target)	1.3%	4.0%	4.9%
Crest factor	6.8	5.6	5.0
mean(spectral error)	0.4 dB	0.2 dB	-0.4 dB
peak(spectral error)	2.4 dB	3.1 dB	5.2 dB
rms(spectral error)	0.7 dB	0.7 dB	1.2 dB

3I.3 Conclusions

Multi-axial dynamic testing is becoming a standard practice in the dynamic testing field. The CUBE 6 DOF hydraulic shaker installed at KU Leuven is able to perform different typologies of tests, including single DOF shock and vibration testing, multi DOF random vibration control and road reproduction, full vehicle testing under quasi-operational loading condition, highly dynamic multi-axial testing of vehicle

components, accelerated life-time prediction and durability testing of different components, structure-borne road noise investigation, system identification of nonlinear components. Two examples of these testing activities are reported, showing the importance and the capabilities of this equipment.

Acknowledgments

The Research Fund KU Leuven is gratefully acknowledged for its support.

3I.4 References

- [1] Berckmans, D., Pluymers, B., Sas, P., Desmet, W. (2011). Testing research activities at the Noise & Vibration Research Group of the K.U.Leuven. *European Journal of Mechanical Engineering*, 2011 (1), 15-21
- [2] De Coninck, F., Vaes, D., Swevers, J., Desmet, W., Sas, P. (2004). Vehicle suspension and structure borne road noise testing on a 6-DOF high frequency shaker table: first outlines. *Proceedings of the 30th Fisita 2004 World Automotive Congress*. 30th Fisita 2004 World Automotive Congress. Barcelona, Spain, May 23-27, 2004

Annex 3J

Experimental approaches for monitoring of rotational dynamics systems

Simona Moschini¹, Konstantinos Gryllias¹, Bert Pluymers¹ and Wim Desmet¹

¹Department of Mechanical Engineering, KU Leuven,
Celestijnenlaan 300B, 3001 Heverlee (Leuven), Belgium,
Simona.Moschini@kuleuven.be,

Konstantinos.Gryllias@kuleuven.be, Bert.Pluymers@kuleuven.be,
Wim.Desmet@kuleuven.be,

Abstract. During last decades the scientific community focused its attention on strategies to reduce the global Green House Gases (GHGs) emissions. Materials have been developed or improved to avoid energy dispersion; new techniques have been developed in order to exploit at best renewable and non-renewable energy sources. Other paths are currently followed to pursue the same goal, for instance, the introduction of hybrid and electric vehicles (EVs) into the automotive market. EVs are characterized by a completely new dynamic behaviour with peculiar NVH characteristics and their innovative drivelines include novel components. This last aspect calls for ingenious monitoring system and techniques. In this framework, the concept of virtual sensing reveals itself as one of the most powerful tools. Several physical quantities are relevant to define the health status of the system. Unfortunately, many of these quantities cannot be directly measured in many practical applications due to lack of specific sensor or to the environment in which the system is operating. As a consequence, state estimation techniques come out as an extremely helpful tool. These techniques allow combining the world of measurements with the one of numerical modelling leading to the estimation of the desired unmeasurable system quantities. In the current research a Kalman Filter based algorithm is applied to investigate and assess the health condition of a simple driveline. The attention is focused on the estimation of one of the most common malfunction for rotating components: the unbalance.

3J.1 Introduction

EVs have recently hit the automotive market as powerful solution to decrease the GHGs emission. EVs use one or more electric motors for propulsion. Electric motors are an appealing alternative to combustion engines in vehicles: they can be powered from renewable energy sources and do not cause emissions where they are being used. The most common primary energy storage system used in EVs is batteries. In recent years tremendous improvements have been made in terms of the energy density of batteries to allow EVs to compete with engine powered vehicles. Research has shown that one way of increasing the lifetime and energy density of EV primary energy storages is to integrate power buffers in the drivelines, in the form of flywheels [1]. A proper functioning of this rotating component plays a key role for the

efficiency and effectiveness of the driveline it belongs to. A flywheel is a rotating mass that stores energy in the form of kinetic energy and it can be assimilated to a rotor based driveline. Among the different kinds of malfunction that can affect rotor-based drivelines, unbalance is one of the most important. If the rotor mass centerline and the rotor rotational axis don't coincide, unbalanced inertia related forces occur. They rotate together with the rotor and are oriented perpendicular to the rotational axis. The major effects are increased levels of vibration and radial loads acting on the structure unforeseen in the design phase. The rotor unbalance acts as external synchronous centrifugal force acting in the lateral vibration mode. Lateral vibration is the most critical because it is generally the principle cause for structural failures in rotor systems inducing, among others effects, rubbing of the rotor against the stator [2]. Unfortunately, unbalance cannot be directly measured. Current diagnostics techniques are mainly based on the analysis of the induced vibrations with respect to a limit value. The main advantage of the classical so called limit value supervision methods is their simplicity and reliability. However, they are only capable of detecting the malfunction after a relatively large change of the monitored feature or a long lasting gradually increasing malfunction [3]. A different approach to the monitoring problem arises from the modelling world: the virtual sensing approach. Virtual sensing techniques deserved special attention during the last years, especially for automation industry [4]. The basic concept behind the several strategies that have been developed along the years is to add knowledge to the available measurements through a dedicated modelling technique, allowing extracting more information from the experimental data. When analysing a generic system, several quantities are of interest to describe the behaviour of the system itself as response to external forces. In many practical situations, the most important quantities cannot be directly measured due to lack of space or specific sensors. The ad hoc application of state observers instead allows determining the quantities that are fundamental to assess the health status of the system but that are not directly measurable

3J.2 Virtual Sensing Algorithm

The adopted virtual sensing algorithm is based on the Kalman Filter (KF) theory [5]. The KF is an iterative solution to the problem of filtering experimental data through a linear filter: it is very effective in evaluating the state of a dynamic system affected by noise with a Gaussian distribution and zero mean value. KF can be used as well as state observer to predict unmeasured or unmeasurable system quantities. The estimation performed by the KF consists of a prediction and a correction step. The former is based on the numerical model of the system, usually described in terms of state variables, the latter on a suitable weighting of the difference between the predicted and collected measurement data. They recursive two step prediction approach is relatively not cumbersome in terms of computational cost [6]. In the discrete time domain, at time step k , the system dynamics can be expressed as:

$$\begin{aligned} \underline{z}_k &= [F]_{k-1} \underline{z}_{k-1} + [G]_{k-1} \underline{u}_{k-1} + \underline{w}_{k-1} \\ \underline{y}_k &= [H]_k \underline{z}_{k-1} + \underline{v}_{k-1} \end{aligned} \quad \text{Eq. 1-J}$$

where:

- \underline{z} is the state variables vector
- $[F]$ is the discrete time state matrix
- $[G]$ is the discrete time input matrix
- \underline{u} is the input force vector
- \underline{w} is the process noise
- \underline{y} is the measurement vector
- $[H]$ is the observation matrix
- \underline{v} is the measurement noise

The process and measurement noise, \underline{w} and \underline{v} are white, zero-mean, uncorrelated noises with known covariance matrices $[Q]_k$ and $[R]_k$ respectively.

The first step of the KF algorithm, the *prediction* or the *a priori* state estimation step, is based on the system model:

$$\hat{\underline{z}}_k^- = [F]_{k-1} \hat{\underline{z}}_{k-1}^+ + [G]_{k-1} \underline{u}_{k-1} \quad \text{Eq. 2-J}$$

The second step, the *correction* or *a posteriori* state estimate step, starts from the *a priori* estimate (Eq. 2-J) and corrects it according to the difference between the predicted and the available measurements:

$$\hat{\underline{z}}_k^+ = \hat{\underline{z}}_k^- + [K]_k (\underline{y}_{k-1} - [H]_k \hat{\underline{z}}_k^-) \quad \text{Eq. 3-J}$$

The matrix $[K]_k$ in Eq. 3-J is the Kalman gain matrix that is a function of the noises covariances, the system matrices and the covariance of the state estimation error.

Starting from the basic KF formulation (Eq. 2-J, 3-J) different extensions of the KF have been developed throughout the years [5].

A particular extension of the KF, the Augmented Kalman Filter (AKF), will be applied in the case under investigation to estimate the unbalance. AKF allows estimating the unknown forces acting on the system, including them in the state vector. The prediction - correction steps involved in the AKF are exactly the same as presented in Eq. 2-J and Eq. 3-J for the original KF formulation. The difference arises in the expression of the state vector and state matrix.

The first equation in Eq. 1-J becomes:

$$\underline{z}_{a_k} = \begin{bmatrix} [F]_{k-1} & [G]_{k-1} \\ 0 & 0 \end{bmatrix} \underline{z}_{a_{k-1}} + \begin{Bmatrix} \underline{w}_{k-1} \\ \underline{w}_{u,k-1} \end{Bmatrix} \quad \underline{z}_{a_k} = \begin{Bmatrix} \underline{z}_k \\ \underline{u}_k \end{Bmatrix} \quad \text{Eq. 4-J}$$

In Eq. 4-J $\underline{w}_{u,k-1}$ is the noise associated with the unknown input. $\underline{w}_{u,k-1}$ satisfies the same hypothesis as \underline{w} and \underline{v} . In absence of a better modelling available, the updating

equation for the unknown input can be expressed according to the random walk model as follows:

$$\underline{u}_k = 0 + \underline{w}_{u,k-1} \quad \text{Eq. 5-J}$$

Numerical simulations have proven the efficacy of the proposed methodology [7]. The experimental validation of the described methodology to unbalance identification will be presented in the following section [8].

3J.3 Algorithm validation

A modification of an existing test rig has been designed to validate the proposed approach. The basic test rig consists of two electrical motors connected through a double cardan joint [6]. The motors are squirrel cage motors and the test rig is equipped with a torque sensor, the left motor delivers power to the system while the right one acts as a simple inertial load (Fig. 1-J). The test rig allows reaching rotational frequencies up to 50 Hz.

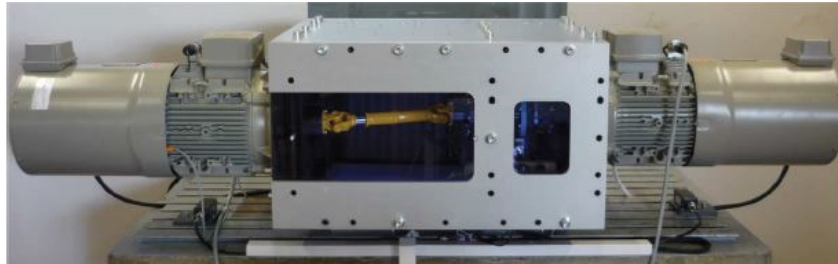


Fig. 1-J. Test Setup

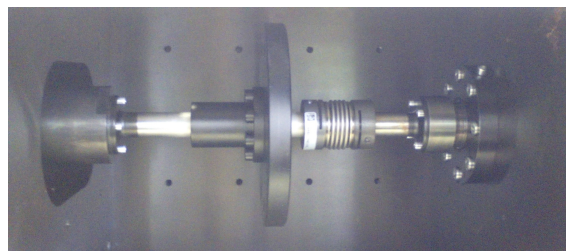


Fig. 2-J. Driveline under investigation

The ad hoc designed driveline consists of a shaft and a disc (Fig. 2-J). The shaft, due to design restriction, is divided in two parts that are connected through a torsionally rigid elastic coupling. On the left side the shaft is directly connected to the motor while on the right side, it is supported by a radial roller bearing. This simple setup

allows generating unbalance response of the rotor. The disc is designed in such a way that it is possible to apply controlled unbalance through a series of radial holes.

A lumped parameter model has been used to represent the behaviour of the driveline of Fig. 2-J. The mass is concentrated in the rotor and the shafts are modelled as slender beams (Fig. 3-J).

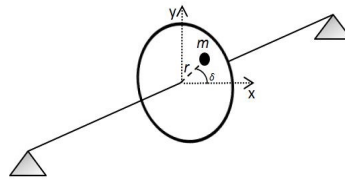


Fig. 3-J. Isotropic rotor model

The motion of the rotor consists of two lateral transversal modes: vertical and horizontal. The supports are modelled as linear springs in the two directions. The two motions are not coupled and the result is a rotor lateral circular orbital motion. In an unbalanced condition the rotor mass centerline does not coincide with the axis of rotation, as a result radial forces will arise as consequence of an uneven mass distribution. From the modelling point of view, this effect can be modelled as one lumped force function of the unbalance mass m , unbalance radius r , unbalance angle δ and the square of the constant rotational speed Ω (Eq. 6-J). This force is attached to the rotor and rotates with it at rotational speed Ω [2].

$$F = mr\Omega^2 e^{j(\Omega t + \delta)} \quad \text{Eq. 6-J}$$

Different assumptions have been made in the rotor modelling process, the most important being [2]:

- the rotor is rotating at constant rotational speed Ω
- the gyroscopic effect is neglected
- the model is linear: all the forces are linear either in time or in displacement, velocity or acceleration
- supports are considered elastic in both x and y direction

The governing equations of the model of Fig. 3-J can be obtained starting from the expressions of potential, dissipative and kinetic energy through the Lagrangian approach:

$$\begin{aligned} M\ddot{x} + D\dot{x} + Kx &= mr\Omega^2 \cos(\Omega t + \delta) \\ M\ddot{y} + D\dot{y} + Ky &= mr\Omega^2 \sin(\Omega t + \delta) \end{aligned} \quad \text{Eq. 7-J}$$

The symbols M , D , and K in Eq. 7-J are respectively the rotor mass, the damping associated with the shafts and the stiffness resulting from the series of flexible supports and shafts. The damping is included as linear combination of the mass and stiffness matrices of the global system. The unbalance force is projected along the horizontal direction and the vertical direction. Vertical and horizontal directions are defined according to a right hand reference system having as z axis the axis of the shaft of Fig. 3-J. The dot accent represents the derivative with respect to time.

As a first step towards the validation of the proposed methodology, the displacements of the shaft centerline have been chosen as the input variables for the virtual sensing algorithm, described in the first section. Given the structure of the original test rig, the shaft displacements have been measured using inductive probes at the left hand side of the disc. The acquisition time has been set to 30s, the sampling frequency has been selected to avoid aliasing problems and to guarantee a bandwidth up to 1300 Hz.

The system has been excited imposing a known unbalance by means of a weight applied to the disc (Fig. 4-J).

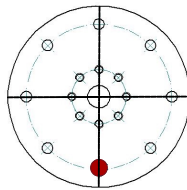


Fig. 4-J. Unbalance position

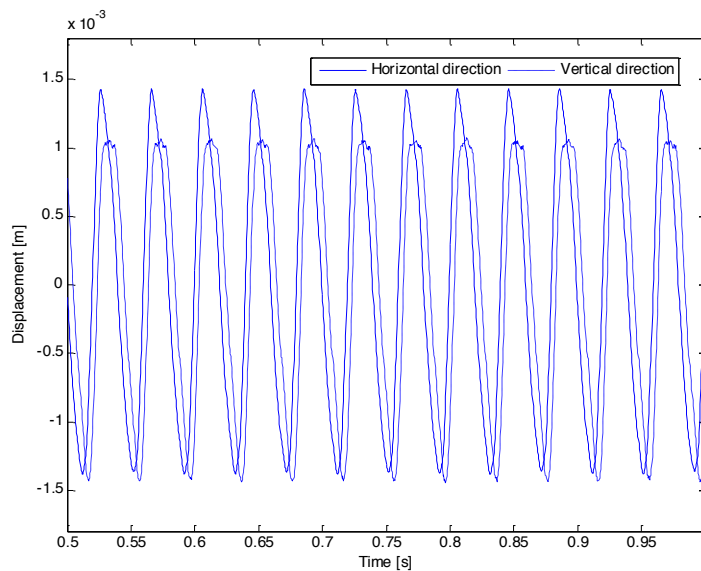


Fig. 5-J. Shaft displacements

An example of the measured displacements is shown in Fig. 5-J. The unbalance induced vibration trend is clearly visible. Literature studies showed indeed how the unbalance induced vibrations are characterized by a predominant sinusoidal behaviour with frequency equal to the rotational frequency of the shaft itself, in this case imposed to 25 Hz (Muszynska, 2005).

An accurate tuning of the parameters of Eq. 7-J, i.e. system mass, damping and stiffness, is an important step in order to match the characteristics of the system. One of the standard ways to identify rotor based drivelines is the perturbation test. Due to design restrictions, the selected strategy to be able to quantify the system properties has been a perturbation test with synchronous excitation. For a given unbalance mass and location several run out of the system have been performed considering different frequency of rotation and the dynamic stiffness has been computed for each analysed frequency. The analysis of the trend of the direct and quadratic dynamic stiffness is a well-known procedure to retrieve the parameters of the system [2]. Within the range 0 Hz - 50 Hz, the behaviour of the system under investigation is characterized by a flat direct dynamic stiffness curve. Therefore the global system stiffness, comprehensive of shaft and support stiffness, has been as first approximation estimated as an educated guess starting from the static stiffness.

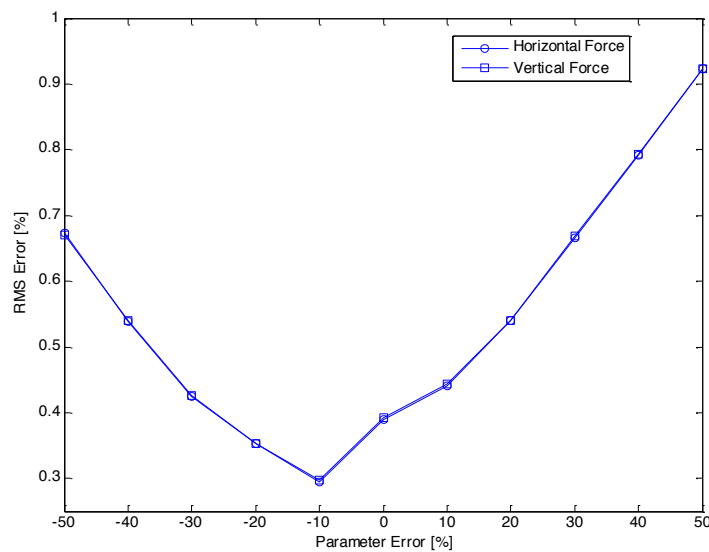


Fig. 6-J. Estimation error trend towards parameter error

A numerical sensitivity analysis has been carried out in order to quantify the sensitivity of the virtual sensing algorithm to the uncertainties introduced by the system parameter identification procedure. High uncertainties affecting the outcome of the base numerical model can nullify the advantages of even a highly refined model of the structure from a virtual sensing point of view. To be able to quantify the influence of these uncertainties on the efficiency of the method, a preliminary

numerical analysis has been carried out to evaluate the influence of an error in parameter assessment on the quality of the estimation. The results, for a given SNR of 30 dB, are shown in Fig. 6-J.

The Root Mean Square (RMS) of the error computed according to Eq. 8-J, the absolute value of the difference between the imposed unbalance force F and the estimated one F_e has been chosen as indicator of the estimation quality.

$$Error = |(F - F_e)| \quad \text{Eq. 8-J}$$

For an error on the parameters of $\pm 50\%$, the variation of the estimation error is within 1%. The absolute variation of the error is negligible, the relative variation of the error with respect to the reference case of perfectly known system parameters is considered within the tolerance margin for an accurate estimation of the unknown excitation force. Hence, the approximations introduced by the system stiffness identification procedure are considered acceptable from the unbalance force estimation point of view.

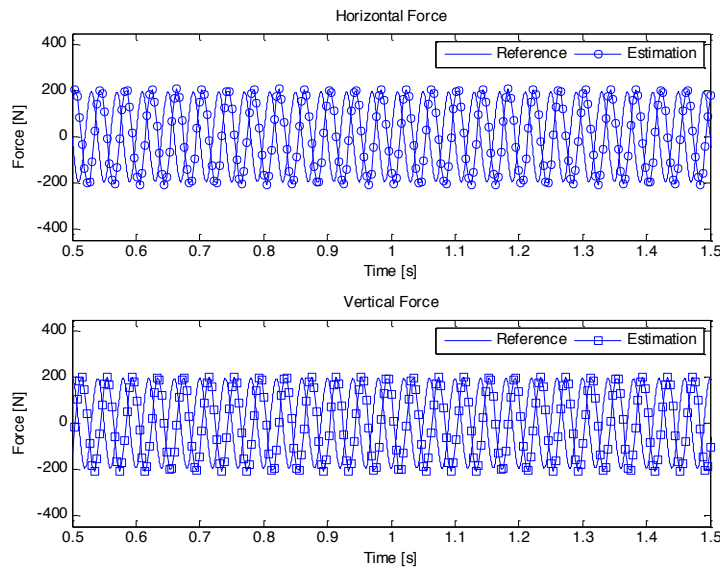


Fig. 7-J. Estimated unbalance forces in the horizontal and vertical direction using the virtual sensing algorithm

Fig. 7-J shows the results of the application of the proposed virtual sensing technique to the test rig of Fig. 2-J. The displacements of Fig. 5-J have been used as input signals. The reference force in the two directions is computed, according to Eq. 6-J as product of the known unbalance mass m the unbalance radius r and the square of the rotational speed Ω , with a nominal phase of 270 degrees. The obtained results show the suitability of the proposed methodology which is capable of estimating the

unknown input acting on the system with a RMS Error lower than 8%. The time lag between the estimated forces and the reference ones can be considered negligible in view of the research goal. An early detection of unknown forces acting on the structure is important to avoid undesired consequences for the structure itself like the increase of vibration and consequent rubbing of the rotor against the stator or rotor bowing. None of the abovementioned phenomena has a sudden nature thus a delay in the estimation of 0.0156 s is considered acceptable.

3J.4 Conclusions

Research has shown that embedded power buffers in EV drivelines can enhance the efficiency of the EV itself. A possible solution is integrating flywheels in EV drivelines. The current research deals with the application of virtual sensing techniques to driveline monitoring. An Augmented Kalman Filter state estimation algorithm is combined with online displacement measurements and a classical rotordynamic model, in order to quantify the unbalanced forces. The efficiency of the method is evaluated using simulations and a specially designed experimental test rig. The time delay of the estimation is considered as acceptable and can be further reduced. To conclude, the developed virtual sensing procedure can serve as a part of condition monitoring systems, contributing to the accurate and on time fault detection in EV drivelines.

3J.5 References

- [1] J. Santiago, J. Oliveira, J. Lundin, J. Abrahamsson, A. Larsson and H. Bernhoff, "Design Parameters Calculation of a Novel Driveline for Electric Vehicles," *World Electric Vehicle Journal* (2009) 225-232.
- [2] A. Muszynska, *Rotordynamics*, CRC Press, Taylor & Francis, 2005.
- [3] R. Isermann, "Model-Based fault-detection and diagnosis - status and applications," *Annual Reviews in Control* (2005) 71-85.
- [4] R. Isermann, "Fault diagnosis of machines via parameter estimation and knowledge processing - tutorial paper," *Automatica* (1993) 815-835.
- [5] D. Simon, *Optimal state estimation*, Wiley (2006).
- [6] B. Forrier, F. Naets and W. Desmet, "Virtual sensing on mechatronic drivetrains using multiphysical models, in ECCOMAS 2015.
- [7] S. Moschini, K. Gryllias, B. Pluymers and W. Desmet, "State estimation techniques for rotor unbalance identification," in COBEM, Rio de Janeiro, 2015.
- [8] S. Moschini, K. Gryllias, W. Desmet and B. Pluymers, "Virtual sensing for rotordynamics," in TurboExpo (Under Submission), Seoul, 2016.